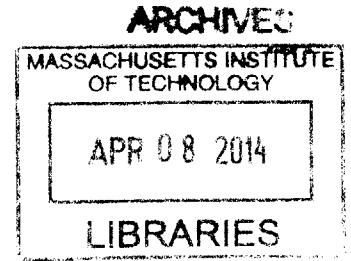# An in-situ accelerator-based diagnostic for plasma-material interactions science in magnetic fusion devices

by

Zachary Seth Hartwig

B.A. in Physics, Boston University (2005)

Submitted to the Department of Nuclear Science and Engineering
in partial fulfillment of the requirements for the degree of

Doctor of Philosophy

at the

MASSACHUSETTS INSTITUTE OF TECHNOLOGY

February 2014

Author . . . .
Department of Nuclear Science and Engineering
21 November 2013

Certified by . . . .
Dennis G. Whyte
Professor
Thesis Supervisor

Certified by . . . .
Richard C. Lanza
Senior Research Scientist
Thesis Reader

Accepted by . . . .
Mujid S. Kazimi
TEPCO Professor of Nuclear Engineering
Chair, Department Committee on Graduate Students

An in-situ accelerator-based diagnostic for plasma-material interactions science in magnetic fusion devices

by

Zachary Seth Hartwig

Submitted to the Department of Nuclear Science and Engineering
on 21 November 2013, in partial fulfillment of the
requirements for the degree of
Doctor of Philosophy

Abstract

Plasma-material interactions (PMI) in magnetic fusion devices such as fuel retention, material erosion and redeposition, and material mixing present significant scientific and engineering challenges, particularly for the next generation of devices that will move towards reactor-relevant conditions. Achieving an integrated understanding of PMI, however, is severely hindered by a dearth of *in-situ* diagnosis of the plasma-facing component (PFC) surfaces. To address this critical need, this thesis presents an accelerator-based diagnostic that nondestructively measures the evolution of PFC surfaces *in-situ*. The diagnostic aims to remotely generate isotopic concentration maps that cover a large fraction of the PFC surfaces on a plasma shot-to-shot timescale.

The diagnostic uses a compact, high-current radio-frequency quadrupole accelerator to inject 0.9 MeV deuterons into the Alcator C-Mod tokamak. The tokamak magnetic fields in between plasma shots are used to steer the deuterons to PFCs where the deuterons cause high-Q nuclear reactions with low-Z isotopes $\sim$5 μm into the material. Scintillation detectors measure the induced neutrons and gammas; energy spectra analysis provides quantitative reconstruction of surface concentrations. An overview of the diagnostic technique, known as accelerator-based in-situ materials surveillance (AIMS), and the first AIMS diagnostic on the Alcator C-Mod is given; a description of the complementary simulation tools is also provided. Experimental validation is shown to demonstrate the optimized beam injection into the tokamak, the quantification of PFC surfaces isotopes, and the measurement localization provided by magnetic beam steering. Finally, the first AIMS measurements of fusion fuel retention are presented, demonstrating the local erosion and codeposition of deuterium-saturated boron surface films. The finding confirms that deuterium codeposition with boron is insufficient to account for the net fuel retention in Alcator C-Mod.

Thesis Supervisor: Dennis G. Whyte
Title: Professor

Thesis Reader: Richard C. Lanza
Title: Senior Research Scientist

3

Fear is the mindkiller.

—— Paul Maud'Dib

Acknowledgments

In many ways, this section was the most difficult for me to write. When one has received so much from so many it becomes a challenge to convey to each of them the depth of gratitude that they are owed; I have made my best effort here. As such, I discarded the possibility of a standard single acknowledgments page long ago and make no apology for my lack of brevity.

I have decided to split my acknowledgments into personal and professional categories since I owe the achievement of this thesis not only to my scientific colleagues but also to my family and friends outside of MIT. These categories are somewhat arbitrary, however, as I am extremely fortunate to count many of those who have contributed to my scientific development as personal friends.

Professional

Because I consider this thesis to be the culminating destination in the long adventure of training to be a scientist, I find it most appropriate to start at the very beginning of the journey. I am grateful to Paul Baudendistel, whose passion for science and excellence in teaching first kindled my interest in physics in his high school classroom; I recall clearly to this day his brave demonstration of conservation of energy with a bowling ball and a pendulum! I am next indebted to Martin Schmaltz, who taught me electromagnetism as an undergraduate biomedical engineer. Conversations with him outside of the classroom opened my mind to the beauty and challenge of physics; I switched majors and haven't looked back.

My first opportunity to do physics in the laboratory I owe to Lee Roberts, who offered me a research position at Boston University. During my time there, I had the privilege of working with two of the most generous and gifted physicists. I owe the majority of my development as an experimental physicist to Kevin Lynch, whose patient teaching, hilarious cynicism, high expectations, and tolerance for practical jokes helped me flourish as a younger student. Rob Carey complemented that education in the laboratory, classroom, and adviser's office; in my own interactions with students and colleagues I continuously strive to emulate his example.

During my thesis work at MIT, I had the privilege of working with an extraordinary

7

Personal

As I thought about these acknowledgments to preface my thesis on advanced measurement instrumentation, it is amusing but entirely expected to discover that the debt I owe to my immediate family is beyond measure. My parents, Paul and Kitty, probably deserve the accolades that accompany this thesis more than I do. It was their parenting skill, constant support, and enduring patience (sometimes severely tested!) that molded me into the person I am today. I also owe much to my brothers, Matt and Fitz. While I am now a physicist, Matt was the reason I ended up in science and engineering, due to his pursuit of engineering and willingness to share his Legos. Fitz's tremendous accomplishments continue to impress and inspire me, and parts of this thesis were written to his outstanding recent EP.

I am very much indebted to Emily Jump. She not only agreed to marry me during an extremely stressful and busy time in our lives but provided unending, uncomplaining support that made all the difference during the last few years of fairly nonstop work. She has brought a tremendous amount of levity and joy into my life that has provided a much needed sense of balance and perspective.

My relationship with Martha Fischhoff has simply been transformative. She is on of the most inspiring people I have ever met and I am deeply grateful that she remains a constant in my life. Bryan and Elliot Pennington have been my close friends and partners-in-crime for over half of my life, and Elliot Rauscher for a few years before that. I am very grateful to these three for the many shared antics, adventures, and achievements that have passed and those yet to come.

I am indebted to my close friends Ugo Amadi and Sangeeta Ballal, who have provided an incredible source of friendship since our undergraduate days. Ugo has challenged me to grow in many ways and, sometime against my will, to expand my horizons; I thank him greatly for the improved view. I am grateful to Sangeeta for her support, friendship, and tolerance of my ridiculous metaphors; her continuing friendship has made the distance between us seem not so large.

From the 225 mile Boston-to-New York ride to our participation in the "Olympics" in Montreal, Shane Mulrooney and I have shared a number of adventures; I tremendously appreciate his steadfast presence and friendship over year. Bridgid Mulrooney has also been an a close friend, providing me with a lot of laughs and showing much tolerance to her husband and I's antics. I owe an incalculable amount to Andrew Inglis, who has played so many different roles: long-time housemate, physics colleague, startup co-worker, cycling teammate, fellow adventurer, close friend, and Shaklee Physique aficionado. His unquenchable passion for life, adventure, and innovation has inspired my own great efforts.

In addition to the cycling, conversation, and good food over the years, I'd also like to thank Gabe Redner for his forgiving nature: our first significant encounter was when I accidentally bumped his optical table and destroyed three hours of precision

calibrations in the undergraduate physics laboratory. Incredibly, we became friends and remain so to this day. Ken Lane - cyclist, physicist, inimitable character - helped me tremendously with graduate school applications, has invited me to his table with his friends and family, and is the possibly the finest cook of tartiflette on this side of the Atlantic.

I owe my sanity, in part, to Mark Vautour and Sean Owen. The time I have spent on the bike with them over the years - whether night riding the battle road ("The British are coming!"), completing an offroad ride with the help of a "borrowed" boat, or riding the unthinkable 317 miles to Montreal in 22 hours straight - has been an unforgettable experience. I hope that the completion of this thesis heralds the return of more hours in the saddle together.

Yuri Podpaly and I have the kind of friendship that can only be forged through surviving our first years of graduate school together in the same office. We have shared many laughs, frustrations, and heated debates over the years, and he is largely the reason I passed my quals. His absence after his graduation has made me appreciate our time together even more.

I have been fortunate to be friends with Mike Garrett: outstanding engineer, talented artist, elite cyclist, and one of the most humble individuals I have met. He has taught me a tremendous amount about living on, and perhaps more importantly, living off the bike. I am also grateful for my friendship with Geoff Olynyk, with whom I have shared many insightful, wide ranging discussions and an excellent two week research stay in Torino Italy, where we mainly performed a number of exhaustive investigations into the local beverages and cuisine. I'd like to extend my thanks to Dan Brunner for his friendship over the years; the office has not been the same since his departure for the Netherlands. Rounding out the inimitable NW17-135 office, I am grateful to count Bob Mumgaard as a friend and colleague, as his uncompromising drive and precision science has challenged me to always present my best.

Finally, John Rice has welcomed me into his home and his mountain retreat on a number of occasions, always with excellent food, drink, and laughs. I am grateful for his continuing friendship and willingness to snowshoe with me no matter how great the distance.

Contents

List of Figures

15

List of Tables

Introduction

The production of electricity from controlled nuclear fusion is a promising non-fossil fuel-based technology that could supply a substantial portion of global energy demand in the second half of the twenty first century and beyond [1]. In magnetic confinement fusion, a toroidally shaped thermonuclear plasma is confined with strong magnetic fields in order to isolate the confined 100 million degree plasma from the material boundary layer. In between, a relatively cold boundary plasma ($\lesssim 100$ eV) exhausts heat and plasma particles to the material surfaces, which are in turn recycling adsorbed neutral atoms and sputtered impurities into the plasma. The result is a strong physical coupling between the confined plasma and the surrounding plasma-facing components (PFC) that can profoundly effect the performance of both. Understanding the physics of this dynamic system, known as plasma-material interactions (PMI), and qualifying materials solutions for reactor-relevant conditions is recognized as one of the key scientific challenges for magnetic fusion energy [2].

Achieving a comprehensive understanding of PMI, however, has been severely hindered by an asymmetry in experimental diagnosis. The theory of plasma measurement techniques has been well developed, and a plethora of plasma diagnostics routinely measure the key physical characteristics of the boundary plasma [3]. In contrast, dedicated instrumentation for PFCs has been sparse. That which has been deployed is typically restricted to very small areas of protected PFCs, limited in measurement capability, and resource intensive, requiring either atmospheric entry inside the fusion device or dedicated run time [4].

To address this critical instrumentation need, a novel PFC surface diagnostic technique has been developed on the Alcator C-Mod tokamak at the MIT Plasma Science and Fusion Center. The technique - Accelerator-based In-situ Materials Surveillance, or AIMS - employs a linear charged particle accelerator and particle detectors to remotely measure the critical PMI effects on PFC surfaces such as fusion fuel retention, PFC erosion and redeposition, and material mixing. Unlike many of current PFC surface diagnostics, the technique is not destructive to the PFCs and is not disruptive to plasma or facility operations. Most importantly, AIMS can remotely interrogate large fractions of the total PFC surface area in the toroidal and poloidal direction for measurement, imparting the capability to cartographically map the isotopic surface composition over the all of the accessible PFC surfaces inside the fusion device. With an optimized AIMS diagnostic, these measurements could be achieved with an

approximately 2 cm spatial resolution and on a plasma-shot-to-shot timescale, providing a quantum leap forward in the experimental study of PFC surface effects in PMI science.

Purpose and structure of this thesis

The principal scientific purpose of this thesis is to lay the foundation for the adaptation of AIMS as one of - if not *the* - standard experimental technique for the in-situ diagnosis of PFCs on magnetic fusion devices. In order to do so, this thesis will enumerate the motivation, implementation, validation, and early experimental measurements of the AIMS diagnostic on Alcator C-Mod in a comprehensive and well documented paper. Between the material contained in this thesis and in referenced scientific literature, it is hoped that the reader will possess a sufficient understanding of the AIMS technique, experimental hardware, and data analysis methods to begin the process of installing an AIMS diagnostic at their own magnetic fusion facility.

The structure of this thesis largely follows the chronology of developing any novel scientific instrument: motivation, implementation, validation, first results, and future work.

Chapter 1 briefly reviews the principle PMI processes and that are expected to be critical for the success of next step magnetic fusion devices: the retention of the deuterium and tritium fusion fuel in PFC surfaces; the net erosion and redeposition of bulk PFC material; and the migration of eroded PFC material and and subsequent mixing with plasma fuel, sputtered impurities, and other wall materials on the PFC surface.

Chapter 2 briefly reviews the state of experimental, *in-situ* PFC surfaces diagnostics in magnetic fusion devices. The limitations of each diagnostic represent the motivations for the development of a truly novel technique such as AIMS.

Chapter 3 presents a conceptual overview of AIMS, explaining the underlying measurement theory and capabilities at a relatively high level, putting aside the details of the the experimental hardware and data analysis until the following chapter.

Chapter 4 discusses the specific details of the AIMS diagnostic on Alcator C-Mod in detail. A physical description of the radiofrequency quadrupole (RFQ) accelerator, data acquisition system, and particle detectors is contained in this chapter, as well the digital pulse processing and analysis methods used to analyze the output of the detectors.

Chapter 5 overviews two computational modeling codes that were essential in the development of the AIMS diagnostic on Alcator C-Mod. The first is a 3D beam

trajectory code that models the interaction of the deuteron beam centroid from the RFQ accelerator with the magnetic field of Alcator C-Mod; the second is a comprehensive Monte-Carlo synthetic diagnostic that is capable of simulating all aspects of an AIMS measurement on Alcator C-Mod, in particular the scattering and detection of the induced neutrons and gammas inside the fusion device.

Chapter 6 presents experimental validation activities that were conducted on the AIMS diagnostic *ex-situ* in an offsite facility and *in-situ* on the Alcator C-Mod tokamak.

Chapter 7 presents the first AIMS measurements of deuterium retention on a magnetic fusion device. The first ever measurements were acquired intrashot during plasma operations and in between wall conditioning experiments.

Chapter 8 concludes the thesis by presenting a summary of key results and enumerating the most important area of future development. The chapter closes by speculating on the potential role of AIMS in PMI science.

Key contributions presented in this thesis

The successful deployment of the AIMS diagnostic on Alcator C-Mod was the result of extensive efforts by a group of talented collaborators. As a consequence, for the purposes of this thesis, it is important to distinguish the author's role in the development of AIMS and the underlying science contributions. While these are presented in the main body of this thesis, it is appropriate to highlight them concisely here:

The author's role in AIMS

- Led the design of the AIMS diagnostic on Alcator C-Mod, including the selection of much of the experimental equipment and the optimized physical arrangement of the diagnostic in the Alcator C-Mod experimental hall.

- Determined the required particle detectors. Worked with external companies or fabricated the detectors in-house. Has begun work on a novel type of neutron detector that will advance the diagnostic capabilities of the AIMS diagnostic on Alcator C-Mod.

- Determined the requirements of the data acquisition system (DAQ) for the AIMS diagnostic and built the system from scratch.

- Wrote a comprehensive software framework for the DAQ that was customized for the AIMS measurements and provided user-friendly real-time data acquisition and offline analysis tools.

- Developed a comprehensive Monte Carlo synthetic diagnostic that is capable of simulating all aspects of the AIMS measurements. The simulation was used to optimize the AIMS diagnostic, including the design and location of the detectors and providing insight into the experimental response of the detectors. It is will also play a crucial role in advancing the future measurement capabilities of AIMS by guiding the interpretation of experimental data and the extraction of absolute isotopic concentrations from the measurements.

- Led the development of data analysis methods and software tools for extracting PFC surface information from the experimental detector spectra.

Science contributions

- The successful demonstration of AIMS represents a significant advance in the experimental diagnosis of materials in magnetic fusion devices and could lead to new understanding in PMI. The results have been published in [5].

- Provided the first time-resolved, localized AIMS measurement of deuterium retention in a magnetic fusion device during plasma operations. The measurements provide experimental evidence to support the theory that the plasma erodes and redeposits deuterium-saturated boron layers on top of the PFCs. The finding is important because it eliminates deuterium codeposition in boron layers as the responsible PMI mechanism for the *net* deuterium retention observed in Alcator C-Mod.

- Presented the first time-resolved, localized AIMS measurements of the relative changes of boron and deuterium at four distinct locations on the inner wall PFCS of Alcator C-Mod during wall conditioning experiments. The result is important because it experimentally fulfills the promise of the AIMS technique to provide cartographic mapping of the changes of the isotope content on the accessible PFC surfaces as a function of time. Such data will be crucial to advance experimental PMI science and to use in the development of computational PMI codes that are critical for magnetic fusion energy reactor development.

- Developed a new method for the high-fidelity simulation of organic scintillation detectors. For the first time, the method enables the simulation of detector response functions and pulse shape discrimination capabilities for detectors of arbitrarily complex geometry and light readout configurations; the simulation can be performed within a larger experimental geometry to capture the realistic complexities of detection. Importantly, the method is now included in the world-leading Monte Carlo simulation toolkit of particle, nuclear, space, and detector physics, Geant4. The results have been published in [6].

Chapter 1

Plasma-material interactions in magnetic fusion devices

From Lyman Spitzer's recognition in 1951 that sputtered impurities from the plasma-facing component (PFC) surface could degrade or collapse magnetic plasma confinement [7] to recent world record fusion performance on the TFTR and Alcator C-Mod tokamaks due to special PFC surface treatments [8, 9], the magnetic fusion community has long recognized the inextricable link between the confined thermonuclear plasma and the material boundary layer. The dynamic physical coupling between the two systems, known as plasma-material interaction (PMI), is composed of a number of physical processes that can significantly modify the plasma physics performance and the engineering viability of the materials.

PMI in magnetic fusion devices is an enormously complex field, encompassing the boundary plasma, the scrape off layer (SOL), sheath plasma, and the PFC material surfaces. As will be discussed in detail in Chapter 2, a relative paucity of PFC surface diagnostics relative to the mature suite of plasma diagnostics presently deployed on magnetic confinement devices has led to tremendous difficult in fully characterizing this system. Therefore, the purpose of the present chapter is to briefly review those physical mechanisms of PMI that lead to the most severe PFC surface modifications in order to understand what is required to experimentally diagnosis the PFC surfaces. For an exhaustive review of PMI in magnetic fusion devices, the reader is referred to [10] and [4].

1.1   A brief overview of PMI

PMI in magnetic fusion devices is primarily driven by the movement of heat and charged plasma particles from the thermonuclear core plasma to the boundary materials; this process is shown in Figure 1-1. Cross-field transport carries the heat and
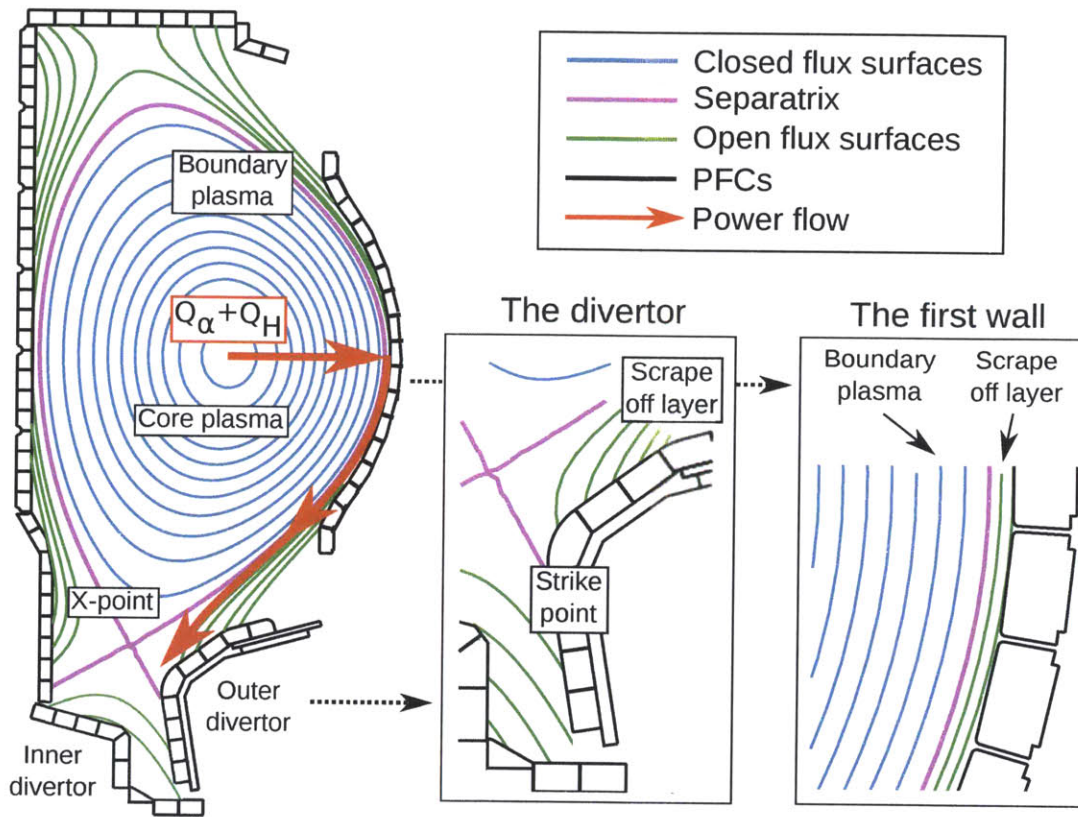
Figure 1-1: A cross section of a toroidal magnetic fusion device showing how heat generated by fusion alpha heating (Q_α), heat deposited by external heating sources, (Q_H), and plasma particles (fusion fuel ions, helium-4 nuclei generated by fusion, and impurity ions) from the plasma core drive PMI at the material boundary layer. Cross field transport carries the heat and particles, or power, across the separatrix into the scrape off layer, where parallel transport along the diverted magnetic field lines exhausts it to material surfaces. Because of the power channeling, the most intense PMI occurs near the strike point in the divertor.

particles generated from thermonuclear fusion, as well as any heat from external heating sources, radially outward from the core plasma to the boundary plasma. From the boundary plasma, the power crosses the separatrix, or last closed flux surface, into a narrow region known as the scrape off layer (SOL). Because of the geometry of open field lines and the dominance of parallel transport over cross field transport, the SOL acts as an exhaust channel, rapidly transporting power along magnetic field lines towards a material surface. These surfaces, known as limiters in limited magnetic topologies and divertors in diverted magnetic topologies, are specifically designed for the intensity of the concentrated heat and particle fluxes. Divertors, in particular, use a combination of geometry, SOL path length, plasma cooling, and robust materials to reduce the impact of PMI. Nevertheless, the physical coupling between the plasma and the materials results in an complex, dynamic system that can have severe consequences on the confined plasma and boundary materials.

Perhaps the greatest challenge of PMI is to achieve an integrated scientific understanding of this system across the enormity of the time and spatial scales involved in the underlying physical mechanisms and material responses. The PMI phase space is depicted graphically in Figure 1-2, which locates the characteristic time and length scales of the plasma, material, and interaction mechanisms. Processes like the implantation of plasma ions or the sputtering of material occur extremely fast ($\lesssim 10^{-8}$ s) and at the atomic level ($\lesssim 10^{-8}$ m). In contrast, short-length scale material responses, such as neutron- and ion-induced defect production and nanostructure growth, span microseconds to years; long-length scale responses, such as grain structure changes or neutron-induced modification to thermomechanical material properties, can range from milliseconds to years in time. The most critical issues effecting the PFC surfaces are described in detail in the following section.

1.2   Critical material issues in PMI

The principal mechanisms behind PMI take place in the thin region ($\sim$mm) of plasma immediately adjacent to the PFCs, known as the plasma sheath, and in the first few monolayers ($\sim$nm) of the material surface; these mechanisms are particularly intense at the divertor PFC surfaces. The PMI processes and PFC responses that occur in this region are depicted in Figure 1-3 and will be described in detail in the following section.

From the perspective of modifications to the materials used in the boundary layer of magnetic fusion devices, the most important effects are the bulk retention of fusion fuel, the net erosion of the material, and the material migration, redeposition, and mixing that occurs after eroded material has left the surface. Each of these effects is discussed in greater detail in this section.

23
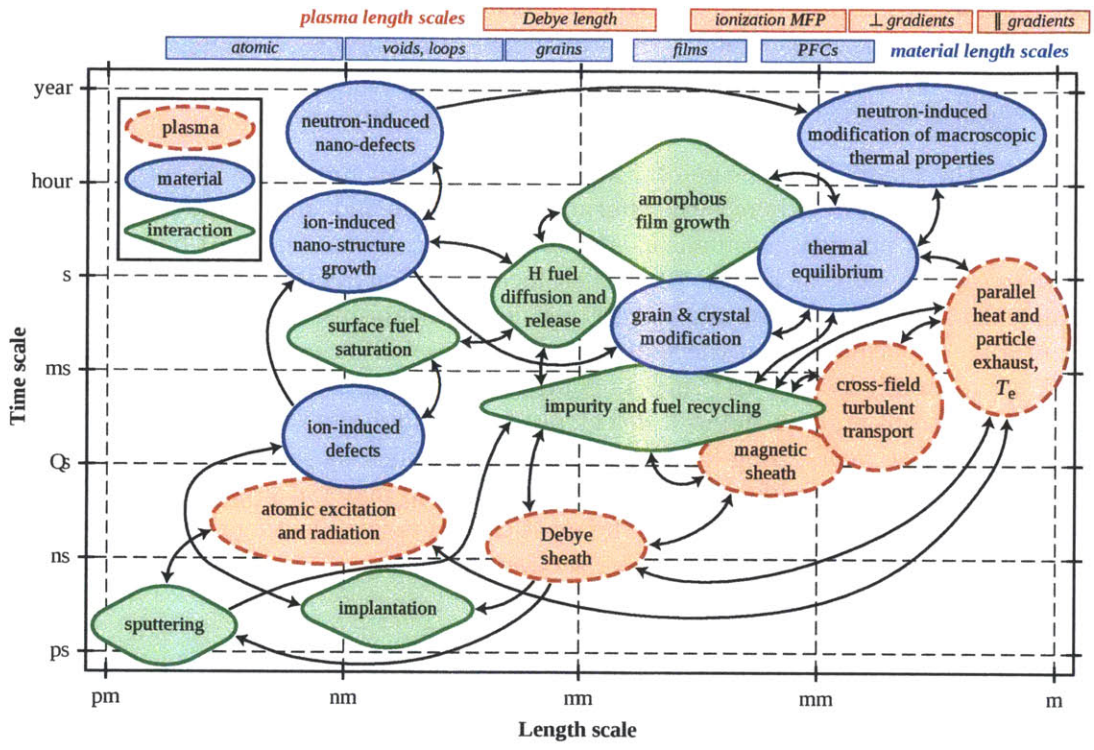
Figure 1-2: The PMI phase space showing the characteristic time and length scales of the physical processes that impact the plasma, materials, and interaction dynamics in magnetic fusion devices (Figure adapted from [11]). The physical interaction mechanisms between the plasma and material are shown in greater detail in Figure 1-3.
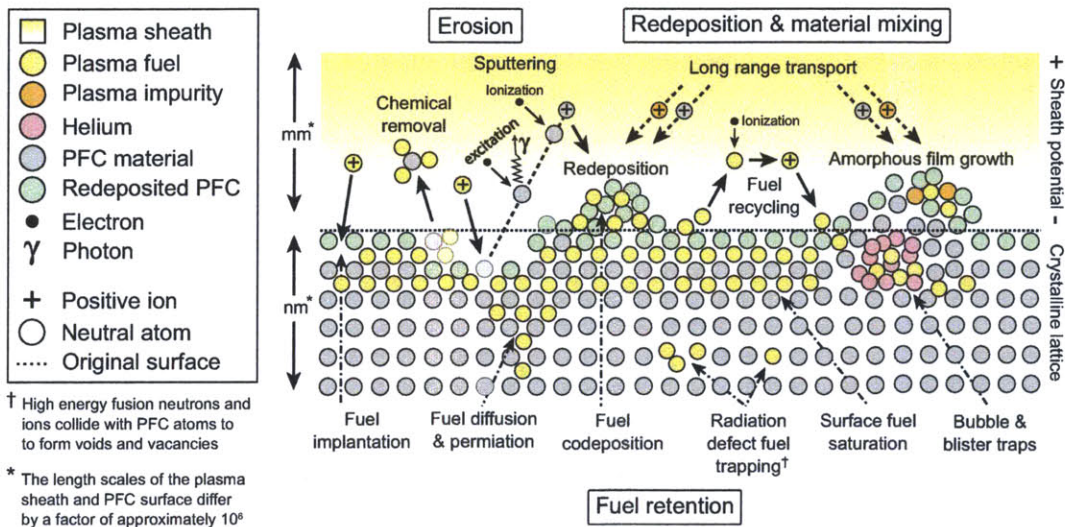
Figure 1-3: An illustration of the principle mechanisms of PMI and their physical impact on the PFC material surface. Erosion (top left) leads to the removal of PFC surface material, where it can be promptly redeposited (top center) or remotely deposited after long range transport in the boundary plasma (top right). A wide range of physical mechanisms cause plasma fuel retention (bottom) in the original PFC material or in redeposited material layers. Figure adapted from [12].

1.2.1 Fuel retention

Deuterium (^{2}H or D) and tritium (^{3}H or T) nuclei are the fuel used in fusion. While deuterium is a stable isotope and available in relative abundance on Earth, tritium is radioactive and not found naturally on Earth except for trace amounts produced by cosmic rays in the atmosphere. With a half life of 12.3 years, tritium fuel reserves will decay at a rate of approximately 5.5% per year. A future fusion power plant will, therefore, be required to breed at least as much tritium as it consumes, leading to the requirement that essentially zero tritium can be retained in the vacuum vessel in order to maintain the fuel supply. In addition, the radioactivity of tritium - which decays into helium-3 via beta emission - presents a significant nuclear hazard were it to accumulate in large quantities. In ITER, for example, nuclear regulations limit the total in-vessel supply of retained tritium to one kilogram. Thus, fuel retention in PFCs represents a significant challenge for future D-T burning fusion devices.

The primary driver of fuel retention is the energetic bombardment of and subsequent implantation in PFCs by plasma fuel ions. Ions accelerated through the plasma sheath potential gradient will have a kinetic energy of approximately $3Z_iT_e + 2T_i$, where Z_i is the ion charge, and T_e and T_i are the electron and ion plasma temperatures in the sheath. For fuel ions at a divertor surface with a T_e of 1 - 50 eV, kinetic energies typically range between 10-300 eV. Fuel ions can also charge exchange with neutral atoms in the sheath, leading to maximum kinetic energies up to a few keV. At these energies,

fuel implantation occurs in the first 3-30 nm of the PFC surface for low-Z PFCs (*e.g.* graphite, carbon-fibre composites (CFC), beryllium) and somewhat less for high-Z PFCs (*e.g.* molybdenum, tungsten). After entering the PFC surface, the energetic fuel ions thermalize through collisions, sometimes causing radiation-induced material defects, and then neutralize into atoms typically settling into interstitial lattice sites or induced defect sites [4]. The high ion fluences to PFCs - $\sim 1 \times 10^{24}$ m^{-2} s^{-1} in a reactor - results in the first atomic monolayers of the PFCs to become completely saturated in deuterium and tritium fuel as well as helium produced in the fusion reactions.

Once implanted in the PFCs, the retention of fuel (hydrogen, deuterium, tritium) in the PFC surfaces is caused by a variety of physical mechanisms. In metal PFCs, the fuel transports through the material due to thermally activated diffusion, which, for hydrogenic species, occurs at and above room temperatures for most metals [13]. Diffusing fuel will saturate the interstitial sites of the first few surface monolayers and also become energetically trapped in the potential wells of radiation-induced vacancies and voids in the metal lattice. Helium bubbles, formed by the implantation of fusion alpha particles, the decay of retained tritium to helium-3, or (n,α) nuclear reactions induced by the 14.1 MeV fusion neutrons have also been shown to be a substantial mechanism for fuel trapping [14]. For carbon-based materials, codeposition is the primary retention mechanism, which is the trapping of surface fuel ions in redeposited and growing layers of eroded PFC materials.

Fuel retention has important consequences not only for the PFC materials themselves but also for plasma operations. Fuel saturation of material surfaces and thermal desorption result in fuel recycling between the wall and plasma. The result is a loss of plasma fueling efficiency, plasma density control, and high levels of neutral hydrogen density, ultimately effecting the particle and energy confinement of the core plasma. For deuterium-tritium burning magnetic fusion devices, the bulk retention of tritium in invessel materials is a serious nuclear safety concern and a facility operations issue since a limited onsite inventory requires high-levels of tritium recovery for sufficient plasma fueling [15].

1.2.2 Erosion

The physical processes that remove PFC surface material in magnetic fusion devices can be classified into two categories: transient events and steady-state surface loss. Transient events deliver high power densities to material surfaces during undesirable off-normal plasma events, causing macroscopic material loss. In contrast, steady state surface loss is caused by physical and chemical interactions on the atomic scale that are always present in magnetic fusion devices.

Transient events include a wide range of short time-scale plasma events that can deliver high power densities to material surfaces, especially in the divertor. In type

I edge localize modes (ELMS), a sudden collapse of the pressure gradient caused by microinstability-driven turbulence leads to strong power loss across the separatrix of 2 6% of the total plasma stored energy with up to 80% being deposited on the divertor PFCs between 0.1-1 ms [16]. Plasma disruptions are another important transient event. Disruptions cause a rapid loss of plasma confinement, resulting in the stored energy of the plasma being dissipated into the vacuum vessel and PFC surfaces, often in the divertor.

The result of transient events is typically melting (for metallic PFCs) and ablation (for carbon-based PFCs), which leads to a direct macroscopic erosion of the surfaces. For metal PFCs such as molybdenum, tungsten, and beryllium, the melt layer that occurs during transient events is exposed to a host of forces during melting, such electromagnetic, gravitational, vibrational, and ablation recoil [17]. These forces, in combination with the liquid loss during melting, control the erosion dynamics and set the fundamental lifetime limits on metallic PFCs. CFC or graphite PFCs, however, sublimate rather than melt at high temperatures but experience reduced erosion rates compared to metallic PFCs due to shielding by the ablated material [4]. The magnitude of erosion during transient events is a function of the deposited energy, deposition area, and deposition time [18].

Unlike transient event-induced erosion, sputtering represents a steady-state source of erosion to PFC surfaces that is due to the physical bombardment of plasma ions and the chemical interaction of atoms on the PFC surfaces. In physical sputtering, plasma ions accelerate through the plasma sheath electrostatic potential or charge exchange with neutrals as described above, with the kinetics of surface bombardment leading to ejected surface atoms. In chemical sputtering, hydrogenic plasma ions react with carbon-based PFCs such as graphite or CFC to form volatile hydrocarbon that are loosely bound to the surface and have greatly reduced sputtering threshold energy. Erosion by chemical sputtering is a function of the incident particle energy and flux, the surface temperature, and the PFC composition and atomic structure [4].

1.2.3 Material migration and mixing

The movement of material in a magnetic fusion device is primarily carried out through particle transport in the boundary and divertor plasmas of material that has been eroded from PFC surfaces. Neutral atoms of retained plasma fuel, plasma impurities, and PFC material leave the PFC surface through sputtering or desorption. Neutrals rapidly become charged ions through ionization, charge exchange, and dissociation with electrons in the boundary and divertor plasma. As ions, the particles become subject to plasma transport, either promptly returning to the PFC surface (prompt redeposition) or transported along local magnetic field lines for deposition elsewhere on the first wall (remote redeposition).

Whether a particle deposits locally or remotely is a complex function of ion tempera-

ture gradient forces, plasma flows towards material targets, the first wall and divertor geometry, and the origin of the neutral atom (limiter, first wall, or divertor) [10]. For diverted tokamaks, the general erosion/redeposition behavior can be described by material migration from the first walls and limiters to the divertor, with *net erosion* occuring at the outer divertor and *net redeposition* on the inner divertor. This behavior has been experimentally demonstrated in the JET, ASDEX-Upgrade, and DIII-D tokamaks despite differences in geometry, size, and PFC material [19, 20].

Further complicating material migration in modern tokamaks is the presence of several material elements at the plasma-material interface. Multiple PFC materials, such as beryllium and tungsten, can be used at different regions in order to exploit the unique PMI and thermomechanical properties of each material. Thin film coatings of PFCs, such as boron on molybdenum (Alcator C-Mod) [9] and lithium on CFC (NSTX) [21], provide an additional source of non-PFC materials. The steady-state cycle of erosion, migration, and redeposition in a multiple-material environment can lead to the formation of solid materials with complex - and often undesirable - compositions, typically referred to as "tokamakium" [22].

The mixing of materials has significant consequences for the PFCs. Because the mixed material layers form on the PFC surface, they can substantially alter the dynamics of PMI, leading to higher rates of sputtering erosion, enhanced fuel retention, changes in fuel recycling, and reduced PFC lifetimes [4, 23]. A second consequence of material mixing is an alteration to the macroscropic thermomechanical properties of the PFCs themselves due to changes in surface morphology and composition. Issues such as reduced melting temperature, reduced power handling, and increased brittleness in alloyed mixed material metals fundamentally alter the intended engineering function of the materials [24].

1.3 PMI in next step fusion devices

The advances in understanding and mitigating PMI effects *of* materials on the confined plasma have been responsible for a significant improvement in plasma physics performance. The study of PMI effects *on* materials, however, has received substantially less scientific attention despite the strong influence of material conditions on plasma performance. This shortcoming is of particular concern for the next generation of magnetic fusion devices that will push towards reactor-like conditions.

Plasma pulses in present tokamaks are relatively short ($\sim$seconds / pulse), have small cumulative exposure times ($\sim$1000 s / year); the short pulse times mean that the heat flux to materials ($\lesssim$10 MW m^{-2}) can be dealt with by inertially cooled PFCs. In such conditions, PMI impacts from steady-state fuel retention, erosion, and material migration are essentially negligible in terms of the PFC performance, although transient events such as ELMS and disruptions can cause severe damage. In contrast, the path to a steady-state fusion energy reactor, will add several orders of magnitude to

pulse duration ($\gtrsim$1000 s / pulse), cumulative exposure time ($\gtrsim 10^5$ s / year), and incident heat flux ($\sim$10 MW / m^2); the long or steady-state heat fluxes must be handled by actively cooled PFCs. The deleterious, steady-state PMI effects that are only partially observed or accessible in present devices will become critical for the physics of plasma confinement as well as the engineering of robust material structures[4]. In order to advance fusion energy towards a realistic commercial power plant, a more comprehensive understanding of PFC materials and PMI processes is required.

Chapter 2

The State of PFC surface diagnosis in PMI science

A comprehensive understanding of PMI science requires the simultaneous characterization of the thermonuclear plasma and the PFC surfaces through experimental measurements; however, an asymmetry in PMI diagnostics, which has heavily favored measurements of the plasma over the PFCs, coupled to the inadequate capabilities of present PFC surface diagnostics has severely hindered these efforts. While the theory of plasma measurement techniques has been well developed and a plethora of plasma diagnostics routinely measure the key physical characteristics of both the core and boundary plasma [3], dedicated instrumentation for the PFC surfaces in magnetic fusion devices has been comparatively sparse.

The purpose of the present chapter is to examine the present state of PFC surface diagnostics and to better understand the requirements for the next generation of diagnostics that will be required to advance PMI science.

2.1 Diagnostic challenges

One of the historic difficulties with the deployment of dedicated PFC diagnostics has been the lack of necessity to fully understand and mitigate PMI effects on current devices. As discussed in Chapter 1, next generation magnetic fusion devices will require several orders of magnitude increases in total plasma energy, pulse time, and integrated run time. The consequence will be profound changes in the material composition and structure, which, in turn, will impact the confinement and stability of the plasma. At present, the uncertainties in PMI science are so large as to preclude the predictive modeling of effects on the plasma and materials under these conditions [25].

Another primary difficulty for PFC diagnostics is the extraordinary scales involved

31

in PMI. Spatially, PMI spans processes such as sputtering or ion implantation that occur on atomic scales (10^{-12} m to 10^{-9} m) to processes such as net plasma erosion of bulk PFC material that occur on the macroscopic scale (10^{-3} m). Temporally, PMI spans an even greater range, extending from nearly instantaneous effects of sputtering (10^{-10} s) to retained fusion fuel recycling (10^{-3} s) to steady-state plasma exposure in a reactor environment ($\gtrsim 10^{8}$ s).

Practically, the large temporal range in PMI processes has led to a division in the diagnosis of "instantaneous" and "long term" effects. Instantaneous PMI processes primarily affect the local and global plasma parameters through the control of line radiation from the plasma boundary, fuel recycling from the PFC surfaces, and core fuel dilution due to impurities from the PFCs. Experimental diagnostics, such as optical emission spectroscopy and mass spectroscopy for PMI have largely focused on these instantaneous processes because their impact on the plasma aligns with the core plasma physics mission of present day tokamak [4].

In contrast, long-term PMI effects primary impact the engineering viability of the PFCs, the ability to mitigate deleterious effects on the plasma, and the operating characteristics of a steady-state power plant, such as wall temperature, plant availability, component lifetime. Realizing fusion energy as a commercially viable energy source fundamentally depends upon an understanding of these long-term PMI processes, which have been underdiagnosed in magnetic fusion devices and present a substantial opportunity for innovating experimental techniques. Therefore, the remainder of this chapter will be dedicated to evaluating the PFC surface diagnostics that have been used to study long-term PMI effects in order to set the stage for the development of Accelerator-based In-Situ Materials Surveillance, which is the focus of the remainder of the chapters in this thesis.

2.2   Present PFC surface diagnostics

Experimental diagnostics for PFCs in magnetic fusion devices can be broadly classified into two categories: *ex-situ* diagnosis, in which PFC materials are removed from the device for measurement after an extended period of plasma exposure; and *in-situ* diagnosis, in which instrumentation is deployed on the magnetic fusion device itself to measure PFC materials in their native environment. Historically, experimental PMI science has been dominated by *ex-situ* diagnosis, primarily due to the greater range of applicable techniques and far simpler experimental implementation available in a dedicated, offsite facility compared to the magnetic fusion device.

2.2.1 Ex-situ diagnostics

One of the most successful and widely applied experimental techniques for the study of material surfaces that have been modified by PMI has been the application ion beam analysis (IBA) [26]. IBA uses $\sim$MeV ion beams in a variety of ion scattering, nuclear reaction, and atomic physics techniques to infer elemental and isotopic composition of the material surface. For the analysis of fusion materials, PFCs are removed from the fusion device during the vacuum breaks that occur at the end of the experimental plasma campaign and brought to a dedicated offsite ion beam facility for analysis [27]. The PFCs have, therefore, been exposed to plasma under a variety of conditions for several months to several years of facility operations. Although it is considered the gold standard in PFC diagnosis, IBA is an intrinsically "archaeological" measurement that folds the PMI dynamics of an entire plasma campaign into a single temporal measurement of the PFC surface composition, preventing the linkage between discrete plasma conditions and the PFC surface response. In addition, IBA is spatially limited to the PFCs that are able to be extracted from the first wall, can be resource intensive for the fusion facility, and may allow changes in surface composition between exposure and measurement due to facility operations, the PFC removal process, or atmospheric exposure. Other *ex-situ* nuclear techniques neutron activation analysis and electron spectrocopy of the tritium decay electrons have also been applied.

Another method that has recently been applied for interrogating fusion materials is the use of high-powered lasers to ablate the PFC surface in order to perform optical spectroscopy of the ejected matter. For example, in Laser Induced Breakdown Spectroscopy (LIBS), laser pulses — varying between 10^{-9} s and 10^{-15} s and above a few J cm^{-2} depending on the experimental conditions — ablate surface material to produce a plasma. Atomic emission spectroscopy and spectral analysis algorithms of the optical plasma radiation then provide chemical identification and quantification of the material surface [28]. LIBS requires essentially no sample preparation and has been shown under laboratory conditions to be highly suitable for the study of the PMI-induced effects [29, 30]; however, advances are required in the spectral analysis algorithms to correctly reconstruct the material surface composition, especially when absolute (or "calibration free") measurements are required [28]. Other laser-based techniques such as laser-induced ablation spectroscopy (LIAS) and laser-induced desorption spectroscopy (LIDS) have also been successfully applied to the analysis of PFC surfaces in the laboratory [29, 31]. The high laser powers required for these techniques have the undesirable effect of destroying the surfaces under interrogation.

2.2.2 In-situ diagnostics

The instrumentation that has been deployed on magnetic fusion devices for *in-situ* PMI studies can be further classified into *global* diagnostics, which provide a single measurement of a particular physical property in order to characterize all PFC surfaces as a whole, and *localized* diagnostics, which provide spatially resolved mea-

surements of a particular physical property potentially on different PFCs.

Global diagnostics, such as thermal desorption spectroscopy (TDS) [32], rely upon the extraction and subsequent measurement the PFC impurities of interest as a neutral gas after being desorbed from the PFC surface during controlled heating. Other methods, such as the static gas balance method used at Alcator C-Mod [9], compare the total fuel injected during the shot to the total fuel pumped out after the shot to compute net fuel retention. Such methods have principally been used to successfully investigate the net global balance of hydrogenic fusion fuel isotopes (hydrogen, deuterium, tritium) in response to various plasma conditions and fuel removal techniques such as disruptions. However, these global techniques intrinsically provide no spatial localization, which is critical to understand PMI, and can require facility intensive operations, such as high temperature baking to desorb impurities from the PFCs. In addition, such techniques have difficulty localizing the retention in time during transient plasma events.

In contrast, a number of localized PFC diagnostics can provide spatially resolved measurements. Quartz microbalances (QMB) exploit the change in the crystal's resonant vibration frequency due to the subtraction/addition of surface-deposited material, making it a useful erosion/redeposition measurement tool. QMB diagnostics have been successfully deployed, for example, on the JET tokamak at Culham, U.K. [33] and the NSTX tokamak at Princeton, U.S.A [34]. Despite instantaneous time resolution and $\sim$1 nm depth resolution, QMBs are limited in dynamic range and are affected by temperature changes. QMBs are insensitive to the isotopic surface composition of the material under measurement, complicating the analysis where the material composition is unknown or changing in time. The most limiting factor, however, is that QMBs are highly temperature sensitive, requiring location in heavily shielded regions away from the plasma and limiting the surfaces available for measurement.

Another localized erosion/redeposition diagnostic that has been deployed on DIII-D tokamak at San Diego, U.S.A. is colorimetry [35]. Colorimetry infers the change in surface material by measuring the interference color patterns from incident white light on transparent surface films. While it provides time-resolved two dimensional erosion/redeposition measurements remotely, colorimetry is limited to $\sim$ μm in depth resolution and strongly dependent on complete knowledge of the optical properties of the surface film, which can be modified by plasma exposure [4]. Active intervention is required to produce or replenish the films under interrogation.

A different approach to the localized *in-situ* diagnosis of PMI has been the use of remote manipulation systems to introduce representative PFC material coupons into the magnetic fusion device for exposure to relatively short, well-characterized plasmas [36]. For example, the DiMES and MiMES systems at the DIII-D tokamak allow small ($\lesssim$10 cm^2) samples to be inserted on extendable probes for exposure at a single location in the divertor and midplane, respectively [37]. After exposure, the samples are removed and typically analyzed with *ex-situ* IBA, although LIBS, TDS, or other material analysis methods can be applied. While such an approach has significantly

advanced an understanding of PMI science, it is extremely limited in terms of geometric access and total exposed PFC surface area ($\lesssim 10$ cm^{-2}), and the short exposure times do not reflect the PFC compositions that would result from long-term exposure in the mixed material environments of magnetic fusion devices. Hard to acquire and expensive run time must be dedicated to such techniques, severely limiting the dynamic range of plasma conditions and material responses that can be investigated [4].

2.3 The need to advance PFC surface diagnosis

The PFC surface diagnostics discussed in the previous section have significantly advanced an understanding of plasma-material behavior during the previous decades. Unfortunately, the present suite of diagnostics is largely incapable of making highly time and space resolved surface measurements of the net processes over a large portion of the exposed PFC surfaces in magnetic fusion devices. The consequences have primarily been twofold. First, the relatively restricted measurement capability, coupled with the inability to routinely measure PFC responses to the wide variety of standard plasma operating conditions, has resulted in a lack of a more comprehensive physical understanding of the PMI processes involved. Second, the absence of comprehensive PFC surface measurements precludes use of data to guide the development and validation of PMI simulation codes that are considered essential in designing the next generation of magnetic fusion experiments [4].

2.3.1 Limitations of existing diagnostics

The previous section elicits the four main limitations of present materials diagnostics. First, the insensitivity to or dependence upon the material composition complicates the extraction of absolute isotopic concentrations in an environment where the plasma is continually remaking the surface through erosion, migration, and redeposition of potentially mixed materials. Second, the unacceptably large or complete lack of spatial resolution inhibits an understanding of the effects of PMI processes on localized surfaces and prevents the acquisition of much-needed experimental data for use in modeling PMI [25]. When existing diagnostics do have spatial resolution, they tend to be limited to only one or two very small areas of the entire PFC surface. This is particularly problematic because unlike the axisymmetric core plasma of a tokamak, the material boundary is intrinsically a 3D structure, leading to both toroidal and poloidal variations in PFC surface effects.

Third and related, the lack of time-resolved PFC surface measurement prevents the ability to link discrete conditions in the plasma with highly resolved, localized responses of the material surfaces. This issue at the core of PMI science, fundamentally determining whether an improved understanding of the plasma-material processes in-

volved can be used to mitigate the deleterious effects to materials in magnetic fusion environments.

Fourth, existing diagnostics place resource-intensive demands on the facility, often requiring vacuum breaks or dedicated, hard-to-acquire run time, and greatly restricts the quantity of experimental data that can be acquired and the dynamic range of plasma conditions under which PFC surface can be measured. Thus, new experimental techniques that address the above diagnostic shortcomings are critical for the advancement of PMI science, and it is instructive to explicitly examine the scientific product and the foundational requirements of an "ideal" PFC surface diagnostic.

2.3.2 Requirements of an ideal diagnostic

PMI in magnetic fusion devices is a four-dimensional problem: two spatial dimension (poloidal and toroidal PFC surfaces), one depth dimension (distance into the PFC surface), and one time dimension (the evolution of the PFC surfaces). Thus, to achieve to a more comprehensive understanding of PMI science, the dimensionality of the problem dictates the requirements of the data that must be experimentally produced by the diagnostic.

It is natural, then, to consider that an ideal PFC surface diagnostic would be cartographic, providing two-dimensional maps over the accessible PFC surfaces with spatial resolution on the order of the PFC tile sizes or of the gradient scale lengths for the process in question. The maps would present the quantities of interest for the PMI process under scrutiny: deuterium/tritium concentration for studying fusion fuel retention; the net change in surface height for studying erosion/redeposition; or the absolute isotopic composition for studying material mixing and migration. To account for the evolution of the PFC surface in response to plasma exposure, the PFC surface maps should be temporally resolved on time scales relevant to the long-term PMI processes of fuel retention, erosion/redeposition, and material composition changes. Finally, the diagnostic should provide some measure of depth resolution (*e.g.* into the material) on each of the measurements that form the overall maps of PFC surface composition.

The ability to produce such time and space resolved PFC surface data places four fundamental requirements on the ideal PFC surface diagnostic, which should be able to:

1. Quantify the isotopic and elemental concentrations of the PFC surface composition, as well as net erosion. Net erosion rates in current magnetic fusion devices are on the order of 0.1 - 10 nm s^{-1}; therefore, the diagnostic must have a dynamic range of 10 nm to 10 μm to accommodate the maximum net erosion rates during a plasma campaign. Depth resolution for all measurements is desirable.

2. Provide spatially resolved measurements of PFC surface compositions over a large fraction of the plasma-facing materials composing the first wall. Spatial resolution should be on the order of $\lesssim 2$ cm, which is the approximate size of PFC tiles or the gradient scale lengths of the process in question.

3. Provide temporally resolved measurements of the PFC surface compositions on a time scale relevant to the longer term effects of PMI. Because present tokamaks are pulsed, a plasma shot-to-shot time scale provides an obvious timescale for measurements although steady-state measurements at higher time resolution would be preferable.

4. Perform the PFC surface composition measurements *in-situ* without requiring dedicated run time during the plasma campaign or interrupting facility operations. Such a requirement means the diagnostic must be capable of making remote measurements without requiring a vacuum break or physical access to the PFC surface.

2.3.3 New diagnostic developments

Two recent developments in PFC surface diagnostics have made considerable progress towards such an ideal PFC diagnostics, both which attempt to exploit the success of *ex-situ* materials diagnostics by adapting their respective techniques to the environment of a magnetic fusion devices.

The first development has been the application of the laser-based techniques for the *in-situ* measurement of retained hydrogenic fusion fuel inside magnetic fusion devices. In general, fiber optics and focusing optics are used to direct an external high-power pulsed beam onto a small region of PFCs, usually located in the lower divertor or inner column. The ablated material emits strong visible light from atomic transmissions upon entering the fusion plasma or being further heated into its own plasma; the light is measured to obtain isotope quantification. Proof-of-principal experiments using LIDS have been carried out on the JET and TEXTOR tokamak in 2001 [38] and 2009 [39], respectively. A more recent proof-of-principle experiment demonstrated that LIBS could be used to study the composition of codeposited material layers in TEXTOR in 2011 [40].

The second development, which is the adaptation of IBA from the standard dedicated laboratory environment to the magnetic fusion environment, is the primary scientific contribution of this dissertation and will be discussed in detail in the following chapters.

Chapter 3

Accelerator-based In-situ Materials Surveillance (AIMS)

In order to advance PMI science, a new approach to the diagnosis of PFC surfaces inside magnetic fusion devices is required to overcome the limitations of present PFC surface diagnostics as discussed in Chapter 2. Interestingly, where traditional *in-situ* diagnostic techniques are limited (small surface area, low spatial resolution, narrow measurement techniques), *ex-situ* techniques excel (large surface area, high spatial resolution, comprehensive surface measurements). Similarly, the high temporal resolution of *in-situ* diagnostics greatly outperforms the archaeological nature of *ex-situ* diagnostics for studying the dynamic PMI system. Thus, it seems obvious to question whether the most successful *ex-situ* PFC surface diagnostic - ion beam analysis (IBA) - can be adapted for *in-situ* measurements in order to leverage the combined advantages of both diagnostic approaches.

The purpose of the present chapter is provide a general description of a novel experimental technique that does exactly that. The technique, which incorporates particle accelerators and radiation detectors directly onto a magnetic fusion device to make measurements of the PFC surface compositions, is known as Accelerator-based In-situ Materials Surveillance (AIMS). The details of the first experimental AIMS diagnostic on the Alcator C-Mod tokamak will be presented in Chapter 4.

3.1   Principles of AIMS

The quintessence of AIMS is the adaptation of standard IBA of materials from the traditional *ex-situ* laboratory setting to the *in-situ* environment of a magnetic fusion device. The essential equipment and procedural steps involved in AIMS are depicted in Figure 3-1, which shows a cross section of the Alcator C-Mod tokamak as a representative example of a magnetic fusion device.

39
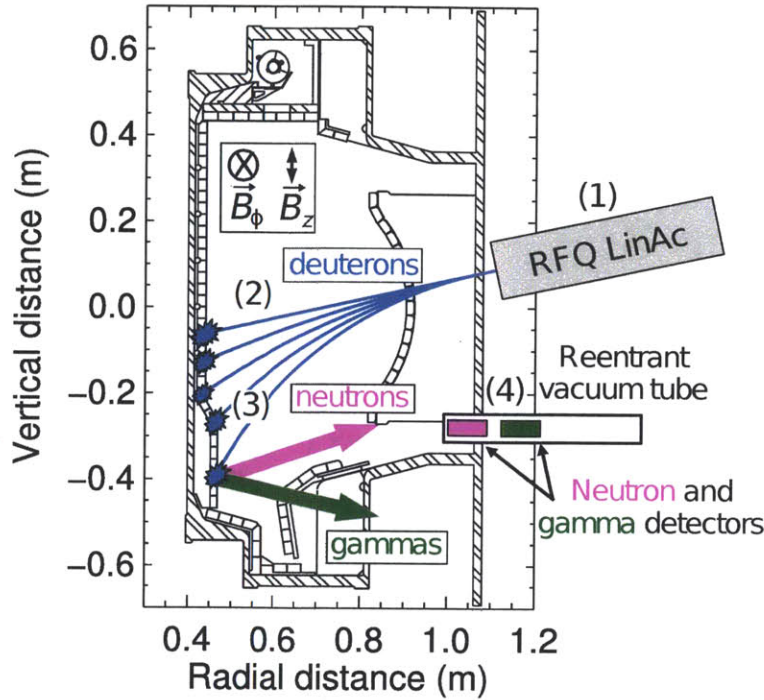
Figure 3-1: A depiction of AIMS on a cross section of the Alcator C-Mod tokamak showing (1) the radiofrequency quadrupole (RFQ) linear accelerator, (2) magnetic beam steering, (3) nuclear reactions in materials, and (4) particle detection.

A compact linear deuteron accelerator is connected to the tokamak vacuum system at one of the radial diagnostic ports. When the tokamak is not running plasma discharges, the accelerator injects a beam of ~MeV deuterons into the tokamak vacuum vessel. Using the tokamak magnetic field coils, the beam can be steered electromagnetically via the Lorentz force:

$$\mathbf{F} = q\mathbf{v} \times \mathbf{B} \tag{3.1}$$

To understand the steering mechanisms, consider a cylindrical coordinates system (r,ϕ,z) aligned with the vertical axis of tokamak toroidal symmetry. The negative radial velocity component of the deuteron beam (v_r) interacts with the toroidal (B_ϕ) and vertical (B_z) magnetic field resulting in a steering force; B_ϕ provides steering around the cross section and B_z provides steering into and out of the cross section in Figure 3-1. Constant magnetic field provides a steady-state, localized measurement at the point where the beam intercepts the PFC; controlled changes to the magnetic field move the beam to new measurement locations. The beam can effectively be swept around the inside of the fusion device, resulting in a two dimensional map (poloidal and toroidal directions) of the PFC surface isotopic content with the spatial resolution set by the deuteron beam spot size on the PFCs.

When the ~MeV deuterons impact the first wall, they induce high Q nuclear reactions with isotopes from hydrogen (Z=1) to approximately calcium (Z=20), producing high

Table 3.1: The key parameters of interest for IBA show the significant challenges that were overcome in order to adapt standard laboratory techniques for AIMS.

Parameter	Standard IBA	AIMS
Accelerator	Electrostatic, $>$m^3	RF, $\sim$0.1 m^3
Beam ion species	Z$\lesssim$26; rarely ^{2}H	^{2}H
Beam energy	Variable $\lesssim$5.0 MeV	Fixed
Beam current [nA]	$\sim$10^0-10^3	$\sim$10^6
Beam duty cycle [%]	100%	$\sim$1%
Detected species	Ions, x-rays, γ	Neutrons, γ
Detector distance [m]	$\sim$0.1	$\sim$1
Detector solid angle [sr]	$\sim$10^{-1}	$\sim$10^{-3}
Detector view	Line-of-sight	Shielded
Detector count rates [s^{-1}]	$\sim$ 10^3	$\sim$10^5-10^6
Kinematic geometry	Fixed	Variable

energy neutrons and gammas. Nearby particle detectors perform spectroscopy of the neutrons and gammas from which the isotopic content of the PFC surface can be reconstructed. Due to the penetrating nature of the neutrons and gammas, the nearby detectors do not require line of sight to the PFC measurement location. The measurement depth into the PFC surface is dependent on the incident deuteron beam energy and PFC material but is on the order of ten microns for $\sim$MeV deuteron beams in typical PFC materials.

3.2 From standard IBA to AIMS

While the basic principles remain the same - analyzing materials by detecting accelerated ion-induced nuclear scattering products - AIMS represents a significant reinvention of almost all aspects of the standard IBA that is performed *ex-situ* in dedicated laboratories; Table 3.1 illustrates the principal differences.

3.2.1 Standard ion beam analysis

In standard IBA, small beam currents, typically generated in relatively large electrostatic accelerators, are used to irradiate the material samples, resulting in manageable detector counts rates and minimum radiation risks to the operator. The beam energy can be varied, typically between $\sim$0.5 MeV to $\lesssim$5.0 MeV, enabling the experimenter to exploit energy thresholds and resonances in the reaction cross sections. The slowing of the beam in materials also provides depth resolution in some techniques. Incident beam species are typically light ions such as protons, helions, and alphas although heavier ions such as oxygen can be used in some techniques; deuteron beam are rarely used in standard IBA due to the large neutron radiation hazard that is generated by deuteron-induced nuclear reactions. While x-rays and gammas are the detected par-

ticle species in certain techniques, charged particles are preferred because of detector efficiencies approaching 1.0, straightforward data analysis, and well validated experimental techniques [41].

Perhaps the most important aspect of standard IBA is that it is performed in a dedicated environment that is optimized for the experimental techniques. The signal-to-noise ratio can be maximized by eliminating most geometric sources of scattered particles, achieving high detector statistics during long measurement periods, and locating the detectors close to the material sample to maximize solid angle. For multiple measurements over a surface, relative detector count rates can be acquired at each location and then normalized to a calibrated material standard in order to extract absolute quantities of interest such as isotopic concentration or layer thickness. The relative flexibility of the accelerator beamlines, steering magnets, and detector setup enables the operator to geometrically configure the experiment to suit the selected nuclear reactions of interest. This is particularly crucial for gamma- and neutron-based nuclear reaction analysis where almost all of the available cross section data, which exhibits strong angular dependence, is available at only a single experimental angle [42].

3.2.2   Accelerator-based In-situ Material Surveillance (AIMS)

In contrast to traditional IBA, AIMS is performed in an environment that is anything but optimal for performing IBA of materials starting with the accelerator itself. Due to the limited diagnostic space that surrounds a magnetic fusion device, AIMS must utilize a compact linear accelerator known as a radiofrequency quadrupole (RFQ) accelerator. RFQs employ resonant RF cavities with four machined axial vane structures to produce spatially varying fields near the beam axis. The specially designed field structure bunches and accelerates the beam while simultaneously providing strong transverse focusing. The combination of bunching, focusing, and accelerating with RF rather than ~MV DC voltages allows RFQ cavities to be extremely compact high current ion accelerators, typically achieving acceleration gradients of order 1 MeV/m per nucleon [43]. The compact size enables the use of RFQs for the AIMS but restricts the beam energy variability since each RFQ is fabricated for a single mass to charge ratio and final output particle beam energy although in principle micron thick stopping foils could be used to reduce the beam energy at the PFC surface.

Another major difference between AIMS and standard IBA is the necessity to perform energy spectroscopy of induced particles in the strongly adverse environment of a magnetic fusion device compared with the optimized IBA accelerator facility. The superstructure of the fusion device causes substantial amounts of downscattered particles that obscure the prompt, unscattered reaction products in detector spectra. The detectors must work in magnetic fields in order to be close to the PFC measurement locations to maximize solid angle and signal-to-noise ratio. The limited diagnostic space restricts detectors to $\lesssim 10$ cm in linear dimension, and the possibility of severe

mechanical shock from plasma disruptions necessitates robust detectors. High energy neutron fluxes during plasma shots require radiation-hard detector electronics. Finally, the use of high peak current RFQs results in instantaneous detector counts rates that can approach 10^6 pulses per second.

As will be discussed in greater detail in Chapter 4, such a hostile detection environment prevents the use of almost all standard spectroscopy detectors; however, the recent emergence of large surface area ($\gtrsim 1$ cm^2) photonic readout devices, such as the silicon avalanche photodiode (SiAPD) and silicon photomultplier (SiPM), have enabled new types of advanced scintillation crystal detectors [44]. These detectors are mechanically robust, radiation hard, operable at very high count rates, geometrically compact, and insensitive to magnetic fields, making them a feasible choice for AIMS. Inorganic scintillators, such as thallium-doped sodium iodide or cerium-doped lanthanum bromide, provide high efficiency, high resolution gamma spectroscopy; liquid organic scintillators provide similar detection performance for fast neutrons.

Despite the advance in detectors, the necessity to perform spectroscopy *in-situ* on the magnetic fusion device ensures that the acquired particle spectra will have relatively low signal-to-noise ratios due to the unavoidable scattering of induced particles off the dense, high-Z device superstructure that surrounds the detectors. Coupled to the requirement that AIMS must detect high energy gamma and neutrons rather than charged particles - the detected particle must be able to penetrate the detector shielding required in the fusion environment - the analysis of the resulting spectra is much more difficult than standard IBA.

Another important aspect of AIMS is the dynamic nature of the reaction geometry imposed by the desire to steer the incident deuteron beam across a wide range of PFC surfaces. Although the detectors remain in a fixed location, magnetic beam steering effects the kinematics of the nuclear reactions via the angular dependence of the cross sections, the detection geometry due to the change in solid angle, and the background scattering impacts on the final energy spectra. Such variable conditions, coupled to the hostility and inaccessibility of the magnetic fusion environment, complicate the use of traditional calibration standards for extracting absolute measurements of PFC surface quantities. In place of standards, AIMS must rely on the computational modeling of the ion beam interactions with the materials and the subsequent transport of emitted particle to detectors to infer absolute material surface compositions. Such "standardless" ion beam analysis is an emerging and active research trend within the IBA community [42].

3.3   Nuclear reactions for AIMS

Nuclear reactions form the core of the AIMS technique. AIMS utilizes $\sim$MeV deuterons to induced nuclear reactions for analysis in PFC surfaces. Deuterons provide quantification of many isotopes between hydrogen (Z = 1) and calcium (Z = 20) using

43

Table 3.2: The deuteron-induced nuclear reactions that can be used to diagnose PMI shown with the corresponding detected particle type and energy. Net erosion techniques remain under development in the laboratory while the ratio of $^{12}C/^{13}C$ is proposed to monitor impurity transport physics in the boundary plasma.

PMI issue	Reaction	Particle	Energy (MeV)
Fuel retention	$^2H(d,n)^3He$	n	~2-5
	$^3H(d,n)^4He$	n	~13-16
PFC impurities	$^{12}C(d,p\gamma)^{13}C$	γ	3.089
	$^{14}N(d,p\gamma)^{15}N$	γ	1.885, 2.297
	$^{16}O(d,p\gamma)^{17}O$	γ	0.874
Net erosion	$^7Li(d,p\gamma)^8Li$	γ	0.478
	$^9Be(d,n\gamma)^{10}B$	γ	0.718
	$^{11}B(d,p\gamma)^{12}B$	γ	0.953, 1.674
Transport	$^{12}C(d,p\gamma)^{13}C$	γ	3.089
	$^{13}C(d,p\gamma)^{14}C$	γ	2.313

particle-induced gamma emission (PIGE) spectroscopy [41]; quantification of retained deuterium and tritium can be performed through particle-induced neutron-emission (PINE) spectroscopy of the neutrons emitted in accelerator-driven fusion reactions; the nuclear reactions most relevant for diagnosing PMI are shown in Table 3.2. Two types of reactions are used in AIMS, principally because they provide high energy gammas and neutrons that can penetrate the several centimeters of detector shielding that is required in the fusion environment.

3.3.1 Gamma production reactions

In the first reaction type, the incident deuteron is stripped of either its proton or neutron; the residual excited nucleus returns to its ground state via gamma emission:

$$^AX(d,p)^{A+1}X^* \Rightarrow {}^{A+1}X + \gamma \tag{3.2}$$

$$^AX(d,n)^{A+1}Y^* \Rightarrow {}^{A+1}Y + \gamma \tag{3.3}$$

The gamma energy is equal to the isotopically unique nuclear energy level spacing, providing unequivocal isotopic identification that forms the basis of PIGE. Spatial and temporal monitoring of gamma emitting isotopes can provide quantification of erosion/redeposition of low-Z isotopes, such as the boron or lithium layers used to alter PMI and improve plasma performance, and monitoring of the PFC wall condition, such as assaying oxygen concentration after a vacuum break. While the gamma energy distribution is relatively simple and well known, the angular distribution of gamma rays is more complicated. In general, the emitted distributions in angle are described

44

(a) Gamma Production cross Sections

(b) Neutron production cross section
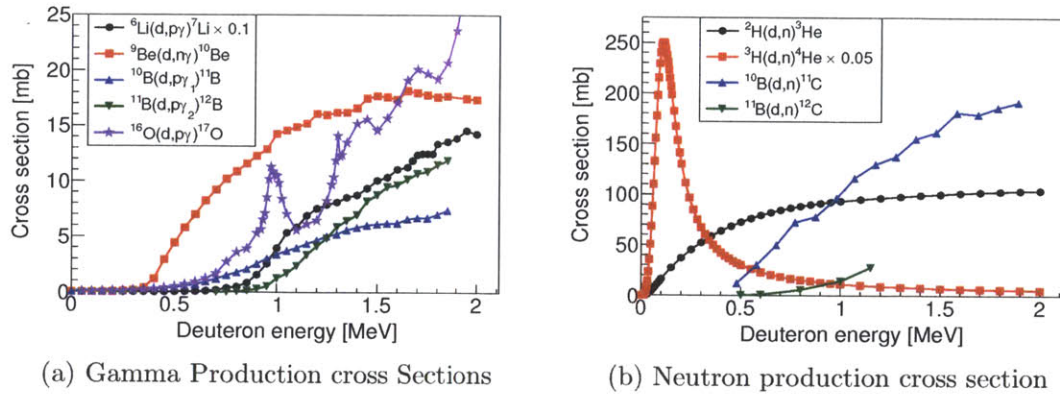
Figure 3-2: Some of the known deuteron-induced (a) gamma and (b) neutron production cross sections of interest for AIMS. For reference, the optimal beam energy for AIMS is $\lesssim 1.8$ MeV. Note that the very high cross section for the ^{3}H(d, n)^{4}He reaction is particularly favorable for tritium retention diagnosis with the AIMS technique. The gamma production cross sections are from [47]; the neutron production cross sections are from [48, 49, 50]

in nuclear theory by an expansion of Legendre polynomials, where the polynomial coefficients are a function of energy and angular momentum of the particles and nuclear level states involved in the reaction [45].

The availability of nuclear data for the gamma-production reactions of interest in Table 3.2 is essential for AIMS, which has variable reaction geometry and requires angle-resolved cross section data to computationally model the measurement process. Unfortunately, the gamma production cross section databases are relatively incomplete. While deuteron-induced absolute thick-target gamma yields for many materials have been compiled [41, 46], angular differential cross section data for incident deuterons below the ~2 MeV used in IBA have only been measured on some of the isotopes of interest and only at a single angle [47]; that data is shown in Figure 3-2a. Fortunately, a renewed interest in standard IBA with deuterons has led to a recent International Atomic Energy Agency (IAEA) initiative to experimentally measure and compile angular differential gamma production cross sections for most of the isotopes below calcium [42]. Coupled with cross section measurements now underway at MIT, a comprehensive data base is rapidly being developed that will be sufficient for AIMS measurements.

3.3.2 Neutron production reactions

In the second type, the deuteron is either stripped of its proton (stripping reactions) or fuses with the target nucleus (fusion reactions), ejecting a neutron and leaving the residual nucleus in the ground state. In AIMS, the principle neutron production

reactions of interest are the well known fusion reactions:

$$^2\text{H}(\text{d}, \text{n})^3\text{He} \tag{3.4}$$

$$^3\text{H}(\text{d}, \text{n})^4\text{He} \tag{3.5}$$

that can be used to directly quantify the deuterium and tritium retained in PFC surfaces. While these neutron-production reactions provide a direct measurement of deuterium and tritium in the absence of suitable gamma production reactions, IBA techniques based on neutron spectroscopy (PINE) are typically avoided due to the complexity of analysis and neutron radiation hazards in favor of techniques based on gamma spectroscopy (PIGE) [41]. In AIMS, PIGE is the preferred technique when gamma-production cross sections are available for the isotopes of interest; however, PINE is useful for corroborating PIGE measurements when gamma- and neutron-production cross sections are available. For example, boron - an element widely used to coat PFC surfaces for plasma performance reasons - can be analyzed with PIGE and PINE using the cross sections shown in Figure 3-2.

Unlike the gammas produced in nuclear reactions, the neutrons produced in the reactions given in Eqs. 3.4 and 3.5 do not have a single characteristic kinetic energy. The ejectile neutron kinetic energy is a function of the reaction type, the incident deuteron kinetic energy at the time of reaction, and the angle between the deuteron and neutron trajectories. At a particular measurement location in AIMS, the angle is fixed; therefore, the neutron kinetic energy can be used to identify deuterium or tritium as well as to potentially provide rough depth-resolution for the measurement.

For reactions of the form X(d,n)Y, the kinetic energy of the ejectile neutron (E_n) is given by

$$E_n(E_d, \theta) = E_T B \left(\cos\theta \left[\frac{D}{B} - \sin^2\theta \right]^{1/2} \right)^2 \tag{3.6}$$

where

$$B = \frac{m_d m_n \left(E_d / E_T \right)}{\left(m_d + m_n \right) \left(m_X + m_Y \right)} \tag{3.7}$$

$$D = \frac{m_X m_n}{\left(m_d + m_n \right) \left(m_X + m_Y \right)} \left[1 + \frac{m_d Q}{m_X E_T} \right] \tag{3.8}$$

where E_d is the deuteron energy entering the reaction channel, Q is the energy gain of the reaction, E_T is the sum of E_d and Q, and θ is the angle between the incident deuteron and ejectile neutron trajectories [41]. In AIMS, the angle between the deuteron beam and the neutron detector is fixed by the magnetic beam steering and detector location, leaving the neutron kinetic energy as a unique function of reaction type and deuteron depth. The dependence on depth derives from the deuteron slowing down in the PFC, which changes the ejectile neutron kinetic energy. Thus, it may be possible to eventually unfold these dependencies to produce a depth-resolved fuel retention measurement.

46

In contrast to gamma production reactions, both the cross section and the angular distributions of neutrons from the deuterium-deuterium and deuterium-tritium reactions are relatively well known due to the relative simplicity of the nuclear physics and the widespread use of these reactions in nuclear fusion research, nuclear weapons, and neutron generators. While the first reported measurements were made in 1936 [51], comprehensive angular distributions for both reactions are contained in the most recent ENDF/B-VII.1 data base, the world standard for nuclear cross section data [49]. The neutron production cross sections for deuterium-deuterium, deuterium-tritium, and deuterium-boron are shown in Figure 3-2b.

3.4 Measurement capabilities and material effects

In this section, the AIMS technique is assessed in terms of its sensitivity to the PMI-driven effects in materials, its modes of operation for measurement, and its potentially deleterious effects on the PFC surfaces. All calculations are performed assuming a 2 mA peak current 1 MeV deuteron RFQ operating with a 10 % duty factor at 100 Hz, such capabilities are well within the capabilities of modern RFQ accelerators [43]. Under these assumptions, approximately 10^{16} deuterons (1 mC) can be deposited onto the PFC surface in a five second measurement period, resulting in the capability to make many measurements in the tens-of-minute dwell time in between plasma shots on present fusion devices.

3.4.1 Measurement sensitivity

An estimation of the measurement sensitivity for the PFC surface diagnostic techniques in AIMS can be calculated from the particle production rates and the detector count rates. The AIMS techniques are shown to be highly appropriate for diagnosing PMI issues of interest such as fuel retention, erosion/redeposition, and material mixing.

Fuel retention

For assessing the retention of deuterium in PFC surfaces, the neutron production rate per micron can be estimated as

$$\frac{\text{neutrons}}{\mu m} = \sigma \cdot C_{^2H} \cdot n_a \cdot q_{^2H+} \tag{3.9}$$

$$= (10^{-29}\text{m}^2)(0.01)(10^{23}\text{m}^{-2})(10^{16}) \approx 10^8 \tag{3.10}$$

where σ is the cross section for the $^2\text{H}(\text{d,n})^3\text{He}$ reaction, $C_{^2H}$ is the concentration of retained deuterium fuel in the PFC surface, n_a is the areal density of the PFC,

and q_{2H+} is the total charge of incident deuteron ions from the RFQ deposited during the measurement. Equation 3.10 has been evaluated for assuming a 1% deuterium concentration in the high-Z metal PFC surface, which is approximately the expected saturation fluence for deuterium implantation from the boundary plasma[52]. The absolute detection efficiency, ϵ, of the liquid organic scintillation detectors that are presently proposed for neutron detection in AIMS is:

$$\epsilon = \frac{N_H \sigma_H}{N_H \sigma_H + N_C \sigma_C} \{1 - \exp\left[-\left(N_H \sigma_H + N_C \sigma_C\right)D\right]\} \qquad (3.11)$$

where N is the number density, σ_x is the elastic scattering cross section for neutrons on isotope x, and D is the neutron path length in the scintillator [53]. For 2.5 MeV neutrons (approximately the center-of-mass energy of neutrons from the deuterium-deuterium fusion reaction) incident on a 5 cm wide liquid organic scintillator EJ301-based detector, the efficiency is approximately 0.4 using the following values: $N_H = 4.82 \times 10^{28}$ m^{-3}; $N_C = 3.98 \times 10^{28}$ m^{-3}; $\sigma_H(2.5\ MeV) = 2.55 \times 10^{28}$m^2; $\sigma_C(2.5\ MeV) = 1.59 \times 10^{28}$m^2.

Finally, the calculated neutron count rate per micron of PFC is

$$\frac{N_n}{\mu m} = \frac{\text{neutrons}}{\mu m} \cdot \epsilon \cdot \frac{d\Omega}{4\pi} \qquad (3.12)$$

$$= (10^8)(0.4)(10^{-4}) \approx 10^4 \qquad (3.13)$$

which gives a $N_n^{-1/2} \sim 1\%$ counting accuracy per micron for 1% deuterium concentration at the PFC, which is very appropriate for diagnosis deuterium fuel retention in PFC surfaces. The calculation for tritium is more favorable with the much large cross section being only slightly offset by the decreased detection efficiency for higher energy neutrons.

Material erosion, migration, and mixing

The assessment of these PMI issues is primarily carried out through spectroscopy of gammas from the deuteron reaction with the low-Z isotopes in Table 3.2. The calculation of sensitivity is very similar to that done for fuel retention in the previous section.

Thick target gamma yields for 1 MeV deuterons are on the order of 10^6 $\gamma/\mu C/sr$ for ~MeV deuterons on low-Z isotopes [46] giving total gamma production rates on the order of 10^8 for the RFQ and measurement parameters described above. Assuming a gamma detector efficiency and solid angle of 10% and 10^{-3} steradian, respectively, the result is again a roughly 1% accuracy for the high-precision measurement of low-Z isotopes in the first ten microns of low-Z PFC surfaces. Such sensitivities are appropriate for providing depth resolution on the order of tens to hundreds of nanometers for the erosion or redeposition of material.

48

3.4.2 Modes of operation

Two modes of operation can be envisioned for AIMS. The first is a "dynamic measuring" mode, in which comprehensive PFC surface composition measurements would provide, for the first time, the ability to link discrete plasma conditions with the PFC surface. Such a capability is achieved during the course of an experimental run day when measurements can be made *in-situ* on a plasma shot-to-shot timescale without interrupting the standard operating procedures of the tokamak. The advantage is that measurements of the PFC surface can be acquired for any type of experimental run day, enabling time- and spatially-resolved diagnosis of large areas of the PFC surface in response to the full range of conditions encountered during normal plasma operations. In this case, the amount of time available between shots - typically set by time required to prepare the tokamak for the subsequent shot - limits the total PFC surface area that can be surveyed with acceptable measurement

The second mode is "operational monitoring", in which long-acquisition time measurements would be made outside of the plasma run day to fully characterize the state of all AIMS-accessible PFC surfaces. The data can contribute to facility optimization, for example, in the assessment of the PFC oxygen content after a vacuum break, in the evaluation of high-temperature baking, or in the monitoring of wall conditioning techniques such as lithization or boronization. Another critical application is in nuclear safety for deuterium-tritium burning tokamaks, where AIMS would provide localized tritium quantification over all accessible PFC surfaces and be able to provide a comprehensive assessment of detritiation experiments.

3.4.3 Measurement impacts on the PFC surfaces

A major concern for AIMS is whether or not the measurement technique perturbs the PMI conditions in the PFC surface or damages the PFC surface itself. Using the RFQ parameters described above, the following sections show that surface heating and modification are, at worst, mitigable with relatively simple techniques, and at best, not a concern. The nondestructivness of PFC surfaces and, therefore, intrinsic reproducibility of AIMS measurements is one of its key strengths compared to techniques such as LIBS or LIDS, which, as described in Chapter 2, must destroy the PFC surface in order to assay it.

Material heating

One concern is that the power load delivered to the PFC surface leads to sufficient heating to modify the PMI conditions or thermomechanical properties of the material. For the RFQ parameters described above, a 2 mA, 1 MeV deuteron beam at a 10% duty factor leads to a time-averaged power deposition, Q, of approximately ~ 1 MW m^{-2} assuming a beam spot size of approximately 1 cm^2 on the PFC surface.

Instantaneous power deposition occurs on a time scale, τ of $\sim 10^{-3}$ s, which is set the 10% duty cycle and 100 Hz frequency. The approximate surface temperature rise, ΔT, can be calculated using the approximate semi-infinite heat conduction equation

$$\Delta T \approx 2 \left(\frac{\tau}{\pi \kappa c_\rho} \right)^{1/2} Q \tag{3.14}$$

where κ (thermal conductivity) is ~ 100 W m^{-1} K^{-1} and c_ρ (volumetric heat capacity) is $\sim 2 \times 10^6$ J m^{-3} K^{-1} for PFC materials, and Q is the time-averaged power deposition. Thus, the beam energy deposition could lead to substantial nonlinear temperature increases on the PFC surfaces during extended measurements.

To alleviate this issue, the deuteron beam can be toroidally rastered, or sinusoidally swept, continually during measurements when high beam power is used. The effect is to distribute the beam over a larger wetted area of PFC surface in order to alleviate excess localized heating. This can be accomplished with a slight ripple current on the vertical magnetic field coils used to raster the beam toroidally, preventing significant temperature increases on the PFC surfaces. Of course, the heating issue will be moot for AIMS on magnetic fusion devices with actively cooled PFCs.

Surface perturbations

Another concern for AIMS is that the deuteron beam will substantially impact the PFC surface, either by altering the deuterium concentration with implanted beam deuterons or by damaging the material lattice through deuteron-induced atomic displacements and vacancies. In general, IBA, either AIMS or *ex-situ*, can be considered nonperturbative since the range of the beam ions in materials is on the order of microns - much larger than the surface depth of interest - and since the fluence of beam ions is typically orders of magnitude less than the incident plasma ion fluences. The damage to the material atomic structure from beam deuteron collisions can be addressed using SRIM to simulate the effects of 1 MeV deuterons into a PFC material. SRIM is one of the leading codes for modeling the the atomic effects of energetic ions interacting with materials [54].

The distributions of implanted deuterons and atomic displacements due to a 1 MeV deuteron beam incident on a molybdenum PFC are shown in Figure 3-3. Because of ion stopping physics, in which a massive nucleus primarily interacts electrically with relatively small mass atomic electrons, essentially all of the deuterons thermalize and stop at the same distance, or "range", into the material. Compared to plasma deuterium ions, which saturate only the first monolayers of the PFC surface ($\lesssim 20$ nm), the unreacted beam deuterons accumulate entirely at 5 μm into the material, leading to almost zero perturbation of the retained plasma deuterium fuel near the surface that is of interest for AIMS measurements. The accumulation of beam deuterium is essentially negligible compared to the plasma deuterium. As mentioned above, the beam deuteron fluence ($lesssim10^{19}$ D m^{-2} is orders of magnitude smaller than the

50

(a) Deuteron implantation distribution

(b) Atomic displacement distribution
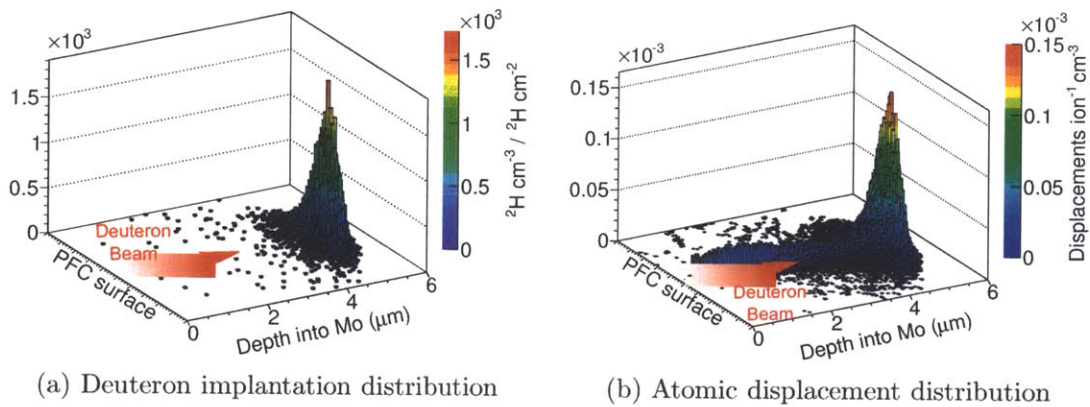
Figure 3-3: The effects of a 1 MeV deuteron beam entering a molybdenum PFC surface. The key result is that the implanted deuterium and the atomic displacements caused by the incident deuteron beam are localized approximately 5 μm away from the surface, ensuring that AIMS is nonperturbative and nondestructive with respect to the PMI processes that occur in the first 20 nm of PFC surface.

plasma deuteron fluence ($\gtrsim 10^{21}$ D m^{-2}) that leads to fuel retention.

Similarly, the atomic displacements caused by the incident beam deuterons are strongly localized near the end of the range, where the decreasing deuteron kinetic energy leads to ion-nucleus collisions dominating over the coulombic repulsion of electrons. The ion-nucleus collisions lead to damage cascades in the PFC material, causing displacements and vacancies in the material lattice. While radiation-induced material damage plays a role in fuel retention through trapping in damage defects, the deuteron beam-induced damage is sufficiently far from the surface to effect PMI dynamics or PFC surface properties.

Chapter 4

The AIMS diagnostic on the Alcator C-Mod tokamak

The essential theory of Accelerator-based In-Situ Material Surveillance (AIMS) was presented in detail in Chapter 3 without regard for the hardware components, data analysis, and engineering solutions required to realize a working experimental diagnostic from the theoretical principles. An implementation of an AIMS diagnostic, which comprises an RFQ accelerator, high voltage and RF hardware, neutron and gamma detectors, data acquisition system, and data analysis software, is a nontrivial, multicomponent subsystem that must be seamlessly interfaced to the complex system of the magnetic fusion device.

The purpose of this chapter is to present a detailed description of the AIMS diagnostic on Alcator C-Mod[1], the first AIMS diagnostic installed on a magnetic fusion device. Each component is described individually so as to impart an understanding of how the discrete components link together to form a single diagnostic system. It is noted that the RFQ accelerator, beam focusing optics, and beam diagnostics form a significant portion of another Ph.D. dissertation and will, therefore, only be described briefly here; the interested reader is referred to [55].

4.1 Overview

AGNOSTIC was successfully installed on the Alcator C-Mod tokamak [56] at the MIT Plasma Science and Fusion Center in August 2012. Depicted in Figure 4-1, the diagnostic consists of an RFQ coupled to the Alcator C-Mod vacuum vessel through a radial diagnostic port. In order to ensure a well-diagnosed, focused deuteron beam spot on the order of $\lesssim 2$ cm^2, the RFQ beamline contains beam focusing optics and

---

[1]Colloquially known as AGNOSTIC (Accelerator-based Gamma and Neutron Observing Surface Tool for In-situ Components)
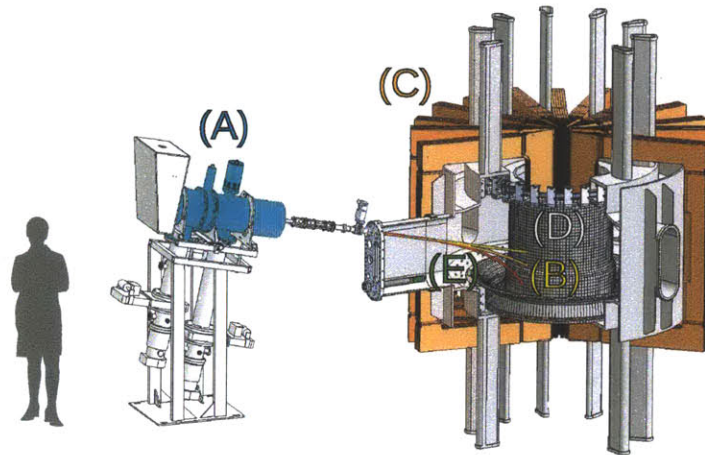
Figure 4-1: The AIMS diagnostic installed on the Alcator C-Mod tokamak showing (A) the RFQ accelerator, (B) three different deuteron beam trajectories, (C) the toroidal field magnets used for beam steering, (D) the PFC tiles, and (E) the reentrant neutron and gamma detectors.

current monitoring instrumentation. A gate valve near the radial diagnostic port flange provides the ability to isolate the RFQ and tokamak vacuum system. This is necessary to protect the RFQ vacuum system during tokamak operations (plasma shots, wall conditioning techniques) and to ensure that the RFQ is accessible for standalone operation and maintenance during plasma campaigns.

To maximize the detector solid angles with respect to the PFC surface measurement locations, compact scintillator-based neutron and gamma detectors are placed inside a vacuum reentrant tube on the radial diagnostic port flange. The stainless steel tube (50 cm long, 0.16 cm thick) is welded to the radial diagnostic port flange and enables detector operation in atmosphere. The reentrant tube location was chosen since detector installation in the tokamak vacuum vessel was considered too restrictive, requiring specialized detectors and limiting intra-plasma campaign detector access. Furthermore, the reentrant tube thermally shields the detectors during plasma shots, mitigates mechanical shock during plasma disruptions, and provides easy access to the detectors for maintenance and calibration during the plasma campaign.

The primary engineering challenges associated with implementing AIMS were geometric constraints on the installation position of the RFQ, beam transport system, and particle detectors in the crowded tokamak cell. High-fidelity CAD models of the Alcator C-Mod tokamak, superstructure, and major diagnostic equipment were used to determine feasible installation positions for each component of AGNOSTIC. Within the determined parameter space, a detailed optimization was performed using the RFQ deuteron beam dynamics and AIMS synthetic diagnostic simulations that are described in Chapter 5. The result is the configuration shown in Figure 4-1.

54
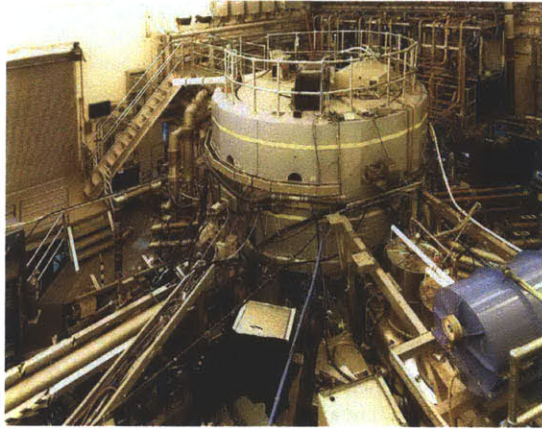
(a) The Alcator C-Mod experimental hall
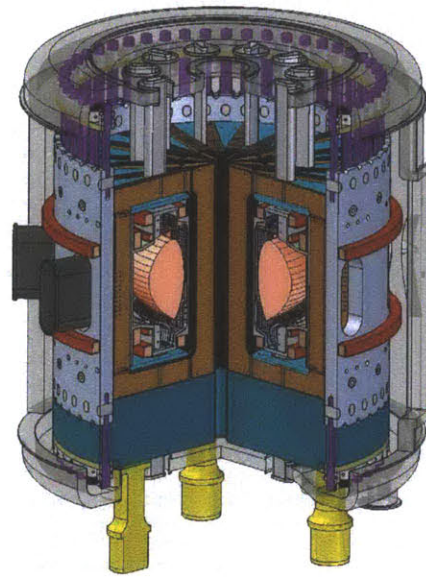
(b) Solid model of Alcator C-Mod

Figure 4-2: A photograph of the Alcator C-Mod tokamak in the experiment hall at MIT's Plasma Science and Fusion Center is shown in Figure 4-2a. A cutaway view on an engineering solid model of the Alcator C-Mod tokamak shows the major components of the compact toroidal device in Figure 4-2b

4.2 The Alcator C-Mod tokamak

The Alcator C-Mod tokamak is a toroidal magnetic confinement fusion experiment located at the MIT Plasma Science in Fusion Center [56]. It is the third in the "Alcator" family of tokamaks, being preceded by Alcator A (1973-1979) and Alcator C (1978-1987), and follows its predecessors compact volume, high-magnetic field approach to plasma confinement. The 20 toroidal field coils are normal conducting copper, capable of producing a maximum magnetic field of 8.0 T on-axis the magnetic field and 17.3 T on the inner leg of the toroidal field coils. 5 sets of poloidal copper field coils (top and bottom) are used for plasma shaping and control. With a major and minor radius of 0.67 m and 0.22 m, respectively, Alcator C-Mod is capable of sustaining ~ 1 m^3 of confined plasma for approximately 2 seconds at densities of $1 - 5 \times 10^{20}$ m^{20}

Alcator C-Mod is probably the most ideal environment of any existing magnetic fusion device to study PMI science. It is the only active tokamak with all refractory metal PFCs (molybdenum), high average power flux into SOL (~ 1 MW m^{-2}), and heat fluxes to the PFC surfaces ($\lesssim 10$ MW^{-2}), more closely replicating the expected conditions in a magnetic fusion reactor than other active tokamaks. Its novel vertical target lower divertor was adopted as the standard configuration in most tokamaks, most notably in the JET ITER-like Wall project in order to experimentally validate

55

Table 4.1: Key plasma and material parameter of the Alcator C-Mod tokamak as of 2013

Parameter	Symbol	Value
Major radius	R	0.67 m
Minor radius	A	0.22 m
Aspect ratio^{-1}	ϵ	0.33
Toroidal field	B_ϕ	8 T
Plasma current	I_p	2 MA
Elongation	κ	1.7
Triangularity	δ	0.6
Plasma volume	V_p	1.0 m^3
Pulse length	t	2 s
ICRH Power	-	6 MW
LHCD Power	-	1 MW
SOL power flux	P/S	1 MW m-2
Material heat flux	Q	10 MW m-2
Wall material	-	Molybdenum
Plasma topology	-	Limited/Diverted
Plasma fuel	-	^{2}H, ^{3}He

the ITER vertical target divertor [57]. The divertor and power SOL power flux thus gives Alcator C-Mod a highly similar edge, SOL, and divertor for reactor-relevant PMI studies [58]. A complementary suite of advanced boundary plasma and material diagnostics, such as gas puff imaging, SOL probes, material thermocouples, IR surface imaging, and the Surface Science Station strongly complement the capability of AIMS [59] for investigating PMI experimentally in a tokamak.

4.3 The RFQ accelerator

Shown in Figure 4-3, the MIT RFQ is a refurbished prototype 0.9 MeV deuterium ion accelerator from ACCSYS Technology Inc. The accelerator cavity measures 1.02 m in length with 0.72 m quadrupole vanes and is powered by a 425 MHz 60kW RF system. Significant upgrades to the controls, instrumentation, mechanical support structure, and vacuum system were required for integration into the tokamak environment. The accelerator controls and instrumentation were upgraded to digital Group 3 fiber optic loop controllers for remote operation in the high radiation environment of the tokamak cell. In addition, the mechanical support structure and vacuum system were redesigned to fit in the confined space surrounding the tokamak port while allowing for precision alignment of the RFQ cavity to the port flange.

The RFQ must be precisely aligned in order to ensure high fidelity with the beam modeling codes used to optimize the beam focusing and magnetic steering. Before coupling to the Alcator C-Mod vacuum system for the first time, the RFQ was aligned using a laser mounted in the accelerator ion source to ensure that the axis of the
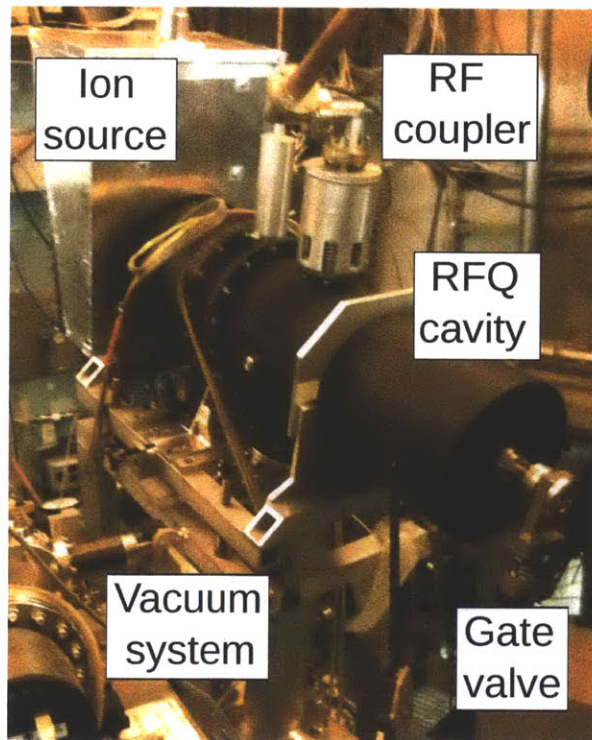
Figure 4-3: The RFQ accelerator and support structure in the Alcator C-Mod cell. The RF coax cable enters at the top of the cylindrical RF cavity. The plasma ion source is contained near the rear box while the vacuum system is underneath. The RFQ was gated off and detached from the tokamak for diagnostic tests at this time.

acceleration cavity was co-linear with the axis of the injection flange. A precision alignment was critical because there was insufficient space for electrostatic beam alignment optics between the RFQ and the tokamak port flange that might normally be used in more flexible experimental geometries.

To achieve $\lesssim 2$ cm spatial resolution on the target PFCs - roughly the width of a molybdenum PFC tile in Alcator C-Mod - beam optics are necessary to maintain a focused beam over the ~ 2 m trajectory through the beamline and tokamak vacuum vessel. Because the iron-core magnetic quadrupoles typically used to focus ion beams can perturb the plasma magnetic fields or create unacceptable structural forces on the beamline, a set of three permanent magnet quadrupoles (PMQ) were used because of their compact size and zero net magnetic field.

To monitor the injected deuteron beam current, a wide-band ferrite current transformer from Pearson Electronics with amplification and noise suppression was installed on the beamline. The transformer was located at the point in the beamline immediately before injection to accurately measure the deuteron current entering the vacuum vessel.

4.4 Detector data acquisition system

The detector data acquisition system (DAQ) was constructed to utilize the most recent advances in waveform digitization, digital pulse processing, and persistent storage of all detector pulses. With the raw waveforms from each measurement stored on hard disk, offline digital analysis can be performed repeatedly with different pulse processing algorithms in order to extract the maximum amount of information from the data set. Such a system also minimizes the number of errors that occur in data acquisition since traditionally analog data acquisition functions (e.g. baseline restoration, pileup rejection, pulse shape discrimination) are performed in flexible digital algorithms rather than immutable hardware settings.

4.4.1 Physical hardware and analysis

The DAQ is used to digitize and persistently store the waveforms from all the detectors used in the experiment as well as signals of interest from the RFQ such as the beam current. The core of the DAQ is composed of VME acquisition hardware provided by CAEN S.p.A:

- V1720 digitizer (8 channel, 250 MSamples/second, 12-bit)

- V6534 high voltage supply (6 channel)

- V1718 VME-USB interface

|(a) Digital waveform|(b) Digital pulse area spectrum|
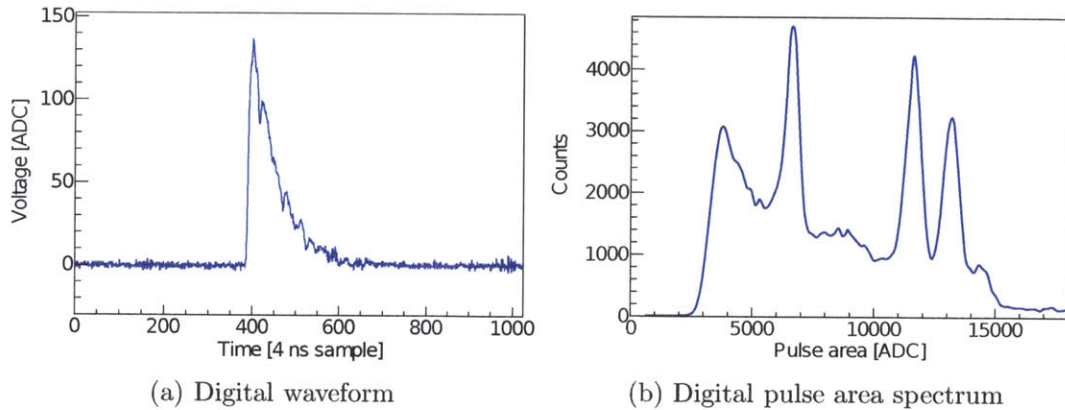
Figure 4-4: A representative example of a digital detector waveform acquired with the DAQ is shown in Figure 4-4a; the time is given in digitizer sample number, with one sample representing 4 ns of linear time. Histogramming either the waveform pulse height or the waveform area will result in a digital pulse spectra, which is represented in analog-to-digital (ADC) units. Figure 4-4b shows a pulse area spectrum.

- VME8004B powered enclosure

The digitizer was selected as the appropriate combination of digitization rate and bit depth for the detectors and analysis techniques used in AIMS while the high voltage supply provides sufficient power and can be remotely controlled.

A rack-mounted PC server controls the DAQ through custom software based on the ROOT toolkit [60] and connects to the VME boards via the V1718 VME-USB board interface. A separate ROOT-based analysis tool handles all the functions of a modern digital pulse processing system. These include parallelized waveform processing (pile-up deconvolution, pulse shape discrimination, spectroscopy), spectrum processing (energy calibration, peak finding, peak integration, background subtraction), and publication-ready graphical output. The acquisition and analysis tools are described in detail in Appendix A.

4.4.2 Pulse processing

Analog waveforms are input into the 12-bit 250 MSamples/second digitizer, where they are assigned a discrete digital value between 0 and $2^{12} = 4095$ corresponding to the analog 0-2 V dynamic input range; sampling of the analog waveform occurs every 4 ns. Digital waveforms can then be represented as sample number (in sample units) versus voltage (in Analog-to-Digital or ADC units) as shown in Figure 4-4a When many digital waveforms are acquired, they may be processed into spectra, either by calculating the pulse height or the pulse area for many waveforms and histogramming the results. An example of a digital pulse area spectrum is shown in Figure 4-4b,

Figure 4-5: An image of the EJ301-PMT detector next to a U.S. quarter for scale. The slightly bulging cylinder at the left contains the EJ301 liquid scintillator in an aluminum canister; the majority of the detector is the 1 inch diameter PMT.

which is computed by histogramming the integrated area between the baseline and the waveform for many waveforms. Because waveform voltage is given in ADC units, the units of the pulse spectra will also be in ADC units until a calibration method is applied to convert the X-axis units into the appropriate energy unit.

4.5   Fast neutron detection

The neutron detector is composed of a $2.5\phi \times 2.7$ cm volume of EJ301 liquid organic scintillator within a 1.6 mm thick canister of aluminum. A 6 mm Borofloat window transmits scintillation photons to an optically coupled Hamamatsu R6095 1-inch photomultiplier tube (PMT) with bialkali photocathode for readout. The detector was assembled in-house and is shown in Figure 4-5. As discussed in Chapter 3, an important attribute of scintillation detectors in AIMS is their ability to operate in the magnetic fields required for deuteron beam steering. PMTs, which use electrostatic fields to induce avalanches of electrons from accelerated photoelectrons from the photocathode, experience severely reduced gain or outright inoperability due to the interference of magnetic fields. Thus, the EJ301-PMT detector had to be located near the entrance of the reentrant tube (where the magnetic field magnitude is near zero) shown in Figure 4-1 to ensure successful operation. Because no other suitable neutron spectrometers for AIMS have been identified in the scientific or commercial literature, the development of a new type of neutron detectors, based on the coupling of EJ301 to a SiPM readout with a novel current preamplifier, has been undertaken. The developments are preliminary and outside the scope of this thesis but will be described in a future publication.

4.5.1   Scintillation properties

EJ301[2] is one of the most widely used organic scintillators for fast neutron and gamma detection. The key scintillator properties of EJ301 are shown in Table 4.2. The properties of EJ301 have been extensively reported in industrial and scientific literature,

---

[2]This xylene- and naphthalene-based organic liquid is known variably by its manufacturer's product code: EJ301 (Eljen Technology), BC501A (Saint-Gobain), or NE213 (Nuclear Enterprises)

Quantity	Value
Mass Density [g/cm^3]	0.874
Atomic C:H ratio	1.212
Refractive Index	1.505
Light / MeV [photons]	~12 000
Peak emission wavelength [nm]	425
Light decay components [ns]	3.0, 32, 270

Table 4.2: The key properties of EJ301 liquid organic scintillator [61].

(a) EJ301 scintillation response functions

(b) EJ301 scintillation emission spectrum and PMT photocathode quantum efficiency
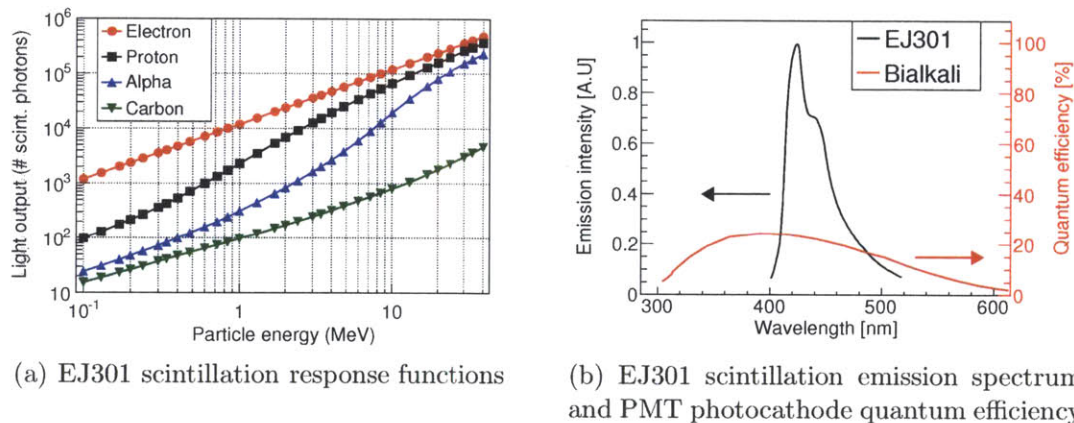
Figure 4-6: The principal optical properties of the EJ301-PMT detector. Figure 4-6a shows the scintillation light produced in EJ301 as a function of the energy deposited by different charged particles [67]; the scintillation response is essentially linear for electrons but highly nonlinear for charged ions. Figure 4-6b shows the relatively well matched EJ301 scintillation photon emission spectrum and the quantum efficiency curve for the a bialkali photocathode in the PMT.

such as material properties [61], optical properties [62, 63, 64], interaction mechanisms with fast neutrons and gammas [53], and performance as a detector for neutrons and gammas [53, 65, 66].

The scintillator response of EJ301 describes the number of scintillation photons or "light" produced as a function of the energy deposited in the scintillator and the type of ionizing particle. As one of the most widely studied organic scintillators, there are a number of EJ301 response functions published in the literature [67, 68, 69, 70, 71].

The EJ301 scintillation response to electrons is linear above approximately 0.1 MeV deposited energy, with slight nonlinearities below this energy [72]. As discussed below, all light output - regardless of the particle depositing energy in the scintillator - is normalized to the energy of electrons that would produce the equivalent light output; the unit used is MeV-electron-equivalent or "MeVee". For ions, perhaps the most cited EJ301 scintillator response is that of Verbinski et. al, which is shown in Figure 4-6a [67]. Strong nonlinearities, as well as clear differences in light yield between different

ion species, dominate the scintillation response.

Regardless of energy deposited and particle type, the scintillation photon emission spectrum is relatively narrow in the blue portion of the visible spectrum, with a maximum emission probability around 425 nm in wavelength. Traditionally, PMTs using bialkali photocathodes are used for light readout due to good matching between the EJ301 emission spectrum and wavelength-dependent quantum efficiency curve of bialkali. Both spectral functions are shown in Figure 4-6b.

4.5.2 Spectroscopy

From the perspective of neutron and gamma spectroscopy, the most important aspect of EJ301 is its exclusive composition of hydrogen and carbon. For gammas, the low average atomic number of EJ301 causes Compton scattering to dominate the interactions, eliminating the presence of a photopeak in the detector response function. The gamma response is instead composed of the broad Compton continuum derived from scattering kinematics, with the Compton edge located at the maximum energy that can be transferred to an atomic electron in a forward collision:

$$E_{e^-} = \frac{E_\gamma^2}{\frac{1}{2}m_e c^2 + E_\gamma} \quad (4.1)$$

where E_{e^-} is the recoil electron energy, E_γ is the incident gamma energy, and $m_e c^2$ is the electron rest mass energy. For scintillators whose size exceeds the gamma mean free path, multiple scattering will contribute a small number of events above the Compton edge.

For fast neutron interactions, the situation is more complicated with both elastic and inelastic collisions leading to the production of scintillation light. The dominant neutron interaction mechanism in EJ301 is elastic scattering off hydrogen and carbon nuclei. Because hydrogen nuclei generate significantly more scintillation light than recoil carbon nuclei for identical deposited energy (See Figure 4-6a), the detector response function is due primarily to the ^{1}H(n,n)^{1}H reaction. The result is a broad rectangular continuum - which is derived from the isotropic neutron-proton elastic scattering cross section - with the high energy edge located at the maximum energy that can be transferred in a forward elastic collision:

$$E_X = \frac{4 A_X A_n}{(A_X + A_n)^2} E_n \quad (4.2)$$

where E_X is the recoil nucleus, A_X is the atomic mass of the recoil nucleus, A_n is the mass of the incident neutron, and E_n is the kinetic energy of the incident neutron. For neutrons scattering off hydrogen nuclei, Equation 4.2 gives $E_{^1H} = E_n$. For neutrons scattering off carbon-12 nuclei, Equation 4.2 gives $E_{^{12}C} = 0.284 E_n$. Because recoil carbon ions produce negligible light compared to recoil hydrogen nuclei, the

Source: ^{137}Cs
E_γ = 0.662 MeV

— EJ301-PMT

Counts [A.U.]

1000

500

0

0   0.1   0.2   0.3   0.4   0.5   0.6

Energy [MeVee]
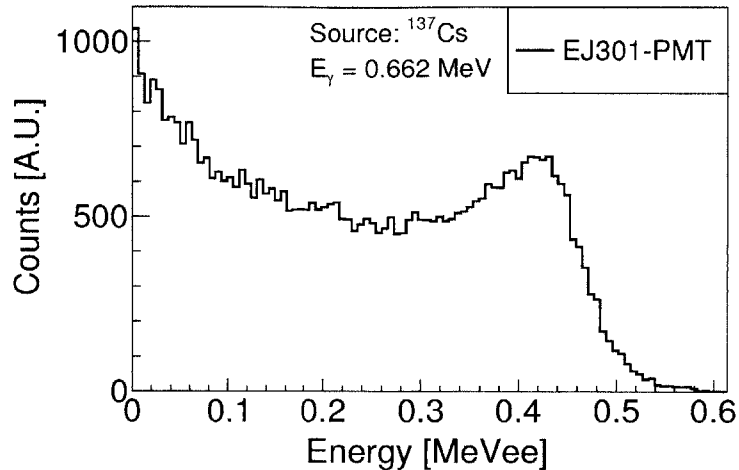
Figure 4-7: The experimental response of the EJ301-PMT detector to 0.662 MeV gammas from a cesium-137 check source. The responses were computed with the digital acquisition and pulse processing methods described in Section 4.4. The spectrum is dominated by Compton scattering and exhibits no photoabsorption peak.

^{12}C(n,n)^{12}C reaction is most evident primarily through multiple scattering. Incident neutrons lose kinetic energy by first scattering off carbon and then transferring the remainder of their kinetic energy to hydrogen nuclei in a secondary scatter. The result is a peaked hump slightly below the high energy edge superimposed on the rectangular continuum.

When the incident neutron energies are above approximately 6 MeV, inelastic nuclear reaction channels with the carbon isotopes begin to open up. These reactions include ^{12}C(n,α)^{9}Be ($E_{threshold}$ = 6.18 MeV), ^{12}C(n,p)^{12}B (13.65 MeV), and ^{12}C(n,d)^{11}B (14.89 MeV) as well as the more complex breakup reactions such as ^{12}C(n,n')^{12}C* $\Rightarrow$ 3α (7.89 MeV), in which the residual excited nucleus fragments into lighter nuclei. Because the reaction products are almost exclusively light ions and recoil nuclei, they contribute significantly to the low energy region of the detector response function.

An example of gamma spectroscopy with the EJ301-PMT detector is shown in Figure 4-7. Because particle interactions are dominated by scattering kinematics, EJ301-based detectors show roughly rectangular response functions for both monoenergetic neutrons and gammas that complicates deconvolution of the incident particle spectrum. The presence of a smeared edge in such spectra, such as the edge at 0.478 MeV in Figure 4-7, indicate the presence of monoenergetic particles incident upon the detector with the location of the half-height of the edge determining the kinetic energy of the monoenergetic particles. Such information can be used to discriminate between monoenergetic neutrons and gammas from the nuclear reactions described in Chapter 3.
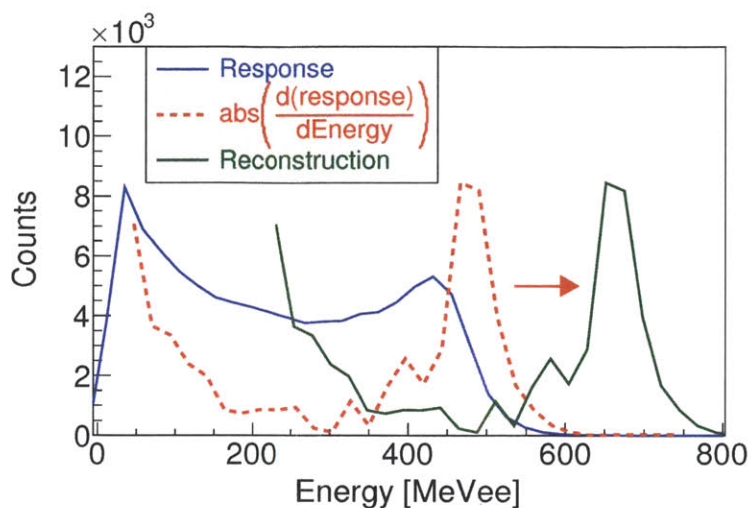
Figure 4-8: Using an experimentally acquired EJ301-PMT response to 0.662 MeV gammas (blue), a peak at the incident energy of the particles can be obtained by calculating the absolute value of the derivative of detector response. In the case of gammas, the kinematics of Compton scattering are used to calculate the required energy shift since some incident energy is carried away by the scattered gamma; for neutrons, no such correction is necessary.

Although no peaks appear in the EJ301-PMT spectra, the absolute value of the derivative of a rectangular response function from monoenergetic particles can be used to reconstruct a peak centered at the incident particle kinetic energy, albeit with poor resolution [53]. An example of this is shown in Figure 4-8 for the EJ301-PMT detector spectra of 0.662 MeV gammas. After taking the absolute value of the derivative of the EJ301-PMT spectra, the result is shifted in energy by an amount equal to the energy carried away by the scattered gamma in Compton scattering. It is evident that a peak with sufficient energy resolution can be achieved in order to determine the kinetic energy of the incident gammas. For neutrons scattering off hydrogen in the detector, the process is simpler since the maximum hydrogen recoil energy is equal to the incident neutron kinetic energy and no energy shift in the result is required to reconstruct the correctly centered peak.

4.5.3   Linearization and calibration

As previously mentioned, because of the multiple nonlinear scintillator response functions, it is desirable from a practical standpoint to place the response functions of the EJ301-based detectors on an absolute, linear scale that is independent of the ionizing particle or energy deposited. The linear response of electrons provides the convenient standard against which other particle's responses will be compared.

The scintillation light generated by an EJ301-based detector due to energy deposition - regardless of ionizing particle - is given in units of "MeV-electron-equivalent" or MeVee, which is the energy at which electrons would produce the same amount of scintillation light as the energy actually deposited by an ion. For example, using Verbinksi's scintillation response shown in Figure 4-6a, the $\sim 10^4$ scintillation photons produced by a 2.5 MeV proton fully stopping in EJ301 is equivalent to approximately 0.82 MeVee [67]. In the formal literature on spectroscopy with organic scintillators, X-axis value of the detector response function is typically referred to as "light" with the units in MeVee. In this thesis, for simplicity and the benefit of experts outside the field of organic scintillation detectors, the X-axis value will be referred to as the particle energy - neutron or gamma - that is deposited in the scintillator in order to emphasize what is being measured. Thus, the terms "detector response function" and "energy spectrum" may be used interchangeably. The unit keVee or MeVee, however, will continue to be used to accurately reflect the underlying detector physics.

To convert the EJ301-PMT pulses from the ADC units assigned by the DAQ to energy units, a calibration curve was constructed using the following procedure. Pulse area spectra were acquired with the DAQ for monoenergetic gammas from ^{22}Na ($E_\gamma = 0.511$, 1.274 MeV), ^{137}Cs ($E_\gamma = 0.662$ MeV), and ^{60}Co ($E_\gamma = 1.332$ MeV) check sources and the strong background from ^{40}K ($E_\gamma = 1.470$ MeV). The Compton edge locations - corresponding to the position of the half-height of the edge - is then found in the spectra (in units of ADC). The location value is multiplied by a small, energy-dependent correction factor required to account for a slight difference in the actual position versus the half-height position [73]. Finally, a plot of deposited energy (in energy units) versus Compton half-height positions (in ADC units) defines the calibration curve, which appears in Figure 4-9

4.5.4 Pulse shape discrimination (PSD)

While the EJ301-PMT configuration detects both gammas and neutrons, standard pulse processing techniques can be used to digitally discriminate between them using the particle-dependent decay tail times of the scintillation pulses. Regardless of the particle depositing energy, the principle decay times of EJ301 scintillation pulses are 3.2, 32, and 270 ns [61]; however, pulses from neutron-induced ion recoils will contain a much higher fraction of the total light in the slow components relative to pulses from gamma-induced electron recoils [53]. Two individual, experimental waveforms from the EJ301-PMT detector, one from a neutron-induced event and one from a gamma-induced event, are shown together in Figure 4-10; the difference in the scintillation light pulse decay tail, which forms the basis for PSD, is strongly evident.

One of the most effective digital PSD methods is to bin the integrals of the total pulse and of the tail pulse in a two-dimensional histogram, which will show separate neutron and gamma distributions [74]. To evaluate PSD capabilities of the EJ301-PMT detector, the detector was exposed to a ^{241}Americium-Beryllium (AmBe) source. The
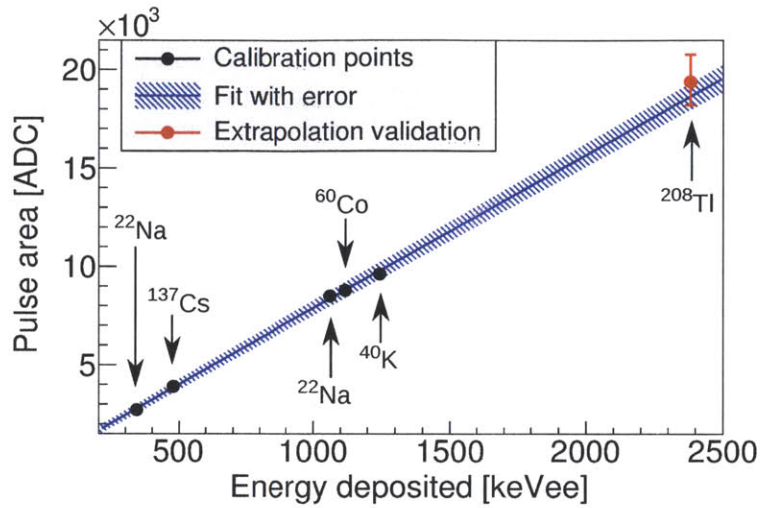
Figure 4-9: The experimental calibration curve for the EJ301-PMT detector. The curve is generated by fitting a first order polynomial to the 5 lower energy data points; the reduced χ^2 fit test value is 0.48, confirming a high degree of linearity in the range 0.341 - 1.243 MeVee. The data point from the weak ^{208}Tl environmental background signal, which was not used in the fit, confirms the extrapolated linearity up to 2.341 MeVee.
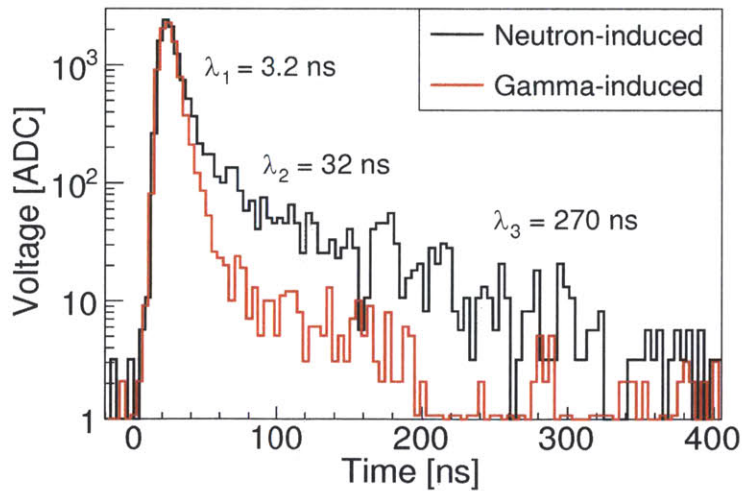
Figure 4-10: A comparison between a neutron-induced pulse and a proton-induced pulse from the EJ301-PMT detector. The higher fraction of light in the long decay components, or "tail", of neutron-induced events compared to gamma-induced events is the basis for pulse shape discrimination.
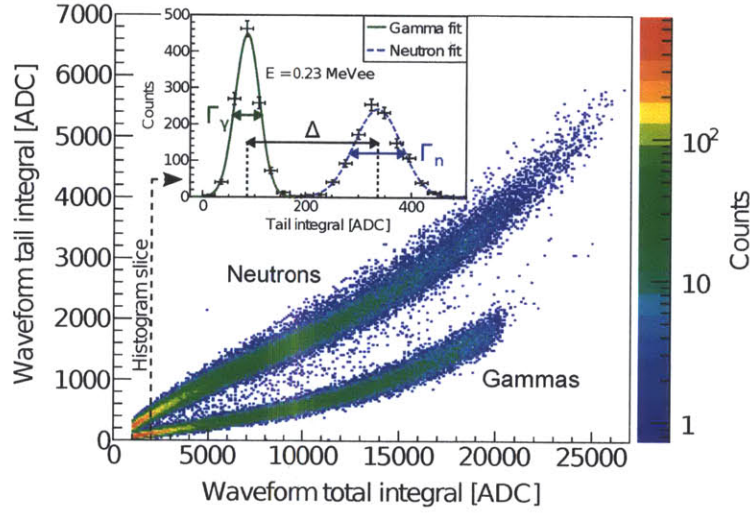
Figure 4-11: The results of digital PSD using the charge integration technique with the EJ301-PMT detector exposed to a ^{241}AmBe source. The neutron and gamma branches are well separated down to the lowest energies. The standard figure-of-merit measure of the effectiveness of PSD is shown in the inset, where the neutron and gamma distributions are well separated at 0.23 MeVee (total waveform integral of 2000 ADC); the figure of merit from Equation 4.4 is 1.57, demonstrating excellent quantitative particle discrimination.

unstable ^{241}Am nucleus spontaneously decays via the emission of an alpha particle, which generates neutrons and gammas via the nuclear reaction

$$^9\text{Be}(\alpha,\text{n})^{12}\text{C}^* \;\Rightarrow\; ^{12}\text{C} + \gamma(4.44 \text{ MeV}) \tag{4.3}$$

The result is a complex neutron emission spectrum between 2-10 MeV [75] and a significant flux of 4.44 MeV gammas. Additional gammas are generated through inelastic neutron reactions with the detector and ambient geometry.

The optimal integration range for the tail pulse was approximately 30 ns and 150 ns after the start of the pulse, where the charge differential between electron- and proton-induced pulses is strongly evident. The results of the PSD analysis are shown in Figure 4-11. Two distributions are clearly separated in the histogram over the entire energy range - represented by the total waveform integral. Because neutron-induced events have more light in the longer decay tail, the neutron distribution falls above the gamma distribution.

The effectiveness of the PSD can be quantified by defining the following figure of merit (F.O.M.) [76]:

$$\text{F.O.M.}(E_{dep}) = \left.\frac{\Delta}{\Gamma_n + \Gamma_\gamma}\right|_{E_{dep}} \tag{4.4}$$

67
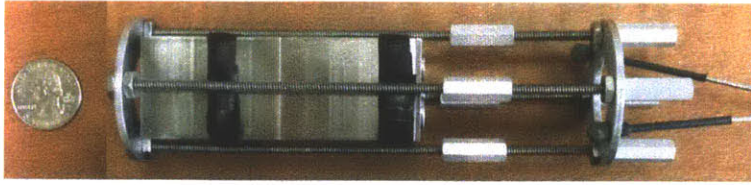
Figure 4-12: An image of the LaBr$_3$-SiAPD detector next to a standard U.S. quarter for scale. The detector is shown inside the cartridge that secures the detector inside the vacuum reentrant tube on Alcator C-Mod during AIMS measurements.

where E_{dep} is the total energy deposited in the detector, Γ_x is the full-width half-maximum of the Gaussian fits to the tail distributions of particle x, and Δ is the distance between the gaussian means. F.O.M $\gtrsim 1$ values indicate essentially zero overlap in the gaussian neutron-gamma distributions at the evaluated energy while F.O.M values < 1 indicate increasing overlap and, thus, a worsening ability to accurately distinguish neutrons and gammas. In the inset of Figure 4-11, the F.O.M. evaluation is shown for 0.23 MeVee (total integral of 2000 ADC), approximately the lowest energy deposition relevant in AIMS. The F.O.M. was calculated to be 1.57, demonstrating excellent PSD over the energy range of interest for AIMS. Careful evaluation has shown that PSD becomes unreliable, i.e. F.O.M. $\lesssim 1$, around 0.14 MeVee (total integral of 1000 ADC) with this particular detector configuration. Thus, for deposited particle energies above the F.O.M. minimum energy threshold, essentially gamma-free neutron spectra can be generated with PSD.

4.6 Gamma detection

The gamma detector was manufactured by Saint-Gobain Crystals and is based on the original design of Flamanc and Rosza [77]. It is composed of a 0.9×0.9×3.5 cm cerium-doped Lanthanum Bromide (LaBr$_3$) inorganic scintillator crystal optically coupled to a Hamamatsu S8664-1010 silicon avalanche photodiode (SiAPD) for readout. An internal charge-sensitive preamplifier aids in pulse shaping. All components are enclosed in a 2 mm thick stainless steel case measuring $3.0 \times 3.0 \times 8.5$ cm. The detector has been ruggedized against mechanical shock. In order to substantially increase the readout rate, a Cremat CR200 shaping amplifier with a 250 ns time constant circuit was used to transform the long preamplifier output exponential pulses to narrow gaussian pulses. The detector is shown in Figure 4-12.

4.6.1 Scintillation properties

Thallium-doped sodium-iodide has dominated the field of scintillator-based gamma spectroscopy since it was first introduced in 1948 [78], primarily due to its high

Quantity	Value
Mass Density [g/cm^3]	5.08
Refractive Index	1.9
Light / MeV [photons]	~63 000
Peak emission wavelength [nm]	382
Light decay component [ns]	16

(a) The key properties of cerium-doped LaBr$_3$ inorganic crystal scintillator [81].
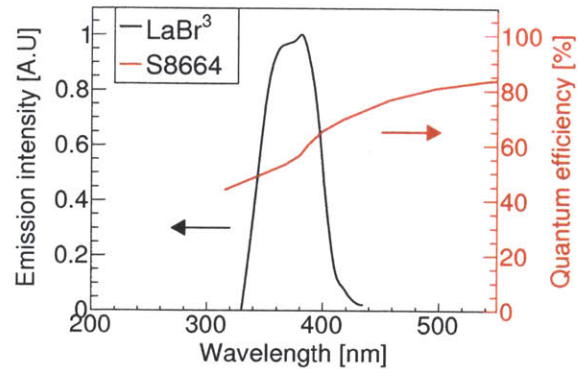
(b) LaBr$_3$ scintillation emission spectrum and SiAPD quantum efficiency

Figure 4-13: The principal optical properties of the LaBr$_3$ inorganic scintillator. The high light emission and high quantum efficiency of the Hamamatsu S8664-1010 SiAPD at the peak emission wavelength of LaBr$_3$ result in excellent photon statistics.

scintillation photon output (38 000 per MeV deposited), reasonable energy resolution (~8% at 0.662 MeV), and ease of large crystal growth ($\lesssim$500 kg). However, cerium-doped LaBr$_3$, discovered only recently in 1999, is the first inorganic scintillator to substantially improve all of the important properties of scintillation crystals for gamma spectroscopy, including light output, light decay time, mass density, average atomic number, and optical absorption length [79, 80]; the properties of LaBr$_3$ as manufactured by Saint-Gobain in 2013 are shown in Table 4-13a

The high mass density and high average atomic number make high energy ($\gtrsim$1 MeV) gamma spectroscopy feasible even with small scintillator crystals; the high light output ensures adequate photon statistics are accumulated by small surface area photon readout devices such as SiAPDs or SiPMs, leading to compact and robust detectors that are operable in magnetic fields [77]. Although the scintillation emission spectrum, with a peak emission wavelength of 380 nm, is at the low end of the S8664-1010 SiAPD quantum efficiency curve, as shown in Figure 4-13b, the quantum efficiency of the SiAPD approaches nearly 50%, and the high scintillation light output ensures sufficient light collection.

Relative to the EJ301-PMT detector, spectroscopy with the LaBr$_3$-SiAPD detector is much less convoluted. The scintillation response of LaBr$_3$ is highly linear in response to gamma-induced electron energy deposition [82], making calibration relatively straightforward. LaBr$_3$ is also insensitive to neutrons, eliminating the need to discriminate between particle types, enabling dependable operation in mixed radiation fields, and able to withstand high neutron fluxes in a fusion environment [83]. All of these features combine with the intrinsic high energy resolution provided by the scintillator crystal to make LaBr$_3$ an excellent scintillator for gamma spectroscopy in AIMS.

69
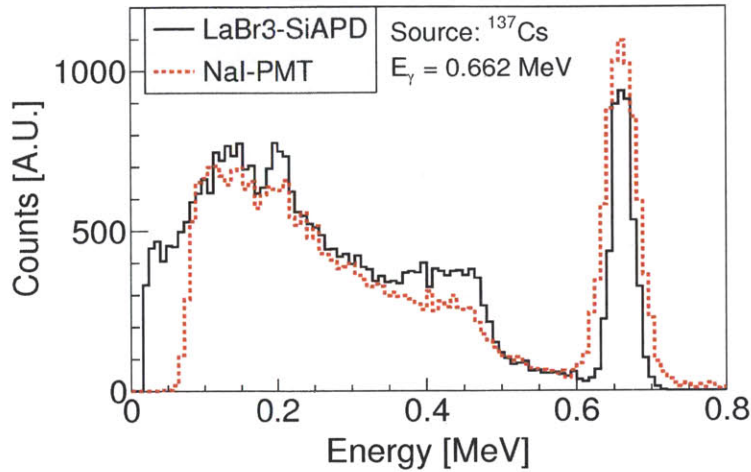
Figure 4-14: The experimental response of the LaBr$_3$-SiAPD detector to 0.662 MeV gammas from a cesium-137 check source. The responses were computed with the digital acquisition and pulse processing methods described in Section 4.4. The LaBr$_3$-SiAPD detector achieves 1.9 times better energy resolution than a standard PMT-coupled NaI-PMT detector.

4.6.2   Spectroscopy

Figure 4-14A shows the LaBr$_3$-SiAPD energy spectrum for 0.662 MeV monoenergetic gammas from a cesium-137 check source. The detector shows a high resolution peak centered on the incident 0.662 MeV gamma energy, reflecting the strong photoabsorption provided by the dense, high average atomic number crystal. The Compton scattering continuum is evident below the photopeak, including a very sharp Compton edge at 0.478 MeV. Also shown, for comparison, is the response of a 5.08ϕ×5.08 cm thallium-doped sodium-iodide (NaI) crystal coupled to a 2-inch PMT to 0.662 MeV gammas. As NaI-PMT detectors have been the gold standard of scintillator-based gamma detection for well over half a century, it is a testament to the performance of the LaBr$_3$-SiAPD detector that it can provide approximately twice the energy resolution at 0.662 MeV with good counting statistics compared to the NaI-PMT detector and with a significantly smaller scintillation crystal. In fact, energy resolutions of approximately 2.0% at 0.662 MeV have recently been achieved with strontium and calcium doping of the LaBr$_3$ crystal [84].[3]

---

[3]Energy resolution for scintillation detectors is evaluated at a specific energy, often at the 0.662 MeV gamma peak from ^{137}Cs. The energy resolution is typically calculated as the Gaussian peak full width at half maximum divided by the peak location in the energy spectrum.

4.6.3 Calibration

As discussed above, the scintillator response of $LaBr_3(Ce)$ crystals is highly linear to gamma-induced electron energy deposition. The calibration of the detectors is straightforward. First, the detector is exposed to a set of gamma check sources with the DAQ being used to perform digital spectroscopy. The position of the gamma peaks in the spectra (in ADC units) at known energies provides the set of points that construct the calibration curve. The calibration curve is used during data analysis to convert waveform integrals in units of ADC to energy units.

An important aspect of the $LaBr_3$-SiAPD detector is its gain sensitivity to temperature. The gain decreases by four percent for every ^oC increase. In conditions where the temperature may drift, the measurement times must be less than the temperature fluctuation timescales in order to avoid degrading spectroscopy performance. Under conditions where the temperature drifts slowly but measurements can still be performed, *in-situ* calibration of the detector before and after an AIMS measurement can be used to correctly evolve the calibration curve over the course of many measurements, thus ensuring a correct energy calibration.

Chapter 5

Computational Modeling

Modeling has played a key role in the design and execution of the AIMS diagnostic on Alcator C-Mod. During the design phase, scoping studies had to be performed in order to ensure that the injection of the deuteron beam was optimized - from the perspective of maximizing the effectiveness of AIMS measurements - and that the design and location of the neutron and gamma detectors in the tokamak superstructure provided high resolution energy spectroscopy with acceptable signal-to-noise ratio. Once experimentally implemented, modeling can function as a "synthetic diagnostic", where simulation plays a key role in the interpretation of experimental measurements for the extraction of absolute PFC surface compositions.

The purpose of this chapter is to present three modeling developments in support of AIMS on Alcator C-Mod: a single-particle dynamics code for optimization of the RFQ beam injection configuration; a new Monte Carlo model for simulating the nonlinear scintillator responses common to most organic scintillators; and a Geant4-based synthetic diagnostic for comprehensively simulating AIMS measurements of PFC surface composition in Alcator C-Mod.

5.1 AIMS single-particle dynamics code

In order to satisfy the diagnostic requirements of AIMS on Alcator C-Mod, the injection position and angle of the deuteron beam from the RFQ accelerator must be carefully optimized. The point at which the beam is injected is set by a small access flange that admits the beam into the tokamak vacuum vessel. The injection angle of the beam is set by the position and rotation of the RFQ accelerator. Neglecting engineering constraints, the optimum injection configuration is a function of the magnetic fields required for beam steering and the total amount of accessible PFC surfaces. To avoid excessive resistive heating of the magnets and to minimize the demands on the magnet power supply, the required coil currents should be as low as

73

possible; to maximize the impact of AIMS, the beam should be able to access the largest PFC surface area as possible. The optimization must, therefore, model the magnetic beam steering with the three dimensional environment of the tokamak in order to evaluate the field requirements and PFC surface accessibility.

5.1.1 Integrating the equations of motion

To perform this optimization, a three dimensional beam steering code was developed using IDL in order to utilize the prior geometric modeling of the Alcator C-Mod vacuum vessel and internal components. Because this code was intended to provide an approximate evaluation of beam steering over the large parameter sweeps required for optimization, a first-order accurate integration scheme provides an acceptable tradeoff of cheap computation and relatively good accuracy for the calculation of the beam trajectory. For simplicity, a cartesian coordinate system centered at the tokamak axis of symmetry and midplane was chosen with the following convention: $+\hat{x}$ points radially outward centered on a radial diagnostic port; $+\hat{z}$ point vertically upwards starting at the midplane; $+\hat{y}$ is such that the coordinate system is right handed. The coordinates are shown for reference in Figure 5-1.

The code models the charged deuteron beam as a single particle moving through the tokamak magnetic fields.[1] The deuteron interacts with the vector sum of the toroidal and vertical magnetic fields, $\mathbf{B} = \mathbf{B}_\phi + \mathbf{B}_v$, via the Lorentz force

$$m\frac{d\mathbf{v}}{dt} = \mathbf{F} = q\mathbf{v} \times \mathbf{B} \tag{5.1}$$

where m and q are the mass and electric charge of the deuteron. The position of the deuteron can easily be evolved with a forward Euler scheme to numerically integrate the equations of motion:

$$\frac{\mathbf{v}^{n+1} - \mathbf{v}^n}{t^{n+1} - t^n} = \frac{q}{m}\begin{vmatrix} \hat{x} & \hat{y} & \hat{z} \\ v_x & v_y & v_z \\ B_x & B_y & B_z \end{vmatrix} \tag{5.2}$$

where the deuteron velocity and position components at the $n+1$ time step are given

---

[1] It should be noted that modeling high current ion beams in magnetic fields, such as those produced by RFQ accelerators, neglects many important effects that must be considered in order to correctly optimize beam focusing optics and to predict the beam resolution at the PFC surface [85, 86]. For the calculation of approximate beam centroid trajectories during large parameter sweeps during diagnostic scoping, a first order Euler scheme was determined to be acceptable. For detailed modeling of the RFQ beam dynamics in AIMS measurements, the interested reader is referred to [55].

by

$$v_x^{n+1} = v_x^n + \frac{q\Delta t}{m}\left(v_y B_z - v_z B_y\right) \tag{5.3}$$

$$v_y^{n+1} = v_y^n - \frac{q\Delta t}{m}\left(v_x B_z - v_z B_x\right) \tag{5.4}$$

$$v_z^{n+1} = v_z^n + \frac{q\Delta t}{m}\left(v_x B_y - v_y B_x\right) \tag{5.5}$$

$$x^{n+1} = x^n + v_x^{n+1}\Delta t \tag{5.6}$$

$$y^{n+1} = y^n + v_y^{n+1}\Delta t \tag{5.7}$$

$$z^{n+1} = z^n + v_z^{n+1}\Delta t \tag{5.8}$$

$$\tag{5.9}$$

In the chosen cartesian coordinate system, the vector components of the magnetic field, $\mathbf{B}$, are given by

$$B_x = \frac{B_0 R_0}{\sqrt{x^2 + y^2}}\cos\left(\frac{\pi}{2} - \tan^{-1}\frac{y}{x}\right) \tag{5.10}$$

$$B_y = \frac{B_0 R_0}{\sqrt{x^2 + y^2}}\sin\left(\frac{\pi}{2} - \tan^{-1}\frac{y}{x}\right) \tag{5.11}$$

$$B_z = B_v \tag{5.12}$$

$$\tag{5.13}$$

where B_0 is the toroidal magnetic field on the magnetic axis R_0, which is 0.67 m for Alcator C-Mod.

5.1.2 Optimization of deuteron injection

The deuteron trajectory integrator is coupled to a realistic 3D boundary of the interior of Alcator C-Mod, including the diagnostic ports, vacuum vessel, divertor, limiters, and PFC tiles. The deuteron can then be tracked through the magnetic fields until it intercepts the boundary, where the hit position is recorded as a function of the toroidal and poloidal field magnitudes. Optimization of the injection configuration can then be performed by "sweeping" the toroidal and vertical magnetic fields during scans of the parameter space. Parameters of interest include the injection position (x,y,z) and angles of the deuteron beam with respect to the radial diagnostic port flange.

The final optimized position for injection is shown in Figure 5-1, where the beam trajectories and the hit locations are colored by the value of the toroidal magnetic steering field. The coverage of the PFC surface is excellent, with the beam able to access the central column, inner divertor, divertor floor, and outer divertor; by reversing the toroidal field, the beam can be swept in the opposite direction to scan
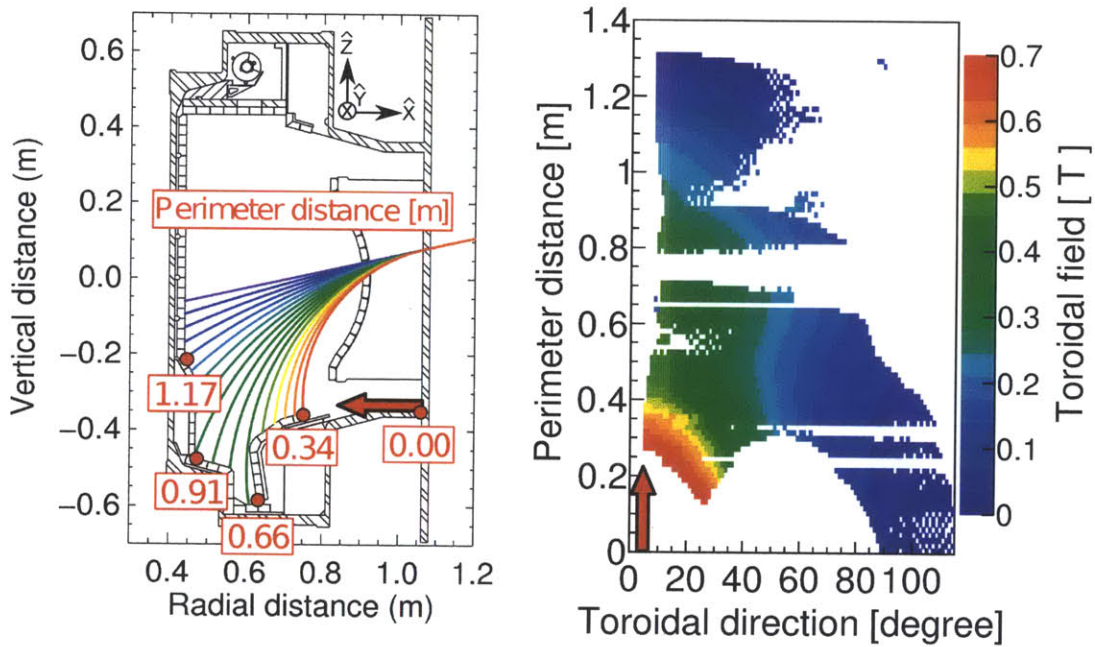
Figure 5-1: The single-particle beam trajectory code computes accessible PFC surface locations - shown here as functions of the toroidal magnetic field used for beam steering in the poloidal direction- for the optimized installation position of the RFQ accelerator on Alcator C-Mod. The vertical magnetic field used for beam steering in the toroidal direction is not shown.

the upper half of the first wall. The beam can scan over 90 degrees toroidally in both directions by reversing the vertical field, thus providing an enormous range of measurement locations. Most importantly, all of these locations can be accessed with $\lesssim 0.7$ T of toroidal field and $\lesssim 0.08$ T of poloidal field, which are small enough to ensure adequate magnet cooling between plasma shots and to be provided by standard steady-state power supplies. For reference, Alcator C-Mod typically operates with its toroidal field between 5 and 8 T during plasma shots.

The code serves a number of other important functions. During AIMS experiments, it provides the required magnetic field values to steer the beam to a particular measurement location. It also serves to calculate the angle between the deuteron beam impact vector and the detector position vector during experimental data analysis, which is a required input for the nuclear reaction kinematics described in Chapter 3.

5.2   A new scintillation model for Geant4

As will be presented in the following section, the comprehensive modeling of PFC surface measurements, which require high-fidelity simulations of the scintillation detector responses within the environment of Alcator C-Mod, is an essential component of AIMS. Available simulation tools, however, were found to be inadequate for this purpose, and work was undertaken to develop new scintillation detector modeling capabilities, particularly for organic scintillators such as the EJ301 liquid that composes the EJ301-PMT detector in AGNOSTIC.

The simulation of organic scintillation detectors in neutron and gamma fields has long been of interest to the detector physics community for two primary reasons. First, simulation helps interpret the complex detector response functions that are generated by the nonlinear production of scintillation photons as a function of energy deposited and ionizing particle type. Second, simulation can easily generate a large number of detector response functions for various incident particles, which can be difficult to obtain experimentally. These response functions are required as inputs to unfolding codes that deconvolve the incident particle energy spectrum from the detector response. In addition, simulation can play an important role in the computational design and optimization of new types of particle detectors that are based on organic scintillators.

In this section, the implementation and validation of new organic scintillation detector modeling capabilities are presented. The method enables the simulation of time-resolved production (linear or nonlinear), transport, and readout of photons in a detector of arbitrary geometry, scintillator choice, structural materials, and light readout configuration, all potentially within the complexity of an encompassing experiment geometry [6]. The code was written in collaboration with Peter Gumplinger of TRIUMF, and, as an indication of its widespread utility in detector modeling outside of AIMS simulation, has been incorporated into Geant4 [87], one of the leading

Monte Carlo particle transport codes for high energy, nuclear, space, medical, and detector physics. This is the first time that such comprehensive organic scintillator-based detector modeling can be performed within a single Monte Carlo (MC) code, leading to significant improvements in the simulation of detector response in complex environments and the optimization of advanced design for scintillation detectors.

5.2.1 The need for a new approach

The most widely used configuration for organic scintillation detectors is a right cylinder scintillator coupled to a PMT of similar size to optimize light collection. However, new scintillator materials, such as PSD-capable plastic [88] and new light readout devices, such as silicon photomultipliers (SiPM), can now be used to fabricate detectors in a wide variety of complex geometries, materials, and light readout configurations. For these "advanced" organic scintillation detectors, the capability to perform high fidelity modeling of the detector response functions and pulse shape discrimination (PSD) would greatly enhance computational detector design.

Existing codes are not well suited to such work. Although used successfully for decades to model organic scintillation detectors, codes such as SCINFUL [89] and NRESP7 [90] are limited to right cylinder geometries, provide limited particle sources, do not model the light readout device, and restrict the simulation boundary to the detector itself. Recently, codes such as MCNP-PoliMi [91] and MCNPX-PHOTRACK [92] have extended somewhat the detector complexity and simulation domain that can be modeled but require significant post processing, code coupling, and have not been shown to model the time resolved photon transit time critical for simulating PSD.

One of the principal motivations for this work was to develop a single MC code that could comprehensively model the optical physics of advanced organic scintillation detectors. This can play an important role in guiding detector design and optimization, such as using SiAPDs or SiPMs with EJ301 for a robust, magnetic field-insensitive neutron detector for AIMS. A second motivation was the desire to include this capability within the framework of a general purpose MC code - Geant4 in particular - in order to calculate detector response functions within a larger simulated experiment, such as simulating the AGNOSTIC detector responses inside of the Alcator C-Mod superstructure.

5.2.2 Scintillation model

Geant4 is an object-oriented C++ Monte Carlo toolkit for simulating the passage of particles through matter [87]. Most aspects of simulating EJ301-based scintillation detectors with Geant4 have been extensively studied [71, 93, 94, 95, 96].

All of these studies, however, neglect the production, transportation, and detection

of scintillation photons, choosing to score the energy deposition in the scintillator volume and then to apply scintillation response and detector resolution functions to replicate the full experimental detector response. While successful in many applications, this approach is not ideal as it obscures the influence of optical properties on the detector response, requires substantial knowledge of the scintillator light response and detector energy resolution, necessitates post-processing work by the user to generate detector response functions, and is not applicable to computationally exploring complex detector geometries or nonstandard light readouts.

In Geant4, as in all other MC codes, a continuous particle trajectory is necessarily broken into many small steps in order to correctly simulate the passage of the particle through matter, which has important implications for simulating the scintillation light response. In scintillators with a linear response, light production is directly proportional to the ionizing energy deposited in the scintillator. Thus, the total light produced along a particle track in the scintillator can be computed as the sum of the light produced in smaller steps without regard for the kinetic energy of the ionizing particle at each energy-depositing step.

In scintillators with a nonlinear response, the light produced in each step must be computed as

$$L_{\text{step}} = L(T, x) - L(T - E_{\text{dep}}, x) \tag{5.14}$$

where L is the number of scintillation photons, T is the kinetic energy of the charged particle before the step, E_{dep} is the total ionizing energy deposited in the scintillator during the step, and x is the charged particle type depositing energy. In addition to correctly modeling the total light produced by a multiple step ionizing particle track in a scintillator, this methodology accounts for two important cases. First, light is produced correctly for incomplete energy deposition of the charged particle, such as is the case where the particle exits the scintillator volume ("wall effects") or in the case that the particle is absorbed in a nuclear reaction. Second, the scintillation photon density is larger in the high kinetic energy portion of the ionizing particle track in the usual case where the nonlinear photon yield increases with particle energy.

A complete description of the code implementation of the scintillation model, along with the full machinery of optical photon production, transport, and detection in Geant4, is well outside the scope of this thesis[2]. In short, the light yield of a scintillator - linear or nonlinear - can be fully defined by the user as a function of deposited energy independently for electrons, protons, deuterons, triton, alphas, and heavy ions. When combined with the other user-specified scintillator properties, such as the photon emission spectrum, pulse rise time, pulse exponential decay time(s), fast-to-slow charge ratio, absorption length, and refractive index, any arbitrary scintillator may be modeled in Geant4.

---

[2]The complete optical physics capabilities of Geant4 and instructions to implement them in user simulations may be found in the Geant4 User's Guide for Application Developers, Section 5.2.5 [97]

5.2.3 Validating the model

In order to confirm the capability of Geant4 to correctly simulate the detector responses of organic scintillators, a series of computational and experimental validation tests were performed. The tests attempted to validate the response functions generated by Geant4 against a leading organic scintillation detector simulation code and experiments conducted in the laboratory. The tests covered a wide energy range for both gammas (0.511 to 1.274 MeV) and neutrons (0 to 20 MeV). All Geant4 detector response functions were produced with version 10.0-beta, using the EJ301 light responses of Verbinski [67] to model the scintillation light output as functions of energy deposited and particle type.

The Geant4 physics list was constructed using the standard prepackaged and validated class collections of relevant physics: G4EmStandardPhysics for electromagnetic interactions; HadronPhysicsQGSP_BIC_HP and HadronElasticPhysicsHP for hadronic interactions; G4DecayPhysics for particle decay; and G4OpticalPhysics to include the production and transportation of scintillation photons. The neutron high precision (HP) data transport model used the standard G4NDL4.3 neutron data library that is distributed with Geant4.

Two detectors were used for experimental validation: the first is the EJ301-PMT detector described in Chapter 4 that was used in AGNOSTIC on Alcator C-Mod; the second detector is a 25.0×25.0×8.2 cm cell of EJ301 coupled to a single 3 inch diameter PMT that was custom manufactured by Scionix. A 2 cm thick aluminum vessel contains the EJ301 scintillator and provides structural support.

Ensuring equivalent detector response functions

When comparing two organic scintillation detector response functions, the response functions must have identical units and be appropriately scaled to one another by requiring that integrals under the two response functions for identical ranges are equal.

In Geant4, response functions are generated by histogramming the number of detected photons per event for all simulated events, giving the X-axis units in detected photons by default. The detector response produced by many other simulation codes is typically given as light versus counts, where light is in the ubiquitous units of "MeV-electron-equivalent", or MeVee. In this paper, the unit MeVee is defined as the scintillation light produced by 1 MeV deposited in the scintillator by electrons. In order to compare other codes to Geant4, the light value can be multiplied by the scintillator photon yield - 12 000 photons per MeV deposited by electrons for EJ301 - to convert X-axis units of the response function histogram from MeVee to total detected photons.

Comparing Geant4 to experimental response functions is more complicated due to
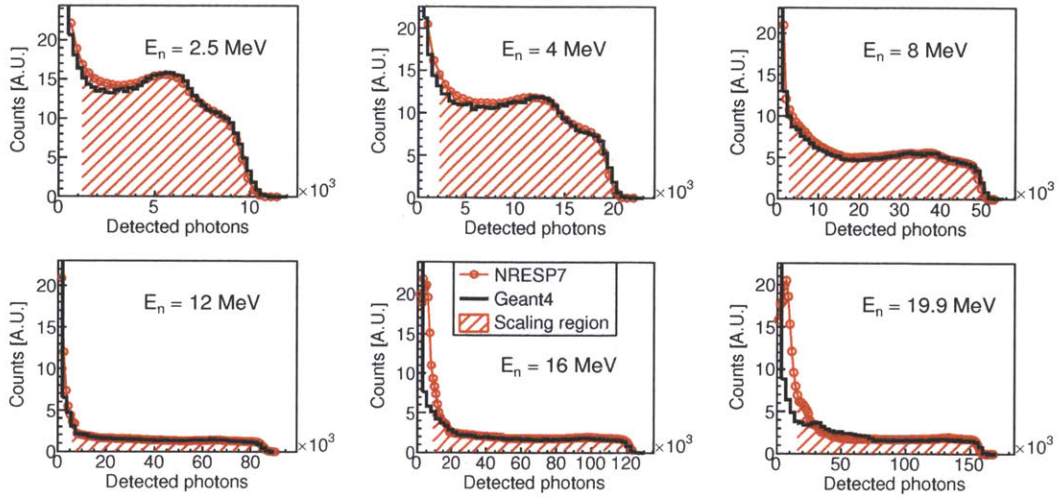
Figure 5-2: Comparisons between NRESP7 and Geant4 simulated detector responses of a $5.08\phi \times 5.08$ cm right cylinder of EJ301 to monoenergetic neutrons.

detector calibration. Typically, two or more monoenergetic gamma energies are used to experimentally place the X-axis calibration on an absolute linear scale [67], which determines the conversion from pulse height (units defined by the data acquisition system) to light produced (units of MeVee). Because the approach taken by Geant4 simulates physical reality to such a high degree, a simulated calibration - identical to the experimental one - must be performed to convert the X-axis of the simulated response function histogram from detected photons to MeVee. Once the calibration is established - experimental and simulated - Geant4 and experimental response functions for any equivalent particle flux may be correctly compared.

Computational validation against NRESP7

NRESP7 is one of the most widely used and validated codes for the simulation of EJ301-PMT detectors for incident fast neutrons up to 20 MeV [90]. It has been successfully used at Physikalisch-Technische Bundesanstalt in Germany for almost 30 years for the simulation of EJ301-based detector response functions [66].

A simulated $5.08\phi \times 5.08$ cm right cylinder of EJ301 was constructed in Geant4 and NRESP7. The detector geometry and optical properties were made as identical as possible between the two codes. The detectors were then irradiated in the simulations with monoenergetic neutrons along the axial dimension of the scintillator up to 19.9 MeV, the high energy cutoff for NRESP7 and Geant4's `NeutronHP` data-driven transport model.

Six results comparing detector response functions from NRESP7 and Geant4 at different incident neutron energies are shown in Figure 5-2; the shaded area depicts the

integration range used to scale the Geant4 response functions to those of NRESP7. Overall, the comparison shows close agreement between the two codes over the entire detector response functions and across the energy range of incident neutrons. Several features in particular demonstrate excellent agreement: the position of the high-energy edge, defined by the maximum energy transfer in the elastic scattering ^{1}H(n,n)^{1}H reaction; the peaked hump just below the high-energy edge caused by multiple scattering in a single event within the scintillator volume; and the rise at low energies for incident neutrons below 12 MeV, defined by the increase in light contribution from nuclear reaction exit channel alphas and ions.

There are two slight differences, one expected and one unexpected. The expected difference occurs in the disagreement of the low energy region of the detector response function for incident neutron energies above approximately 12 MeV. The cause is the inability of the NeutronHP model in Geant4 to correctly handle breakup reactions that become important at high neutron energies. Reactions such as

$$^{12}C(n, n')^{12}C^* \Rightarrow 3\alpha \qquad (5.15)$$

lead to light contributions in the low energy region of the detector response function due to energy deposition by deuterons, alphas, and heavier ions, which produce significantly less light than electrons or protons for the same energy deposited (See Figure 4-6). NRESP7 correctly includes these reactions, which lead to the higher light response. This discrepancy has been reported in the literature [71].

While the breakup reactions exists in the G4NDL4.3 neutron data library, the G4NeutronHP transport model presently handles the reaction as one-step inelastic reactions and does not model the breakup of the excited nuclei. For the example reaction presented in Equation 5.15, the $^{12}C^*$ does not decay into three alpha particles, leading to an underprediction of light in the low energy region of the detector response function. An update to G4NeutronHP, which would enable the correct handling of breakup reactions, is presently under development by the Geant4 collaboration and is expected in a future release.

The second, unexpected discrepancy in the comparison to NRESP7 occurs in the slight underprediction by Geant4 for the lower energy portion of the scattering continuum for incident neutrons below 5 MeV. This effect might be explained by either slight disagreements in the ^{1}H(n,n)^{1}H differential cross section or in differences of light transport between Geant4 and NRESP7.

While the latter issue warrants further study, the overall results show excellent agreement between the two codes. More importantly, the NRESP7 results shown in Figure 5-2 have been shown to replicate experimental measurements with high accuracy [66], giving further validity to Geant4's ability to correctly simulate the detector response functions to neutrons for EJ301.
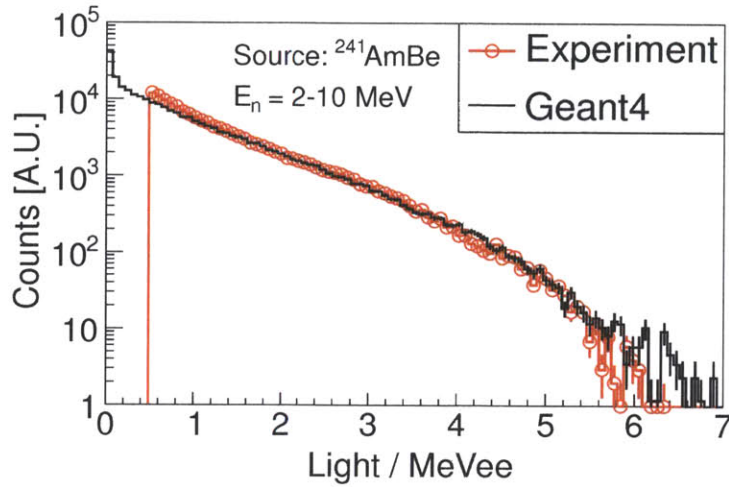
Figure 5-3: A comparison between the experimental and Geant4 simulated detector responses for the large cuboid ($25 \times 25 \times 8.2$ cm scintillator cell) EJ301-PMT detector when exposed to neutrons and gammas from a ^{241}AmBe source.

Experimental validation against ^{241}AmBe neutrons

For this experiment, the large EJ301-PMT detector ($25 \times 25 \times 8.2$ cm scintillator cell) was exposed to an ^{241}AmBe source with the goal of replicating the experimental neutron detector response with Geant4. The source was placed approximately 15 cm above the center of the square face of the detector. Two sets of data were taken, one with the source in place and one with the source removed. The latter spectrum was subtracted from the former to remove the particle background from cosmic rays and terrestrial decay events. Data was collected long enough to obtain a smooth experimental detector response function with excellent statistics. For the Geant4 simulation, the complex ^{241}AmBe neutron emission spectrum was taken from the recommended ISO standard [75], and gammas, produced by inelastic neutron collisions with the detector, were filtered out of the final detector response function in the simulation.

Because the detector was used in a mixed neutron and gamma field, digital PSD, described in Chapter 3, was performed to eliminate the gamma events from the final neutron spectrum. The PSD figure-of-merit for this detector , given in Eq. 4.4, was evaluated at 1.03 at 0.5 MeVee, which is taken to tbe the lowest energy at which PSD can be considered adequate for removing gammas from the spectrum.

Close agreement between the experimental and simulated response functions, shown together in Figure 5-3 are achieved over almost the entire response within the statistical uncertainties; a few spurious high energy events appear in the simulated spectrum. The slight deviation at lower energies in the experimental spectrum is attributed to deteriorating PSD enabling leakage of gamma events into the neutron spectrum; the

(a) 0.662 MeVee gammas from ^{137}Cs

(b) 0.511, 1.274 MeVee gammas from ^{22}Na
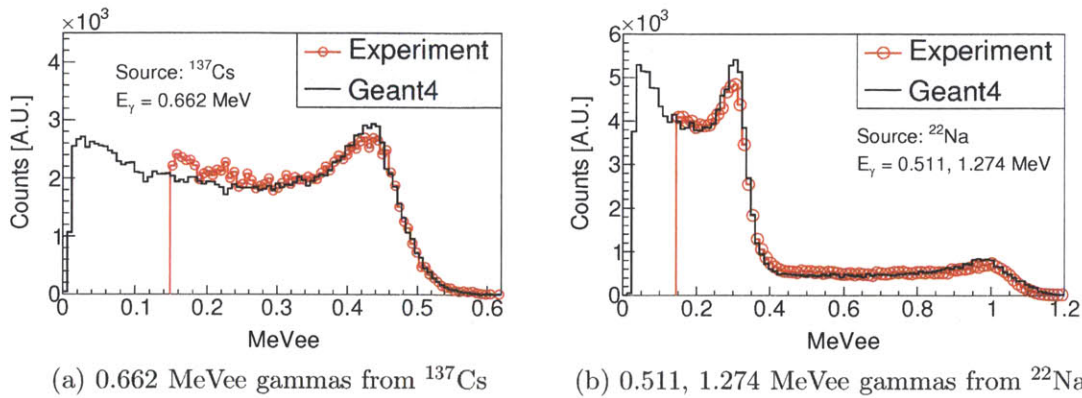
Figure 5-4: A comparison between the experimental and Geant4 simulated responses for the EJ301-PMT detector when exposed to different monoenergetic gammas from standard check source.

experimental spectrum is cutoff at the PSD-determined lower threshold of 0.5 MeVee. Overall, the results indicate that Geant4 is capable of correctly simulating organic scintillation detector response functions for incident neutrons in the 0-10 MeV range, despite an unusually large, suboptimal detector and a complicated incident neutron spectrum.

Experimental validation against monoenergetic gammas

For this experiment, the small EJ301-PMT detector used for AGNOSTIC was exposed to three monoenergetic gammas from standard check radioisotope source: 0.662 MeV gammas from ^{137}Cs in the first run; and 0.511 and 1.274 MeV gammas simultaneously from ^{22}Na in the second run. The sources were placed approximately 5 cm from the flat face of the cylindrical scintillator housing and were aligned with the cylinder's axis of symmetry. Data was collected long enough to ensure a smooth experimental response function with excellent statistics. Because essentially zero neutrons interacted with detector during the few seconds of source irradiation, PSD was not required. Background subtraction was not required due to the extremely high detector count rates from the radioactive sources.

The experimental gamma response functions are compared to the simulated Geant4 response functions in Figure 5-4. For 0.662 MeV gammas, the simulated response closely matches the experimental response, with agreement over most of the response better than approximately 5%. The simulated response correctly replicates the position of the Compton edge at 0.48 MeVee, the shape of the broad Compton continuum, and the intrinsic detector resolution. The simulation slightly underpredicts the response at the lowest light levels, which is attributed to a small number of downscattered gammas from the PMT and ambient geometry in the experiment; the PMT and room were not modeled in the simulation, accounting for the difference in scattering.

For the simultaneous exposure to 0.511 and 1.274 MeV gammas, the simulated and experimental response function again agree within a few percent, with the exception of a slightly sharper simulated detector energy resolution at the 0.341 McVec peak. Again, the same simulated underprediction at the lowest light levels is attributed to a small number of downscattered gammas. Overall, the results indicate that Geant4 can simulate EJ301 detector responses to gammas in the 0.511-1.274 McV gamma energy range to better than 5% agreement over most of the response function.

Scintillation pulse and photon transport

To validate the capability of Geant4 to study the timing properties of organic scintillators, Geant4 was used to simulate individual pulses of scintillation light from EJ301 in response to incident particles; the simulated pulses were then compared to experimental pulses. The particle-dependent fraction of light in the long time component decay tails was achieved by attaching unique scintillation processes to each particle type.

Two pulse comparisons, one for protons and one for electrons, are shown in Figure 5-5. In order to ensure an equivalent comparison, the simulated and experimental peak position was used to align the pulses on the time axis, and the peak amplitude was used to align the pulses on the intensity axis. While Geant4 does not exactly capture the pulse rise time, the crucial components of the pulse for distinguishing particles - the decay tail - is replicated to a very high degree.

Two conclusions can be drawn. First, Geant4 models the first two light decay components very well for both electrons and protons, correctly replicating the arrival and detection time of the photons at the PMT. This indicates that the optical transport and detection of individual scintillation photons within the detector is being handled correctly. Second, Geant4 is capable of simulating the energy distributed between the first and second light decay components for different particles, as evident by the larger second-component decay tail for the proton pulses. Geant4 is not presently able to model more than two decay components, but these are not critical for modeling PSD in EJ301.

Because the simulated pulses reflect the features that form the basis of distinguishing particle types using the decay tail shape, Geant4 is capable of simulating PSD. For example, Geant4 was used to simulate PSD for the AGNOSTIC EJ301-PMT detector in response to neutrons and gammas from the ^{241}AmBe source. The results appear in Figure 5-6 and reflect the excellent PSD capability enabled by the efficient light collection of the small, optimized detector. More importantly, because scintillation photons are generated, transported, and detected using the full MC features described in this paper, synthetic PSD can be performed for a detector of arbitrary geometrical complexity and light readout configuration. This enables the detector physicist to evaluate computationally, for example, the effect on PSD capability of scintillator size and geometry, long light guides or fibers, the substitution of large PMTs with

85
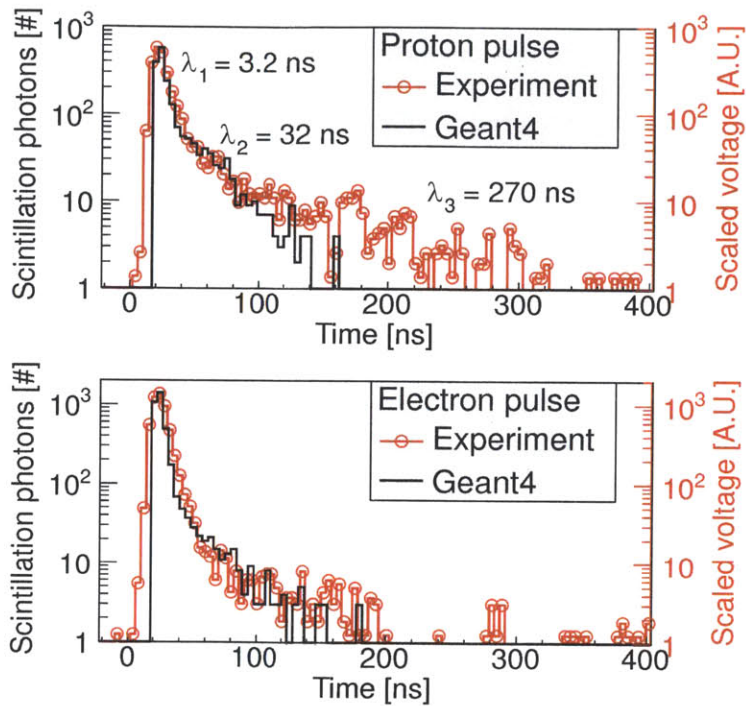
Figure 5-5: Comparisons between the experimental and Geant4 simulated individual detector pulses produced by a proton (top) and an electron (bottom) in the EJ301-PMT detector. At present, Geant4 is presently only capable of simulating the first two decay components.
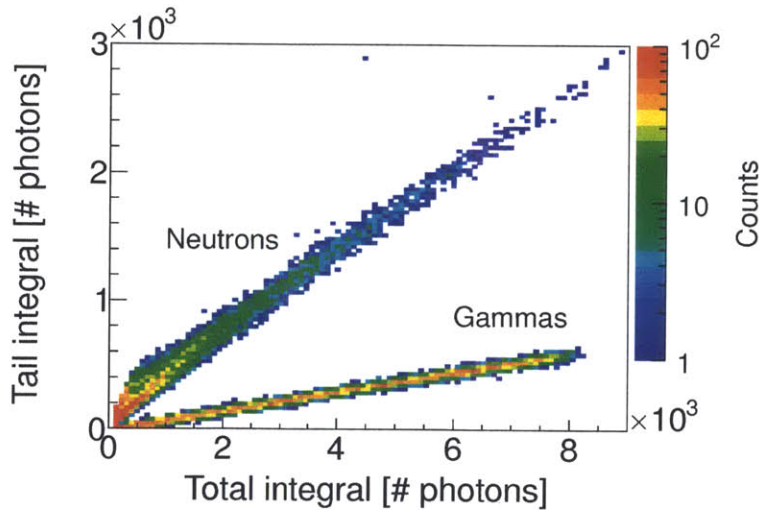
Figure 5-6: An example of simulated PSD for the EJ301-PMT detector when using a simulated ^{241}AmBe source. The excellent light collection of the detector is evident in the clear separation of neutrons and gammas down to the lowest energies.

small SiPMs, or various reflective coatings.

5.2.4 Conclusions for nonlinear scintillator response simulation

The new methods for simulating the response of scintillators presented here provide, for the first time, the ability to simulate a an organic scintillation detector of arbitrary complexity and configuration within a single Monte Carlo code. For AIMS and the detector physics community at large, this is important for two reasons. First, with its extensive physics, geometry, and particle transport modeling, Geant4 facilitates comprehensive detector simulation within an experimental environment, a crucial need in many types of experiments. Second, new types of scintillation detectors, which deviate from the standard PMT-coupled right cylinder of liquid organic scintillator, can be modeled, from scintillator type to optical transport to light readout devices. Although we used PMT-coupled EJ301 detectors for our validation work, the extensibility of the method provides a framework for the evaluation of any type of scintillator and optical readout device so long as the scintillation response and optical property data are correctly input into Geant4.

While previous codes will continue to serve the detector physics community well for certain applications, Geant4 now provides a more flexible and extensible environment for the simulation of organic scintillation detectors. This capability should significantly aid users who require a more powerful capability to simulate detectors within larger experiments or to computationally evaluate advanced detector designs. For AIMS, Geant4 is now being used to guide the development of new types of EJ301-based detector and to simulate the detector response of EJ301-based detectors within the complex environment of Alcator C-Mod, as described in the next section.

5.3 ACRONYM: an AIMS synthetic diagnostic

The ability to simulate the *in-situ* measurement of PFC surfaces plays a multifaceted role in AIMS. During the adaptation of *ex-situ* IBA to the tokamak environment, simulation was used to evaluate the effects of detector type, detector location, and measurement location on the feasibility of performing AIMS measurements; similarly, during the design of a specific AIMS diagnostic, such as AGNOSTIC on Alcator C-Mod, simulation can be used to optimize the the experimental configuration within the geometrical constraints of the tokamak, evaluating the impact of different locations on the measurement quality.

Perhaps most importantly, simulation can be used to interpret the experimental data that is acquired once the diagnostic is operational, providing physical insight into complicated data sets and extracting absolute measurement quantities, such as isotopic

concentration or layer thicknesses. For AGNOSTIC on Alcator C-Mod, ACRONYM [3] is the comprehensive synthetic diagnostic for simulating AIMS measurements.

5.3.1 Overview of ACRONYM

ACRONYM is a Monte Carlo particle-in-matter simulation that is written with the Geant4 toolkit [87]. Mentioned above, Geant4 is an object-oriented C++ toolkit for simulating the passage of particles in matter; it provides an extensive range of theory- and data-driven physics models, particle transport in electromagnetic fields, complex geometries, variance reduction, and powerful data extraction methods [87]. ACRONYM contains the geometry, physics, detector models, and Monte Carlo tools to fully simulate AIMS measurements. When large computation power is required, ACRONYM can be compiled with parallel flags to utilize the Message Passing Interface (MPI) 2 standard code that handles distribution, processing, and aggregation of events. ACRONYM has been successfully compiled with Open MPI and MVAPICH2 and run on up to 256 processors with excellent performance scaling.

While many other mature Monte Carlo codes exist, such as MCNP [98] or FLUKA [99], Geant4 has three unique advantages over other codes. First, it alone contains extensive optical physics modeling, which is now augmented by the new scintillation model presented in Section 5.2. These features enable high-fidelity modeling of the AIMS scintillation detectors within the experimental geometry of Alcator C-Mod. Second, Geant4 is easily the most flexible and extensible major Monte Carlo code available. Its C++ object-oriented toolkit architecture provides essentially unlimited freedom to the programmer, to modify the source code, incorporate his or her own physics models, and link directly into data output formats and analysis programs. Its flexibility enables complicated, multistep experiments such as AIMS measurement to be entirely modeled within a single simulation framework, which is not possible with the fixed inputs and limited extensibility of MCNP or FLUKA. Finally, Geant4 is extremely user-oriented, with a large user base, very active community forum, and responsive developer group that fosters an environment for excellence in simulation.

Geometry, material, and fields

The tokamak superstructure geometry in ACRONYM was taken directly from the official engineering computer-aided design (CAD) models of Alcator C-Mod. At present, the direct importation of CAD models into Monte-Carlo particle transport codes can be prohibitively expensive for extremely complex geometries. Instead, the geometry was painstakingly translated by hand from the CAD models in the standard Geant4 geometry volumes. While great demands were placed on the author, the use of native Geant4 geometry volumes to model the most critical elements of the tokamak super-

---

[3] Alcator C-Mod RFQ Optical and Nuclear Yield Model

(a) ACRONYM   (b) Engineering CAD model
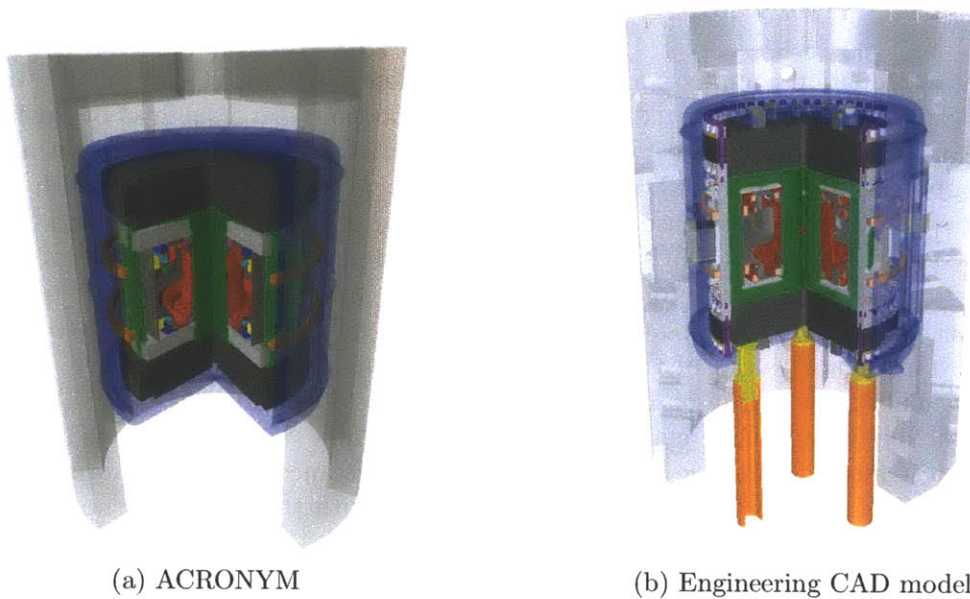
Figure 5-7: A comparison between the ACRONYM model (left) and the official engineering CAD solid model (right) of the Alcator C-Mod tokamak and superstructure, showing that the Monte Carlo particle transport in ACRONYM occurs in a high-fidelity representation of the real geometry.

structure resulted in an extremely efficient code for particle transport. Future versions of AIMS synthetic diagnostics will hopefully be able to utilize the recent advances in high efficiency importation of CAD geometry for Geant4 now under development [100, 101].

A comparison of the geometry in ACRONYM with the original CAD model of Alcator C-Mod is shown in Figure 5-7, which shows the high level of detail at which the simulated geometry matches the physical geometry. All of the components that could significantly effect the particle transport are modeled in detail, particularly near the core of the device where the majority of AIMS-relevant particle transport occurs.

Each object in the ACRONYM geometry is composed of a material that matches its physical world counterpart. A custom materials library containing over 45 complex materials was written to provide a sufficient level of detail. Accurate to the isotopic level, each material provides Geant4 with the necessary physical parameters for particle transport.

The toroidal and vertical magnetic fields are also modeled in ACRONYM to provide accurate trajectories of the deuteron beam centroid. The deuterons are stepped through the magnetic fields with a fourth order accurate Runga-Kutta algorithm.

Variance reduction

Variance reduction comprises a large set of techniques in Monte Carlo particle transport that are used to either reduce the computation time at a fixed level of statistical error in the computed quantity or to decrease the level of statistical error at a fixed computation time. ACRONYM primarily utilizes geometry biasing, in which particle transport is modified based on the importance of the geometry volumes to the final computed quantity. In short, a single particle that enters a volume of higher importance is multiplied into many particles, each with a reduced weight; both the number of new particles created and the assigned weight is proportional to the ratio of importance values of the exiting and entering volumes. Conversely, a single particle entering a region of lower importance has a probability of being killed, with the probably determined, again, by the ratio importance values. The scored quantity of interest for each particle - detector counts, for instance - must be normalized to the weight of the scored particle to ensure fidelity with the analog, or non-variance reduced, Monte Carlo calculation.

Making use of the toroidal symmetry, the biasing of the geometry in ACRONYM is set at the arc level, where one "arc" corresponds to a 36 degree toroidal wedge of Alcator C-Mod with the wedge centered in toroidal angle about each radial diagnostic port. A geometry manager class handles the automatic biasing of all volumes based on a few simple input by the user. For most use cases, the importance of volumes in the arc containing particle detector(s) are high; importance decreases monotonically for each subsequent arc in both toroidal directions.

ACRONYM also makes use of source biasing, in which source particles are immediately killed before tracking begins based on user-defined criteria. For examples, particle emitted in a direction that have almost zero chance of reaching a detector should be killed before they waste CPU cycles in tracking. The user must be extremely careful to ensure that the final scored quantities are correctly normalized based on the particle source biasing parameters chosen for the problem.

Detectors

There are three main detectors modeled in ACRONYM . The first two are the LaBr$_3$-SiAPD and EJ301-PMT detectors that were used in AGNOSTIC and are described in detail in Chapter 4. The third is a ^{235}U fission-based thermal neutron detector that is used in the Alcator C-Mod experimental hall.

For the LaBr$_3$-SiAPD and EJ301-PMT detectors, the modeling includes not only the correct geometry and materials but also a full specification of the scintillator characteristics, detector optical properties, and light readout properties. The result is the precise simulation of the production, transport, and detection of scintillation photons that replicates the physical detector's performance and data output to a high degree, as will be discussed in Section 5.3.2. An image of both detectors in action
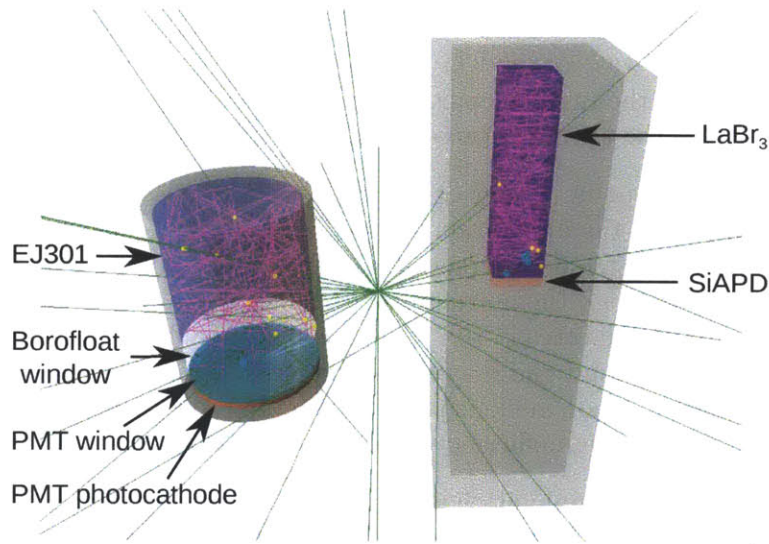
Figure 5-8: The EJ301-PMT (left) and LaBr$_3$-SiAPD (right) detectors responding to 0.662 MeV gammas (green) from a ^{137}Cs check source (center) in ACRONYM. The gammas interact with the scintillator (yellow dots) to produce scintillation photons (magenta) that are transported to the PMT photocathode or SiAPD, where they are detected (cyan dots).

during an ACRONYM simulation is shown in Figure 5-8.

The fission thermal neutron detector contains 93% enriched ^{235}U, which utilizes the extremely high fission cross section at thermal energies to detect neutrons. The detector, along with several other types of neutron detectors, is contained within a large ~cm thick steel canister and surrounded by a 9.7 cm and 7.1 cm shielding layers composed of lead and polyethylene, respectively, to moderate the 2.45 MeV prompt deuterium-deuterium fusion neutrons down to detectable thermal energies. The detector chosen for modeling in ACRONYM is Detector #5 in [102], where its configuration is described in detail. Properties of the detector that were not made available to the author were estimated as closely as possible from [53].

Deuteron-induced nuclear reactions

A core requirement of ACRONYM is that it must be able to simulate the production of neutrons and gammas from the incident low-energy $\lesssim$2 MeV) deuteron beam used in AIMS on the PFC surfaces, such as the nuclear reactions described in Chapter 3. Unfortunately, while data-driven, channel-based neutron reactions have long been incorporated into general purpose Monte Carlo particle transport codes such as Geant4 and MCNP, charged particle induced reactions are either completely absent

91

or based on parameterized models[4]. For light ions on low-Z isotopes, especially at the low energies $\lesssim 2$ MeV, as required in ACRONYM, there are at present no internal models that simulate the nuclear reactions of interest in any general purpose Monte Carlo code of which the author is presently aware.

Furthermore, from the point of view of simulating AIMS measurements, it is actually undesirable to simulate the interaction of every incident deuteron with the PFC surface. This is because a significant fraction of CPU time would be wasted in tracking the deuteron beam through the magnetic steering fields and producing the enormous number of incident deuterons ($\gtrsim 10^{16}$) needed to gain sufficient statistics from the relatively small neutron and gamma production cross sections. Clearly, an alternate approach for nuclear reaction modeling that accounts for low energy light ion reactions on low-Z materials with high efficiency is required for AIMS.

Recent work in the IBA community has begun the implementation and testing of such a model, using the incident beam parameters, material properties, and nuclear cross section data to efficiently calculate the yield of exit channel particles [103, 104, 105]. For a uniformly dense material containing an isotope i of element e, the total yield, of particle produced, Y, can be computed as

$$Y_i = N_d A^{-1} f_m f_i N_a \int\limits_0^{E_{d0}} \frac{\sigma(E_d)}{S(E_d)} \, dE_d \qquad (5.16)$$

where N_d is the number of incident deuterons, A is the atomic mass of e, f_m is the mass fraction of e in the material, f_i is the isotopic fraction, N_A is Avogadro's number, and E_{d0} is the incident deuteron energy. $\sigma(E_d)$ is the reaction cross section for isotope i and is obtained from either standard nuclear databases or dedicated experiments. $S(E_d)$ is the deuteron stopping power in the material and is calculated by codes such as SRIM [54] or Geant4 [87]. In practice, this expression is evaluated numerically by stepping the incident deuteron through the material and aggregating the particle yields for each reaction at each step. Materials that vary in composition or density as a function of depth can be handled similarly although the numerical integration is slightly more complex. The initial validation of these codes has shown excellent agreement with experimental measurements of particle yield [104].

The nuclear reaction model in Eq. 5.16 has been incorporated into ACROYNM by rewriting the internal Geant4 particle source module. After tracking a single deuteron through the magnetic fields, the yield is computed using the RFQ current, PFC surface composition, and nuclear cross section data to compute the yield of the particles of interest. The computed number of particles are then launched as secondary particles in Geant4 for tracking to the detectors. An example for the calculation of

---

[4]"Channel-based" simulation of nuclear reactions considers the energetically available reaction entrance channels and then uses continuous energy cross section data for each reaction to statistically select a reaction exit channel; "Parameterized" simulation uses mathematically models to correctly capture reaction dynamics over many events.
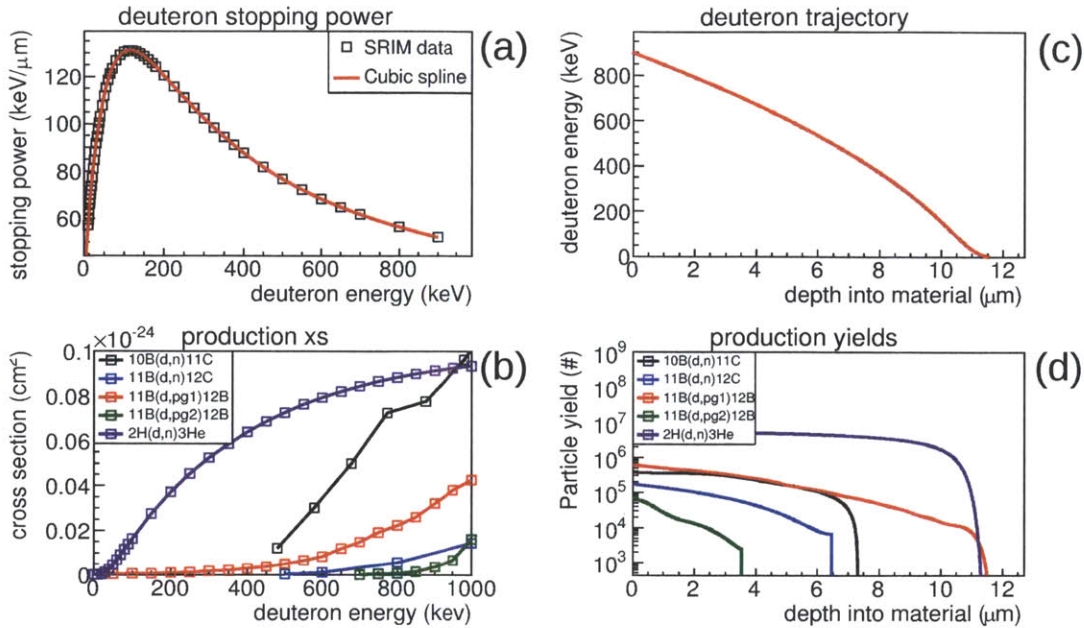
Figure 5-9: The neutron and gamma yield calculated by ACRONYM using Eq. 5.16 for 0.9 MeV deuterons incident upon a mixed deuterium-boron layer on a PFC surface: (a) A cubic spline on SRIM data provides a continuous stopping power curve for calculation; (b) The applicable deuterium and boron nuclear cross sections; (c) The slowing down of the deuteron in the deuterium-boron layer; (d) The step-wise particle yields for each accessible reaction.

the neutron and gamma yield from 0.9 MeV deuterons incident on a 15 μm thick deuterium-boron surface film is shown in Figure 5-9, assuming RFQ deuteron beam parameters of 2% duty cycle, 5 mA peak current, and 5 s of irradiation time.

5.3.2 Validation

Because ACRONYM played a central role in the design of AGNOSTIC and will play a central role in interpreting experimental data, a series of validation test were carried out to build confidence in the models of Alcator C-Mod and the neutron and gamma detectors. Two of the validation results are presented in the following sections.

Validation of geometry and transport

To validate the volume geometry, material composition, and particle transport in ACRONYM, a series of simulations was carried out in an attempt to replicate an experimental calibration of the Alcator C-Mod neutron diagnostic system (NDS). Due

(a) Experimental geometry

^{252}Cf source position	Experiment efficiency ($\times 10^{-8}$)	ACRONYM efficiency ($\times 10^{-8}$)
CT_AB	4.13	4.85
CT_BC	2.77	1.84
F	0.33	0.31

(b) Validation results
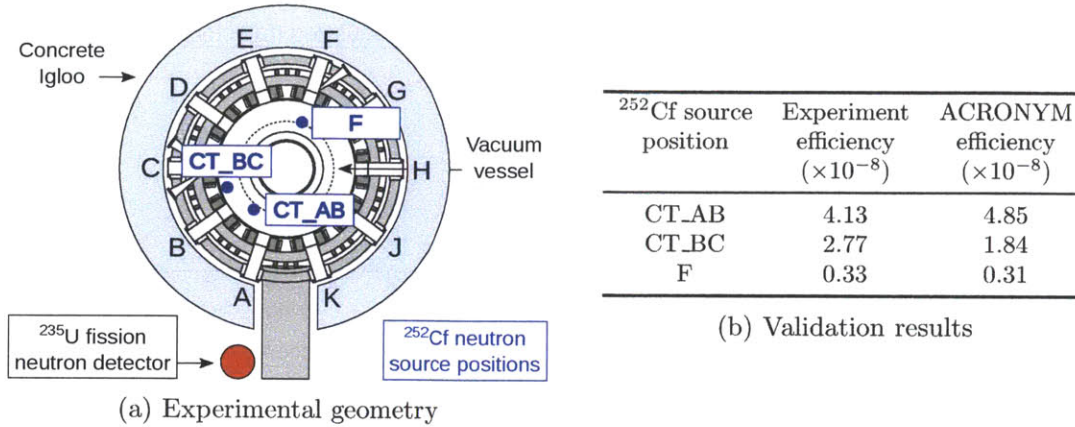
Figure 5-10: The (a) experimental setup for the neutron detector calibration experiments is shown on a top-down view of the Alcator C-Mod geometry. The validation results for each ^{252}Cf neutron source position are shown in (b), where the detector efficiency results are given in counts per ^{252}Cf source neutron. The lack of error bars on both efficiencies is explained in the text.

to the rigorous operation schedule and extremely high-activity radioactive sources required for sufficient detector statistics, the NDS calibration experiments provide one of the few closely controlled experiments against which these features of ACRONYM may be validated. Neutron transport, which requires data-driven channel-based models to achieve high precision results, is far more complex than charged particle or gamma transport, which are well described by parameterized models, making the NDS calibrations particularly useful as validation comparisons.

Composed of several types of thermal neutron detectors that are distributed in four neutron moderator stations within the experimental hall, the NDS is designed to measure the global fusion neutron production rate during plasma shots. Each detector must be calibrated before the start of each plasma campaign to account for all physical changes to the tokamak superstructure and surrounding equipment that may effect neutron transport. For the NDS calibration that was simulated for ACRONYM validation, a 66.5 μg ^{252}Cf neutron source was placed at various locations within the Alcator C-Mod vacuum vessel. The source remained in position until sufficient counting statistics were achieved on each detector. The count rate at each position can then be computed in units of detector counts per ^{252}Cf source neutron [102].

For implementation in ACRONYM, the coordinate locations of the chosen ^{235}U fission thermal neutron detector, described in Section 5.3, and three ^{252}Cf source positions were extracted from [106]. The validation simulation setup is presented in Figure 5-10a, which shows a top down view of Alcator C-Mod. Because higher resolution position data could not be obtained, there is some error associated with the location of the detector and sources. Neutron events were generated until the statistical error in the Monte Carlo calculations of efficiency were negligible compared to the

94

small nonstatistical error in the detector and source positions. Hence, the results of the validation, which are presented in Table 5-10b, are shown without the statistical error bars, which, in any case, are not given for the original calibration results in the literature. The key takeaway is, despite the high complexity of the problem, that the simulated results are in reasonable absolute agreement with the experimental results and very closely replicate the decreased count rate trend as the source is moved further from the detector.

Given the complexity of the problem, which spans the entire Alcator C-Mod superstructure, and the high statistics involved, the simulated detector efficiencies show very good agreement with the experimental efficiencies. The results confirm that the geometry and materials of Alcator C-Mod are well described in ACRONYM and that Geant4 is accurately modeling the transport of the $\lesssim 8$ MeV neutrons, which are produced by ^{252}Cf. Furthermore, the principle modeling domain of interest for AIMS is within the core of the device, where geometry will have significantly less effect on the simulation of the LaBr$_3$-SiAPD and EJ301-PMT detectors.

Detectors

To validate the models of the LaBr$_3$-SiAPD and EJ301-PMT detectors in ACRONYM, the physical detectors were exposed to a variety of neutron and gamma sources in the laboratory and then simulated under identical conditions.

Figure 5-11 shows one result from the validation work, in which the experimental response of both detectors to 0.662 MeV gammas from a ^{137}Cs check source was compared to simulation results from ACRONYM. For the LaBr$_3$-SiAPD detector, the shapes of all features of the gamma spectra are almost exactly replicated, including the Compton backscatter peak, Compton continuum, and photoabsorption peak. The matched spectra shapes indicate that the underlying gamma physics is handled correctly and that the scintillation photon production, transport, and detection is correctly modeling the detector resolution to a high degree. The positions of the Compton edge and the photoabsorption peak also occur in the correct place in energy, indicating that the experimental calibration procedure is correct.

Similarly, the simulated response of the EJ301-PMT detector matches the experimental response to better than a few percent over almost the entire spectrum; the slight deviation from the experimental spectra at the lowest energy is attributed to downscattered gammas from ambient physical geometry that were not modeled in the simulations. The close match between the smeared "edge" centered 0.478 MeVee indicates that ACRONYM is correctly simulated the detector resolution using the new model for scintillation described in Section 5.2
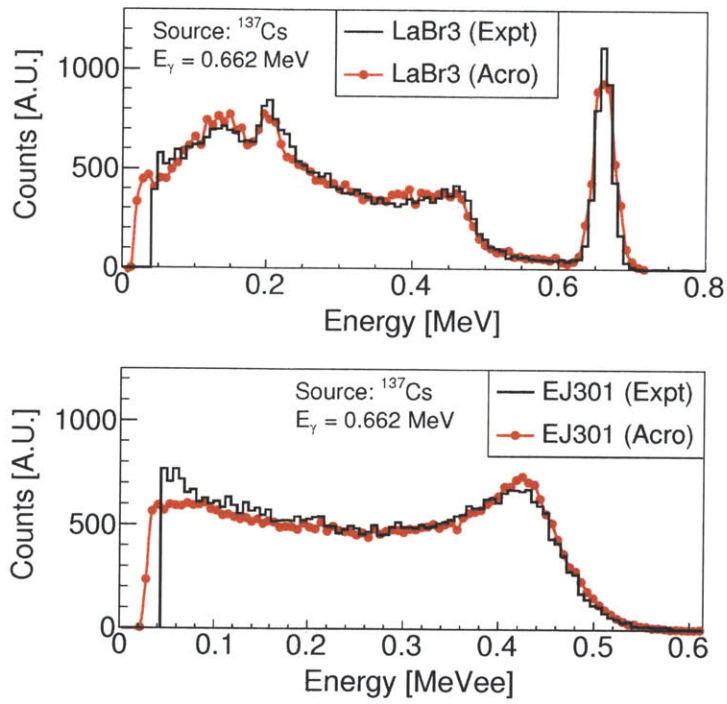
Figure 5-11: Comparisons between the experimental (Expt) and ACRONYM (Acro) simulated responses to 0.662 MeV gammas for the LaBr$_3$-SiAPD detector (top) and EJ301-PMT detector (bottom) that were used in AGNOSTIC.
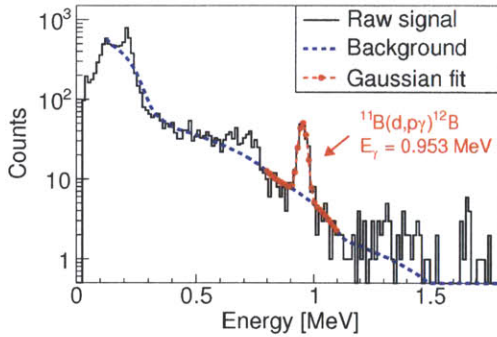
(a) Simulated LaBr$_3$-SiAPD gamma spectrum in AGNOSTIC
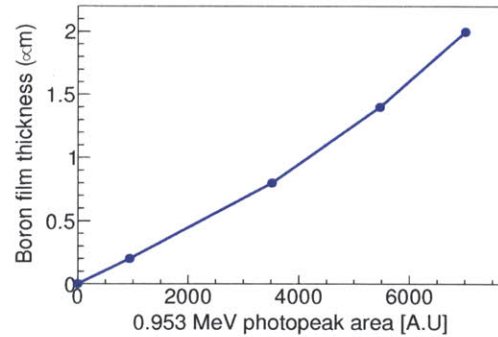
(b) Simulated peak area-boron thickness correlation curve.

Figure 5-12: An ACRONYM measurement of a pure boron film on a molybdenum PFC surface in Alcator C-Mod. (a) A fitted photoabsorption peak at 0.953 MeV in the LaBr$_3$-SiAPD spectrum can be used to quantify the boron on the PFC surface. (b) The simulated correlation between 0.953 MeV peak area and the boron layer thickness links experimentally determined peak area with boron layer thickness.

5.3.3 Simulation of AIMS measurements

As an example of ACRONYM's capabilities, Figure 5-12a shows the simulated LaBr$_3$-SiAPD gamma detector response for the simulated AIMS measurement of a molybdenum PFC in the Alcator C-Mod lower divertor. AIMS is insensitive to the bulk molybdenum because the $\sim$MeV deuteron beam is not sufficiently energetic to produce nuclear reactions in high-Z metals. A 1 μm thick layer of pure boron was specified on the PFC surface. The large scattering background that dominates the response comes from deuteron-induced gammas that downscattered from the ambient geometry into the detector; however, despite the large background, the resolvable photoabsorption peak at 0.953 MeV from the ^{11}B(d,pγ)^{12}B reaction confirms that the LaBr$_3$-SiAPD detector can identify the presence of boron on the surface. A integral of a fitted gaussian to the photoabsorption peak, combined with the deuteron beam current, can be used to quantify the boron thickness under different assumptions about the surface composition.

Figure 5-12b shows the correlation between the simulated change in photopeak area and the change in thickness of an assumed pure boron layer on the PFC surface. For measurement of the erosion and redeposition of boron on the PFC surface of Alcator C-Mod, for example, this simulated calibration curve can be used to interpret the experimentally acquired data, in which the known 0.953 MeV photoabsorption peak area can be used to extract the absolute thickness of the boron layer from the correlation curves.

Chapter 6

Experimental validation activities

An AIMS diagnostic such as AGNOSTIC is a complex system, involving an RFQ accelerator, beam transport system, multiple types of scintillation, detectors, a data acquisition system, and other complementary hardware (RFQ high voltage and RF racks, permanent magnetic quadrupoles for beam focusing, detector preamplifiers and amplifiers for signal preprocessing). Before installing such a system on an even more complex system like Alcator C-Mod, it was critical to validate the individual performance of each component and the system performance of all components in a controlled laboratory setting. Once installed on Alcator C-Mod, it was important to attempt to replicate the validation results achieved in the more ideal *ex-situ* laboratory setup.

The purpose of this chapter is to present experimental work carried out *ex-situ* in an accelerator facility and *in-situ* on the Alcator C-Mod tokamak to validate the ability of AGNOSTIC to perform AIMS measurements of PFC surface composition. The work focused on ensuring the ability of all the subcomponents of AGNOSTIC to work correctly together and on acquiring neutron and detector spectra that contained resolvable features for the identification and quantification of isotopes on the PFC surfaces.

6.1 Ex-situ validation

Before AGNOSTIC was installed on Alcator C-Mod, a series of mock AIMS measurements were performed in an *ex-situ* accelerator facility. The primary purpose of the experiments was to verify the performance of each critical subcomponents of AGNOSTIC - the RFQ accelerator, detectors, data acquisition (DAQ) system, and data analysis, which are described in Chapter 4 - and validate the ability of the entire diagnostic system to function together as designed. While it would have been optimal to perform more detailed analysis of PFC surfaces under controlled laboratory
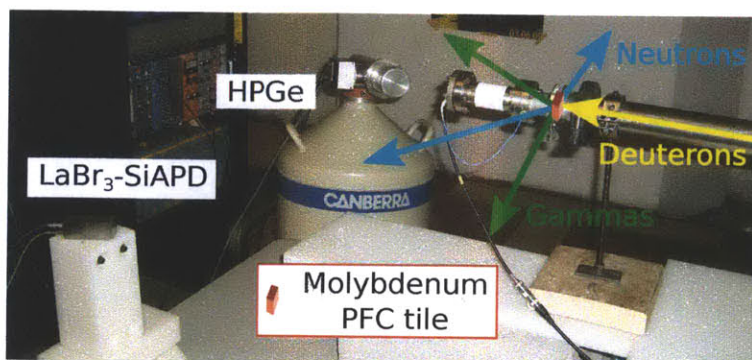
Figure 6-1: Photograph of the experimental setup in the NW13 shielded vault for validating the AGNOSTIC systems before installation on Alcator C-Mod.

conditions, the rigid schedule for installation of AGNOSTIC on Alcator C-Mod did not provide sufficient flexibility to do so.

After moving all AGNOSTIC components into the RFQ cell, an optical imaging experiment was carried out to ensure that the RFQ deuteron beam was focused and centered in the beamline. The primary purpose of these tests was to ensure that an optimized beam would be injected into the Alcator C-Mod vacuum vessel.

6.1.1 NW13 vault experiments

The experiments were performed in the MIT NW13 shielded vault , which measures 5.7×9.8 m in floor dimensions, 4.0 m in height, and has ~1 m thick concrete walls for radiation shielding. The experimental geometry is shown in Figure 6-1 The RFQ accelerator was located in an adjacent room with the beamline penetrating the thick concrete walls through a small circular opening. Near the end of the beamline, a small chamber was installed to hold various test samples for irradiation, with the beamline terminating in a Faraday cup to measure the amount of beam current that missed the target. Several detectors were set up at various locations surrounding the target to measure the deuteron-induced neutrons and gammas produced during target irradiation: the LaBr$_3$-SiAPD detector from AGNOSTIC; a high purity germanium (HPGe) detector for its excellent gamma energy resolution; and two NaI-PMT detectors for additional gamma detection. The EJ301-PMT detector that was used in AGNOS-TIC on Alcator C-Mod had not been assembled at this time and was unavailable for neutron detection. The LaBr$_3$-SiAPD and HPGe detectors are shown in position in Figure 6-1.

After successful tests of the individual subcomponents, a variety of targets were inserted into the beamline and irradiated with the RFQ deuteron beam to measure the induced gamma spectra. Targets included a small graphite block, a copper mesh filled with pure boron granules, and several PFC tiles that had been extracted from Alcator
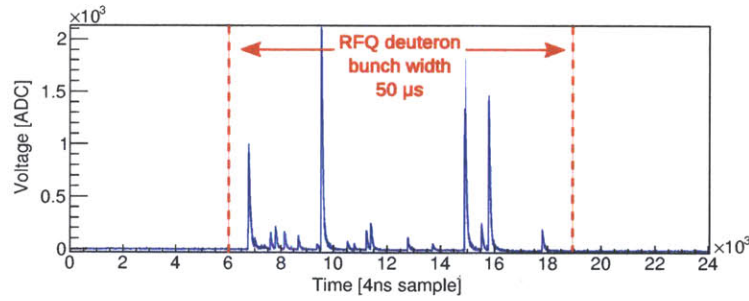
(a) RFQ deuteron beam pulse-induced detector events
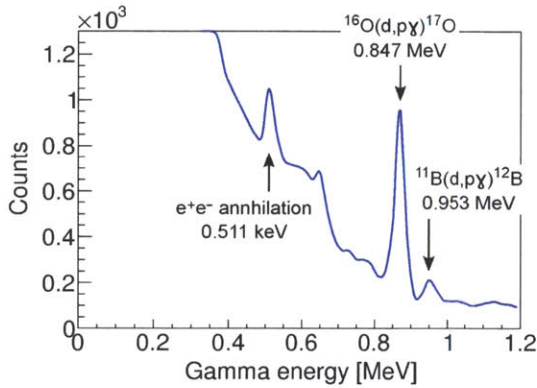
(b) Alcator C-Mod molybdenum PFC tile
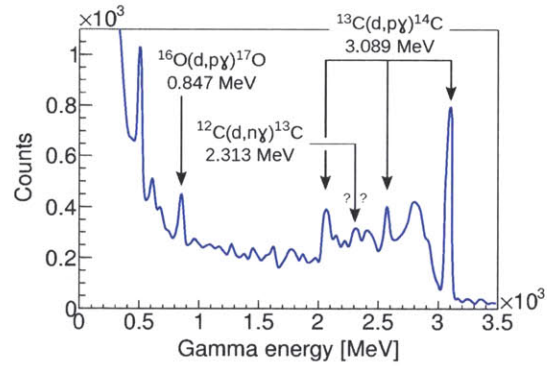
(c) Graphite tile

Figure 6-2: Selected results from the NW13 validation experiments. (a) The appearance of detector pulses only during RFQ accelerator pulses confirms detection of deuteron-induced nuclear reactions and verifies the triggered operation of the DAQ. (b) A gamma spectrum from the $LaBr_3$-SiAPD detector shows the detection of boron on an Alcator C-Mod PFC tile. (c) A gamma spectrum from the HPGe detector shows the detection of carbon and oxygen on a graphite tile.

C-Mod after a recent plasma campaign. The DAQ was triggered by a timing pulse from the RFQ plasma source in order to save digitized waveforms only during the RFQ deuteron beam pulse. Triggering during the RFQ pulse reduces the radioactive background and amount of stored data by a factor of the RFQ duty cycle.

Figure 6-2 contains selected results from the validation experiments. One of the first validation tests performed was to ensure that the gammas from deuteron-induced nuclear reactions could be correctly acquired using the DAQ triggering method described above. Figure 6-2a shows substantial detector counts rates only during the time when the RFQ accelerator is pulsing its 50 μs deuteron beam into the target and zero waveforms outside the pulse. This confirms that the DAQ triggering is correctly acquiring prompt deuteron-induced gammas only from RFQ beam pulses.

The next experiments were to acquire spectra for different targets to confirm the measurement of the nuclear reaction gamma of interest. Figure 6-2b shows a gamma spectrum acquired by the $LaBr_3$-SiAPD detector for an Alcator C-Mod molybdenum PFC tile that has a visible boron film on the surface. Three distinct peaks in the spectra are immediately evident. The 0.511 MeV peak is the annihilation peak, corresponding to the detection of gammas produced when high energy gammas ($\gtrsim 2$ MeV) induce pair production in material close to the detector. The 0.871 MeV peak is a result of the $^{16}O(d, p\gamma)^{17}O$ reaction, confirming the ability to detect and quantify oxygen. The oxygen is present due to exposure of the boron films to atmospheric conditions; the peak gradually disappears as the PFC tile outgasses over time under high vacuum conditions. The 0.953 MeV peak corresponds to gammas from the $^{11}B(d, p\gamma)^{12}B$ reaction, which confirms the ability to detect and quantify boron on PFC surfaces.

Similarly, Figure 6-2c shows a gamma spectrum acquired by the HPGe detector for the graphite tile target. The 0.511 McV annihilation peak is visible at the lowest energies. The peak at 0.847 MeV is caused by gammas from the $^{16}O(d, p\gamma)^{17}O$ reaction, confirming the ability to detector and quantify oxygen. An important consideration is that the gammas from oxygen (0.847 MeV) may overlap the 0.847 McV gammas produced by the $^{56}Fe(n, n'\gamma)^{56}Fe$ reaction, where the incident neutrons come from competing neutron-production reactions induced by the deuteron beam. In more iron-dense scattering environments, such as the tokamak, the 0.847 McV and 0.871 MeV peaks may be unresolvable with the gamma detectors used in AGNOSTIC. This may lead to complications in AIMS where the detection of oxygen must be performed in high energy neutron fields.

Three peaks correspond to the $^{13}C(d, p\gamma)^{14}C$ reaction, the high energy photoabsorption peak at 3.089 McV and the first (2.578 McV) and second (2.067 McV) escape peaks. While the statistics are too low to confirm unequivocal detection, a small peak appears at 2.3 MeV that could correspond to the 2.313 MeV gamma from the $^{12}C(d, p\gamma)^{13}C$ reaction. This would confirm the ability to differentiate carbon isotopes, which, as discussed in Chapter 3, would enable the study of plasma boundary transport of impurities with isotopically tailored impurity gas puffing. Finally, a number of other small peaks in the spectrum, such as the peaks at 0.569 MeV and 0.596 McV, correspond to fast neutron interactions with the HPGe crystal itself.

6.1.2 RFQ beam imaging

As the final step before attaching the RFQ to the Alcator C-Mod vacuum system, the RFQ beam optimization was validated using a specially constructed optical imaging beamline. The beamline was installed after the focusing permanent magnetic quadrupoles and consisted of a short section of beam pipe terminating in a 2-3/4 inch flange with a gold-plated quartz window, on which the impinging deuteron beam generates visible scintillation light. A 45 degree mirror in front of the window was used
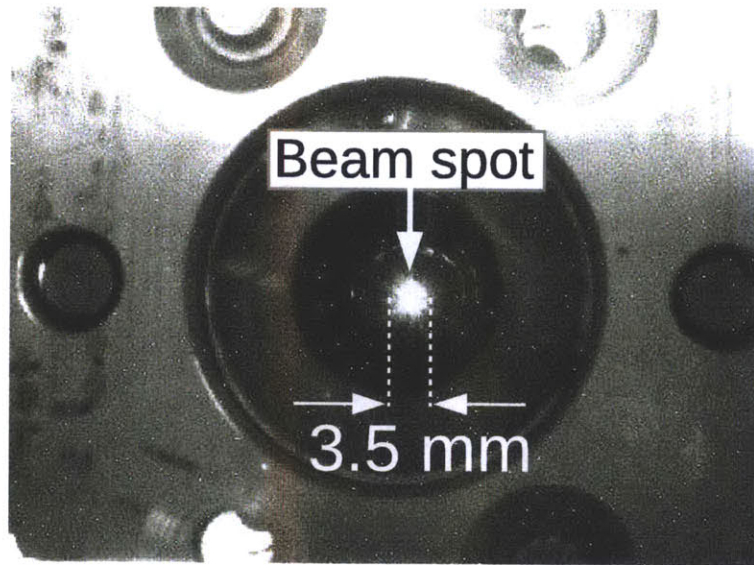
Figure 6-3: A CCD camera image of the optimized RFQ deuteron beam imping-
ing on a 2-3/4 inch gold-plated quartz window flange after the permanent magnet
quadrupoles. The visible beam spot is approximately 1-sigma of the 2D gaussian
beam distribution, showing that an optimally focused beam enters the Alcator C-
Mod vacuum vessel.

to reflect the light out of the confined diagnostic port space and into a CCD camera
for imaging.

An image of the 2-3/4 inch flange face, showing the optimized deuteron beam scin-
tillating on the window, is shown in Figure 6-3. Image analysis with background
subtraction showed the 1-sigma width of the gaussian beam to be approximately
4 mm. Because the injection aperture was approximately 12 mm, the results demon-
strate that more than 99% of the beam enters the Alcator C-Mod vacuum vessel and
confirm that an optimized arrangement of the RFQ and focusing permanent mag-
netic quadrupole system was achieved. The details of the RFQ accelerator alignment
procedure, beamline hardware, and optimization method can be found in [55].

6.2 In-situ validation

AGNOSTIC was successfully installed on Alcator C-Mod during late July of 2012, as
shown in the several photographs contained in Figure 6-4. Similar to the procedure
performed in the NW13 vault, the RFQ accelerator, detectors, DAQ, and supporting
hardware were each separately tested before integrated tests of AGNOSTIC were
performed. The principle purpose of the *in-situ* validation tests was to confirm the
ability of AGNOSTIC to acquire sufficiently resolved neutron and gamma spectra that

(a) Craning in the RFQ
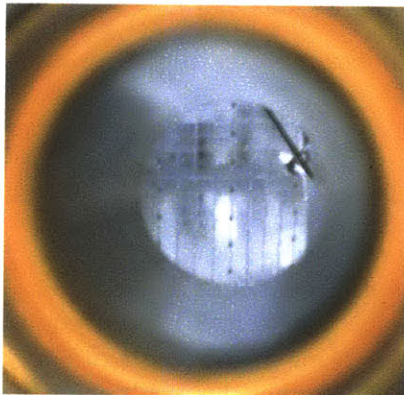
(b) View down the beamline
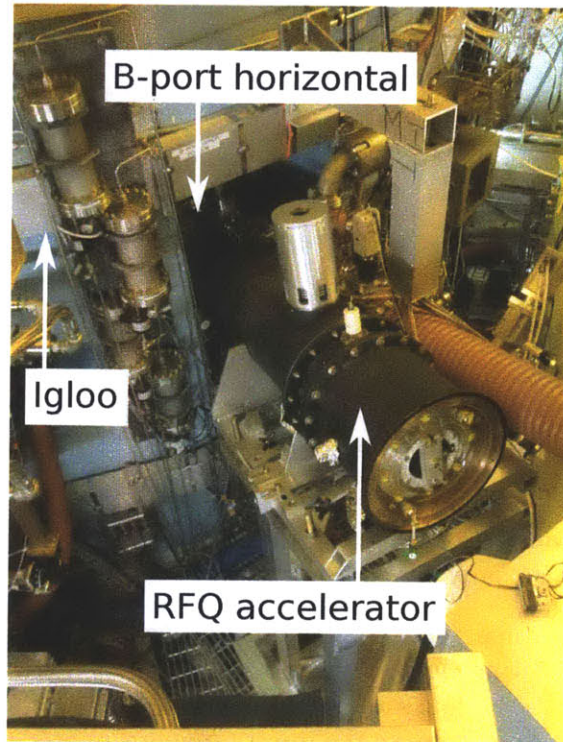
(c) Installation at B-port

Figure 6-4: Photographs taken during the installation of AGNOSTIC on Alcator C-Mod. (a) The RFQ is craned into the experimental hall. (b) Inner column PFC tiles are visible through the RFQ beamline. (c) The RFQ installed at B-port horizontal diagnostic port, where it fits tightly into a gap in the concrete radiation shielding igloo and between 5 other major plasma diagnostics at B-port horizontal.

would enable quantification of PFC surface compositions within hostile Alcator C-Mod environment. A secondary purpose was to validate the magnetic beam steering in order to demonstrate the capability of making measurements at different locations on the PFC surface.

6.2.1 Triggering and prompt detection

To confirm that the beam was correctly entering the vacuum vessel and inducing prompt gammas and neutrons that were measured by the detectors, the RFQ injected 50 μs pulses of deuterons into the vacuum vessel at 100 Hz. The injected current of deuterons was measured with the transformer at the end of the RFQ beamline, adjacent to the isolation gate valve on the Alcator C-Mod port flange. No steering tokamak magnetic fields were used, causing the straight trajectory beam to impinge upon a PFC surface on the inner wall, as shown in Figure 8-2c. A timing signal was split from the RFQ plasma source to trigger a 60μs digital window on the data acquisition system; detector and RFQ data are only stored during triggered windows of fixed width, which is crucial for minimizing radiation background on the detectors and minimizing the amount of stored digital data.

Detector and RFQ current signals during a single digital window are shown in Figure 6-5 Although the current rise time is somewhat slow, the RFQ consistently generates a steady-state ~40 μs pulse of deuterons, which can be integrated in post-processing to determine the total number of deuterons injected into the vacuum vessel. The LaBr$_3$-SiAPD and EJ301-PMT signals only show pulses during the RFQ current pulse, indicating that the neutrons and gammas being detected are prompt deuteron-induced nuclear reaction products. Because visual diagnosis showed the beam to be centered on the injection axis and away from the isolation gate valve, the neutrons and gammas must originate from the central column PFC tiles. Confirmation of this was achieved by closing the gate valve and confirming that the detector signals vanish as expected since the 0.9 MeV deuteron beam is not energetic enough to induce nuclear reactions with steel. Finally, the digitized detector waveforms show very little noise and essentially zero pulse pileup. The pulses can be operated on with real-time or offline digital pulse processing in order to produce high resolution energy spectra that facilitate the reconstruction of PFCs surface conditions.

6.2.2 LaBr3-SiAPD isotope identification

To validate the isotope detection capability of the LaBr$_3$-SiAPD detector in Alcator C-Mod, the deuteron beam was directed with zero magnetic steering field to a single PFC location on the inner wall and digital waveforms were acquired, which were processed offline into a gamma spectrum; Figure 6-6 shows the calculated gamma spectrum. The spectrum is primarily composed of a large background due to the unavoidable Compton scattering of gammas off the dense structure of the tokamak before entering
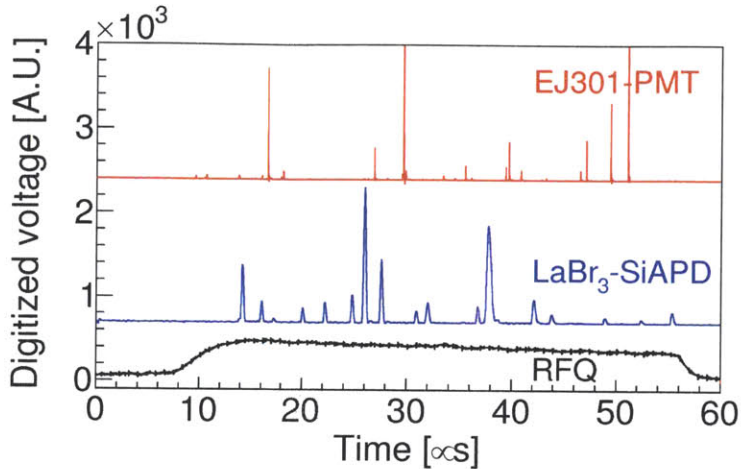
Figure 6-5: A 60 μs data acquisition window is triggered at $t = 0$ by a timing pulse from the RFQ at 100 Hz. The 50 μs RFQ deuteron pulse (bottom trace) induces nuclear reactions on a PFC. The LaBr$_3$-SiAPD (middle trace) and EJ301-PMT (top trace) detectors measure prompt gamma and neutrons, respectively.

the detector. While the background is substantial, four discrete gamma peaks are statistically significant above the background, which show close similarities to the same experiment that was performed *ex-situ* and is described above in Section 6.1.

The 0.511 MeV peak results when positron annihilation gammas from ambient material are detected. The positrons are a result of high energy gammas ($\gtrsim 2$ MeV) inducing pair production in material near the detector. The 0.662 MeV peak is caused by a cesium-137 check source that is intentionally attached to the detector for in-situ calibration during RFQ operations. The 0.847 MeV peak results from inelastic neutron scattering off the significant amount of steel in the vacuum components of Alcator C-Mod via the reaction $^{56}\text{Fe}(n, n'\gamma)^{56}\text{Fe}$. Finally, for the purposes of diagnosing PMI, the most important peak is the 0.953 MeV peak that is produced by unscattered gammas from the $^{11}\text{B}(d, p\gamma)^{12}\text{B}$ reaction. The area of the peak, calculated by integrating a gaussian fit to the peak after subtracting a calculated background spectrum, can be used in conjunction with the beam and detector parameters to quantify boron on the PFC surface. Boron is expected to be present in significant quantities ($\sim$micron-thick layers) on Alcator C-Mod tiles due to the use of "boronizations" to enhance plasma performance.

6.2.3 EJ301-PMT deuterium identification

To validate the ability of the EJ301-PMT detector to measure retained deuterium on the PFC surfaces, the deuteron beam was directed with zero magnetic steering field to a single PFC location on the inner wall and digital waveforms were acquired,
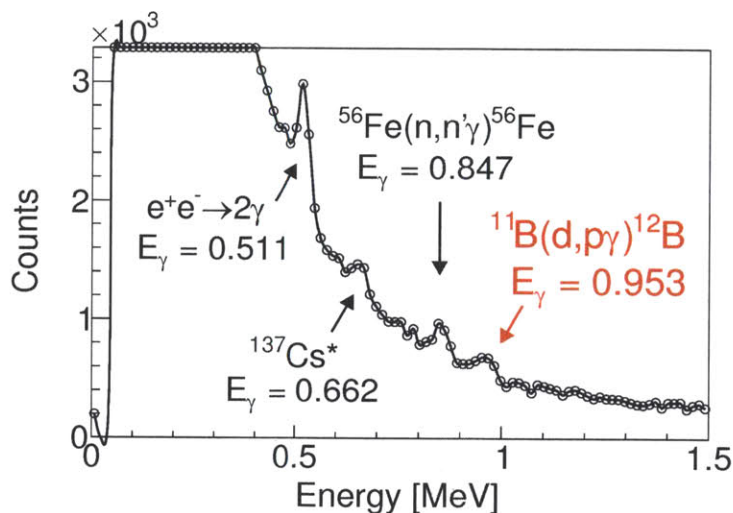
Figure 6-6: A peak at 0.953 MeV in the experimental LaBr$_3$-SiAPD detector spectrum confirms the ability to observe boron on an inner wall PFC.

which were processed offline into a neutron spectrum.

Figure 6-7A shows the experimental EJ301-PMT detector neutron spectrum. Gamma-induced events are excluded from the spectrum using digital PSD with a minimum discrimination accuracy of approximately 99.87% at 0.34 MeVee, the energy deposited by 0.511 MeV gammas in the detector and the lowest energies of interest for AIMS measurements. With zero magnetic steering fields, the angle between the beam and the detector was fixed at 157 degrees. For an incident deuteron beam of 0.9 MeV, Eq. 3.6 predicts that unscattered neutrons from the ^{2}H(d, n)^{3}He reactions will have a kinetic energy of 1.86 MeV for 0.9 MeV deuterons. The neutron kinetic energy will increase for reactions that are induced by lower energy deuterons that have slowed in the material. The neutrons will appear in the EJ301-PMT spectrum at 0.41 MeVee (for reactions at the surface) and 0.56 MeVee (for reactions at the end of the deuterons range) in the EJ301-PMT detector response. Thus, because of the EJ301-PMT detector response to monoenergetic particles, the neutron detector spectrum should show a smeared high energy edge in this energy region due to the presence of retained deuterium on the PFC surface; in Figure 6-7, this region is shaded.

The EJ301-PMT energy spectrum in Figure 6-7A indeed shows a small, smeared high energy edge at approximately 0.41 MeVee. The edge sits on top of a large, smooth background caused by the downscattering of high energy neutrons from the ^{10}B(d, n)^{11}C (Q = 6.464 MeV) and ^{11}B(d, n)^{12}C (Q = 13.7 MeV) reactions. For the measurement of deuterium, the neutrons from the boron reactions represent an unavoidable background from which the identification and quantification of deuterium must be extracted with careful analysis.

A more rigorous confirmation is shown in Figure 6-7B where the absolute value of
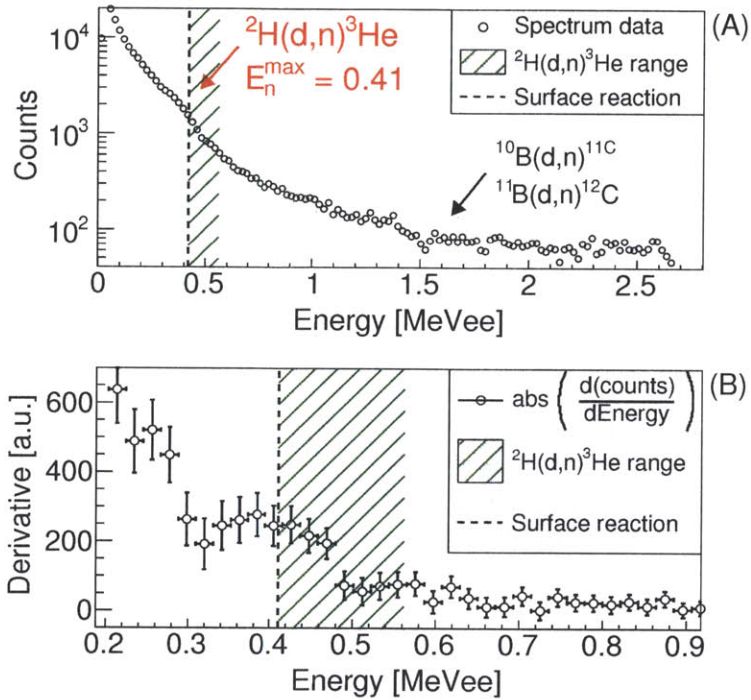
Figure 6-7: (A) The smeared high energy edge at 0.41 MeVee in the experimental EJ301-PMT detector response demonstrates the detection of retained deuterium on an inner wall PFC. The deuterium signal sits on a large neutron scattering background caused by deuteron reactions with boron. (B) The absolute value of the spectrum derivative confirms the detection of unscattered monoenergetic ^{2}H(d, n)^{3}He neutrons. The nuclear kinematics indicate that the neutrons originate from the PFC surface.

Table 6.1: The nuclear kinematic predictions for where in the EJ301-PMT detector response unscattered neutrons from the ^{2}H(d, n)^{3}He reactions should appear for the three different beam-detector angles shown in Figure 6-8.

Toroidal field B_ϕ (T)	Beam angle θ (^{o})	$E_{neutron}$ (MeV)	Detector edge (MeVee)
0.00	157	1.86	0.41
0.05	143	1.93	0.45
0.17	124	2.13	0.52

the energy spectrum derivative is taken in the region of interest. As discussed in Chapter 4, the absolute value of the derivative of the EJ301-PMT energy spectrum will show peaks centered on the energy of incident monoenergetic neutrons. It is evident that there is a statistically significant peak centered very close to 0.41 MeVee, which is defined by the seven consecutive, statistically significant points that deviate from the smooth background spectrum. The peak is indicative of the detection of monoenergetic neutrons from the ^{2}H(d, n)^{3}He reaction.

6.2.4   Magnetic steering and localized measurements

Validation of the magnetic beam steering was performed by exploiting the angular dependence of the ejectile neutron kinetic energy given in Eq. 3.6. Due to present limitations imposed by the magnet power supply, the toroidal field coils of Alcator C-Mod can provide steady-state toroidal magnetic fields between 0.0 and 0.17 T, sufficient to change the angle θ between the incident deuterons and ejectile neutrons by almost 35 degrees, which corresponds to a $\sim$30 cm vertical displacement of the beam impact location. The total corresponding neutron kinetic energy shift is approximately 0.25 MeV, as shown in Table 6.1. Therefore, as the magnetic fields are increased to change the angle, the nuclear kinematics predict that the peak in the EJ301-PMT detector response derivative will shift to higher energy in response to the higher neutron kinetic energy.

The deuteron beam was steered to three fixed locations and neutron spectra were acquired with the EJ301-PMT detector in order to look for the peak shift in neutrons from the ^{2}H(d, n)^{3}He reaction, which also serves as a secondary confirmation of the detection of deuterium. While, in principle, the higher energy neutrons from the ^{10}B(d, n)^{11}C and ^{11}B(d, n)^{12}C reactions would provide more discernible edges, the gain of the EJ301-PMT detector - optimized for the detection of deuterium - caused the neutron-induced pulses from boron to saturate the digitizers of the DAQ and prevented analysis in the high energy region of the spectra.

The absolute value of the derivative of the EJ301-PMT spectra at three different angles appear in Figure 6-8. The shaded vertical bars represent the predicted peak energy of neutrons from ^{2}H(d, n)^{3}He surface reactions at three incident deuteron-
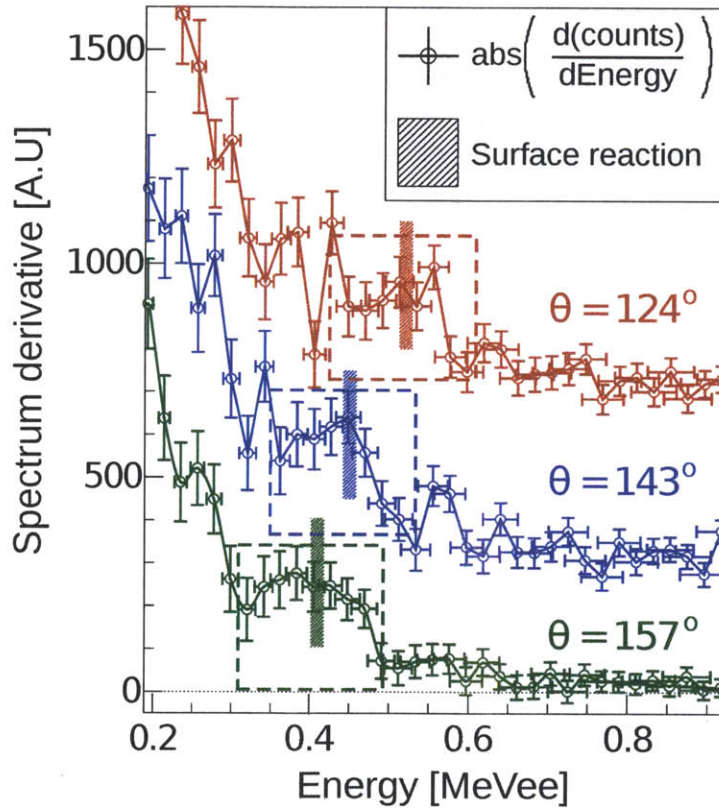
Figure 6-8: EJ301-PMT detector spectrum derivatives for increasing angles between the deuteron beam and ejectile neutron. The ^{2}H(d, n)^{3}He peak is defined by 7 consecutive, statistically significant points that deviate from the scattering background trend. The peak clearly follows the predicted energy shift for surface reactions from nuclear kinematic theory.

ejectile neutron angles: 124°, 143°, 157°. Despite some scatter at lower energies, the key feature - the seven statistically significant, adjacent points that deviate from the scattering background to form the peak - clearly shift higher in energy as the angle changes in close agreement with the kinematic predictions. The degradation in the peak structure with increasing angle is expected from the effects of steering a high current charged particle beam in magnetic field, which results in a larger beam spot size on the PFCs [85, 86].

The results demonstrate two key points. First, the beam dynamics codes, which were used to calculate the angles between the incident deuterons and ejectile neutrons as inputs to the nuclear kinematic predictions shown in Figure 6-8, correctly simulate the trajectory of the beam in the magnetic steering fields and the impact location on the PFCs. Second, the three measurements of deuterium show the feasibility of providing spatially resolved maps of isotopic content across a large surface area of PFCs, confirming the ability of steering the deuteron beam with the tokamak magnetic fields.

6.3 Extracting PFC surface information from the detector spectra

Gamma spectrum analysis

In AIMS, quantification of erosion/redeposition and material mixing is primarily obtained from the $LaBr_3$-SiAPD gamma energy spectra since the involved isotopes have strong gamma production cross sections with the incident 1 MeV deuterons from the RFQ accelerator. The analysis of gamma energy spectra with scintillators is extremely straightforward due to the presence of the photoabsorption peaks caused by full energy deposition of the gamma within the scintillator [53]. Combined with knowledge of the detector absolute efficiency and nuclear reaction parameters, integration of the photoabsorption peaks following a treatment of the background can provide absolute quantification of the isotopes within the surface a material. IBA materials analysis via gamma spectroscopy is a mature field [41].

An example analysis, using the 0.953 MeV gamma from the $^{11}B(d, p\gamma)^{12}B$ reaction, is shown in Figure 6-9. For AIMS, the gamma background - caused by ambient radioactive decay, downscattered gammas, or detector effects - is calculated with the Sensitive Nonlinear Iterative Peak-clipping (SNIP) algorithm, a widely used, statistically robust treatment of background and peak finding in gamma spectra [107, 108]. The SNIP algorithm is applied to the gamma spectra in Figure 6-9 with the result plotting in red; The result is a clear delineation between the background and the 0.953 MeV photopeak from the $^{11}B(d, p\gamma)^{12}B$ reaction, which can be integrated to provide quantification of the boron on the PFC surface.

111
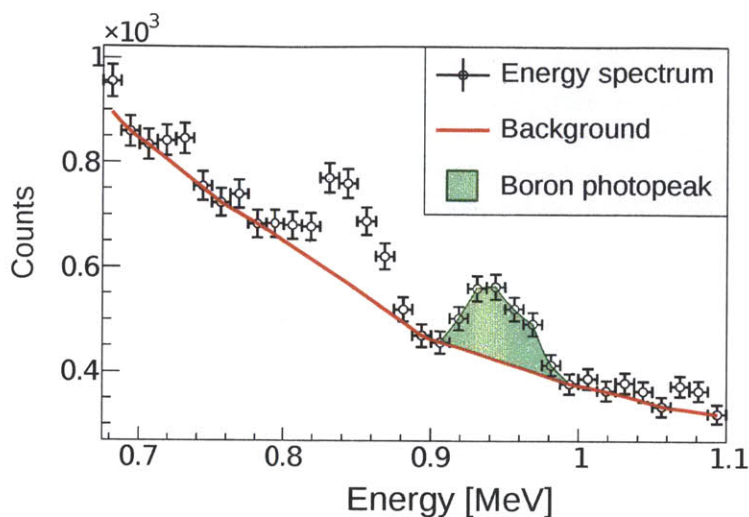
Figure 6-9: PFC surface isotopes with gamma production cross sections can be quantified in AIMS by analyzing the photopeak in the $LaBr_3$-SiAPD energy spectrum. Here, an integral above the calculated background for the 0.953 MeV photopeak from $^{11}B(d, p\gamma)^{12}B$ reaction can be used with the measurement parameters to quantify the boron on the PFC surface.

Neutron spectrum analysis

In AIMS, quantification of the retained deuterium on the PFC surface is obtained by analyzing the EJ301-PMT detector response. As usual, gammas must first be filtered out of the response with digital PSD. For the EJ301-PMT detector, PSD has a lower threshold for effectiveness of approximately 0.150 MeVee. As discussed above, neutrons from the induced $^2H(d, n)^3He$ reaction appear as a scattering continuum in the lower portion of EJ301-PMT spectrum superimposed on top of a large scattering background from competing neutron-production reactions. A smeared edge at the most energetic terminus of the scattering continuum - caused by neutrons elastically scattering off hydrogen in the scintillator with a scattering angle of 180° - can be predicted with nuclear kinematics and used to identify the isotope target involved in the reaction.

The analysis process is depicted visually in Figure 6-10, which shows an EJ301-PMT neutron spectrum acquired from an AIMS measurement of an inner wall PMT with zero magnetic steering field. The dominant feature in the spectrum is the large scattering background caused by incident deuterons on boron surface film via the $^{10}B(d, n)^{11}C$ and $^{11}B(d, n)^{12}C$ reactions. Both reactions have a high Q value (6.464 MeV and 13.732 MeV, respectively) and produce neutrons at significantly higher energy than the $^2H(d, n)^3He$ reaction. These deuteron-boron neutrons downscatter on the Alcator C-Mod superstructure before reaching the EJ301-PMT detector, leading to the large continuum that spans the entire spectrum energy range.

112
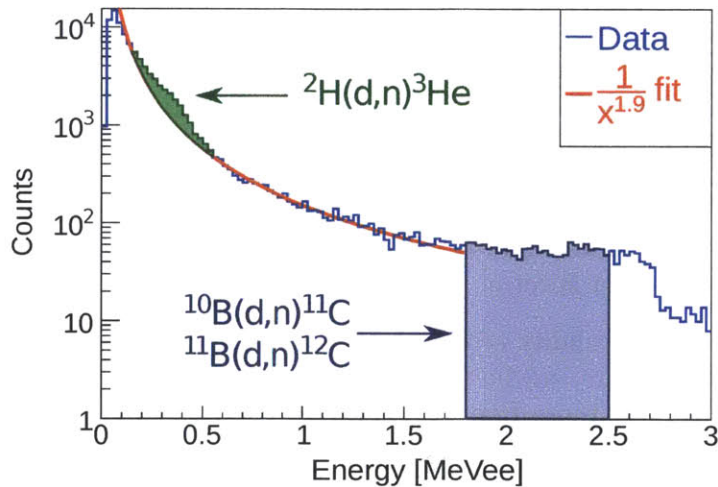
Figure 6-10: Deuterium and boron can be quantified from the EJ301-PMT neutron energy spectrum. An $x^{-1.9}$ function is fit to the large scattering background; an integral over the neutron energy range from the $^2\mathrm{H}(\mathrm{d,n})^3\mathrm{He}$ reaction then measures deuterium. An integral over an arbitrary range at high energy is proportional to the total amount of boron since only neutrons from the $^{10}\mathrm{B}(\mathrm{d,n})^{11}\mathrm{C}$ and $^{11}\mathrm{B}(\mathrm{d,n})^{12}\mathrm{C}$ are energetic enough to exist in this region.

Although the deuteron-boron continuum represents a background that must be carefully handled in the analysis, it does provide a significant benefit. Because Alcator C-Mod is a carefully controlled high vacuum environment,there are no other known isotopes on the PFC surfaces in sufficient quantities to produce neutrons above approximately 0.5 MeVee in the detector spectrum. Therefore, integrating the neutron spectrum at sufficiently high energy provides a quantitative but relative measure of boron. The integration limits are arbitrary - provided they are above the neutron energy from the $^2\mathrm{H}(\mathrm{d,n})^3\mathrm{He}$ neutrons, approximately 0.5 MeVee - but must remain fixed for successive measurements since only the *relative change* in boron surface concentration can be quantitatively compared at present with AGNOSTIC rather than an absolute measure. The integration region used in the analysis presented in this chapter is shown in dark blue in Figure 6-10 and covers 1.8 to 2.5 MeVee.

In order to integrate only neutrons from the $^2\mathrm{H}(\mathrm{d,n})^3\mathrm{He}$ reaction, the deuteron-boron neutron background must be quantified and removed from the EJ301-PMT spectrum. In the absence of a known physical form, an $x^{-1.9}$ functional form was chosen and fit to the scattering background between 0.5 and 1.8 MeVee. There is nothing special nor physically significant about the $x^{-1.9}$ function; it simply provides a good fit to the background and, when extrapolated to low energy, provides a clear delineation between neutrons from the deuteron-boron background (below the fit) and neutrons from the $^2\mathrm{H}(\mathrm{d,n})^3\mathrm{He}$ reaction (above the fit). Thus, an integral of the EJ301-PMT spectrum above the fit provides a quantitative measure of induced neutrons from deuterium on the PFC surface; this integral is shown in dark green in Figure 6-10. At

113

present, only the relative changes in deuterium concentration from measurement to measurement can be obtained with the diagnostic; future improvements in the data analysis techniques are expected to provide absolute deuterium concentrations. Nevertheless, the present analysis provides an excellent relative measure of the change in deuterium during successive measurements since the background fit establishes a constant baseline above which deuteron-deuterium neutrons can be quantified independent of changes to the deuteron-boron background. Thus, relative changes in the boron and deuterium content on the PFC surface can be independently obtained from the EJ301-PMT detector spectra.

A sanity check on the validity of extracting measurements of deuterium and boron from EJ301-PMT spectra can be made by comparing the flux of neutrons from the ^{2}H(d, n)^{3}He reaction to those from the ^{10}B(d, n)^{11}C and ^{11}B(d, n)^{12}C reactions. For this calculation, a randomly chosen EJ301-PMT neutron spectrum from an AIMS measurement was used. Deuterium neutron counts are achieved by integrating the spectrum from 0.2 to 0.55 MeVee above the background fit; boron neutron counts are achieved by integrating the spectrum over the same range and subtracting the deuterium neutron counts. The detector efficiency is identical due to integration over the same incident neutron energy range. The result is 7608 ± 248 deuterium neutrons and 26922 ± 310 boron neutrons, which provides a ratio of $\sim$0.3. To zeroth order, the ratio of the deuterium-to-boron neutron fluxes over this energy range weighted by the elemental cross sections provide a crude estimate of the deuterium-boron atomic ratio in the thin amorphous film layers on the PFC surface. For 1 MeV deuterons, the ratio of the neutron production cross sections for deuterium over elemental boron is $\sim$3 ($\sim$95 b / $\sim$35 b), giving an order of magnitude estimate of the deuterium-boron atomic ratio of $\sim$0.1. Despite significant assumptions, the result is in good agreement with deuterium-boron atomic ratios of $\sim$0.1 that have been found experimentally with *ex-situ* IBA of extracted PFC tiles in Alcator C-Mod [9] and provides confidence that the diagnostic is measuring reasonable isotopic ratios on the PFC surface.

Measurement error and validation

Whether the analysis is performed via gamma spectroscopy with the LaBr$_3$-SiAPD detector or neutron spectroscopy with the EJ301-PMT detector, the total detector counts from the integrated regions of interest must be normalized to the performance of the RFQ accelerator. The most important quantity is the total number of deuterons injected into the vacuum vessel during the detector pulse collection time, which is measured with a Pearson current transformer on the RFQ beamline. The error in the RFQ deuteron measurement - typically between 4% and 8% - must be propagated through the analysis, combining with error from the counting statistics, background calculation, background subtraction, and division of results to get the fractional isotope changes between successive measurements.

The combination of relatively small gamma production cross sections, low injected av-
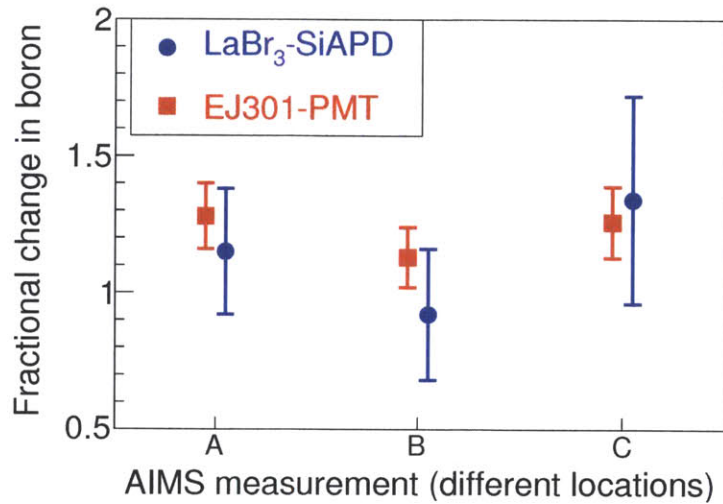
Figure 6-11: A comparison of the AIMS measurement of boron as quantified from neutrons and gammas with the EJ301-PMT and $LaBr_3$-SiAPD detectors, respectively. The key takeaway is that measurements from the two detectors agree very well with each other at each of the three different PFC measurement locations.

erage beam currents, and only a single gamma detector during the proof-of-principle phase of AIMS on Alcator C-Mod resulted in poor statistics on the $LaBr_3$-SiAPD detector. The final measurement error of the fractional change in isotopes from the $LaBr_3$-SiAPD detector was typically between 30% and 40%, with the counting statistics as the largest source of error. For the EJ301-PMT detector, the total counting statistics were much better due to the large neutron production cross section and large region of detector response integration. The final measurement error of the fractional change of isotopes is typically between 10% and 20%. The exact error for either measurement depends primarily on the total detector counts in the measurement and the noise levels on the Pearson current transformer.

Measurements of fuel retention in AIMS can only be made through neutron spectroscopy of the $^2H(d, n)^3He$ and $^3H(d, n)^4He$ reactions; however, there are isotopes, such as boron in Alcator C-Mod, that have both neutron and gamma production cross sections and exist in sufficient quantities to measure. AGNOSTIC provides for the simultaneous detection of neutrons and gammas using the EJ301-PMT and $LaBr_3$-SiAPD detectors, respectively, which have different data analysis procedures. Thus, the measurement of the fractional change in boron between AIMS measurements can provide a semi-independent experimental validation of the measured change in PFC surface properties and the data analysis methods.

Figure 6-11 shows such a comparison between the EJ301-PMT and $LaBr_3$-SiAPD detectors. The X-axis represents AIMS measurements acquired at three different PFC locations; the Y-axis represents the fractional change in boron between two successive AIMS measurements at three different locations. The key result is that at each

115

location the EJ301-PMT and LaBr$_3$-SiAPD detector measure identical changes to the PFC surface compositions well within statistical error bars. Such close agreement confirms that AIMS can reliably quantify PFC surface composition changes at multiple spatial locations. Furthermore, given that gamma-based IBA methods are strongly favored over the far more complex neutron-based methods [41], the agreement between the two detectors validates the use of neutron EJ301-PMT detector response analysis methods to perform IBA on materials in AIMS.

Chapter 7

The first AIMS measurements of fuel retention

As discussed in Chapters 1 and 2, the retention of fusion fuel in plasma-facing materials is one of the most challenging aspects of PMI. It has also historically been one of the most difficult to comprehensively diagnose *in-situ*. Measurements techniques have tended to extremes in terms of spatial information, with global (*i.e.* zero spatial resolution) measurements such as static gas balance or thermal desorption spectroscopy at one end and high spatial resolution measurements at only one or two remote locations such as laser desorption spectroscopy at the other end [4]. In contrast, AIMS is capable is making fusion fuel retention measurements over large fractions of the most relevant PFC surfaces with spatial resolution on the order of 1 cm. As a remote measurement technique that does not interfere with the normal shot cycle of a magnetic fusion device, AIMS is capable of providing such spatial information on a plasma shot-to-shot time scale in order to study the dynamic system of PMI.

The purpose of this chapter is to present the first *in-situ* measurements of deuterium retention using the AIMS diagnostic on the Alcator C-Mod tokamak. The measurements were made during two phases of the FY12 experimental campaign: intrashot during the final plasma experiments at the end of the campaign; and in between wall conditioning operations carried out after the campaign. The AIMS measurements were performed at the end of the campaign so that they could be linked to *ex-situ* ion beam analysis of PFC tiles that were extracted during the post-campaign maintenance period.

117

Figure 7-1: A timeline illustrating the plasma operations and wall conditioning processes that were carried out during the end of the FY12 Alcator C-Mod experimental campaign. The GDC was the final PFC perturbing process before the vacuum vessel was brought up to air for the maintenance period.

7.1 Overview of AIMS experiments during the FY12 campaign

The first substantive AIMS measurements of isotopic changes to the inner wall PFCs in response to plasma operations were carried out at the end of the FY12 plasma campaign. The measurements took place in two distinct phases: the first was throughout the plasma run that took place on October 2 2012 (Alcator C-Mod Run 1121002); the second was during wall conditioning experiments that took place between November 13-16 2012 after the plasma campaign concluded. A timeline depicting the history of plasma operations during the AIMS measurement period is shown in Figure 7-1.

7.1.1 Plasma operations

The 1121002 plasma run was broken into three separate sessions to accommodate three different physics experiments. The first two sessions were dedicated to issues of plasma control, turbulence, and heating in high-performance I-mode plasmas (plasma shots 1-24). Key plasma physics parameters and a representative magnetic flux surface reconstruction are shown for five of these I-mode shots in Figure 7-2. Of the 24 plasma shots, 18 were successful, full-length discharges with the rest either fizzling or disrupting early in the shot.

From the purposes of AIMS measurements that will be discussed below, the important points are that the plasma was run exclusively in a diverted lower-single null (LSN) configuration for all shots and that all shots were relatively similar in terms of the key plasma parameters: plasma current (I_p), average electron density ($n_{\bar{e}}$), central electron temperature (T_e), RF heating power (RF), radiated power (P_{rad}), and energy stored in the plasma (W_{plasma}). The LSN configuration is important because previous experiments on material migration in the boundary plasma have shown that the plasma net deposits material on the inner wall and inner divertor [109, 110]; the relative similarity between shots indicates that the deposition will be approximately constant for each shot. Thus, the total deposition for all shots divided by the number of shots provides a representative average of net deposition per shot.

118
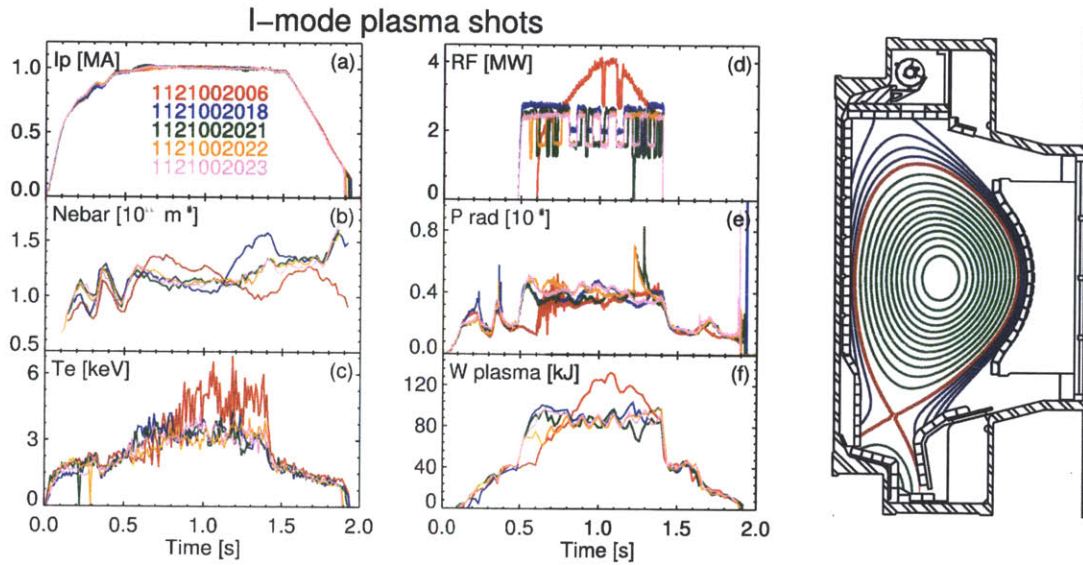
Figure 7-2: Time traces of key plasma parameters (left) and magnetic flux surface reconstruction (right) of several representative shots taken during the first part of the 1121002 run. All eighteen shots were relatively similar, with target plasmas being lower single null diverted I-Mode shots with 3 MW of RF heating and core densities of approximately 1.25×10^{20} m^{-3}.

After the two I-mode sessions were complete, the final shots of the 1121002 run were specifically dedicated for AIMS experiments (plasma shots 25-33). Key plasma physics parameters and a representative magnetic flux surface reconstruction are shown for the AIMS plasma shots in Figure 7-3. Of the 9 plasma shots, only four full-length IWL discharges were successfully produced. A major disruption occurred due to a molybdenum injection; the rest either fizzled or suffered issues with the Alcator C-Mod data system.

For the AIMS shots, an inner wall limited (IWL) plasma configuration was chosen rather than the standard diverted configuration. As evident from the magnetic flux surface reconstruction, the IWL places the separatrix strike point on the inner wall, which maximizes PMI in the region of inner wall PFCs that are accessible for measurement with AIMS. In particular, the net erosion of accumulated boron layers or molybdenum is expected in the strikepoint region. High levels of PMI activity can be inferred from visible imaging of the interior of Alcator C-Mod. Figure 7-4 shows a still image from the WIDE1 visible light camera that is located between A and B ports and is nearly centered on the PFCs that can be measured with AGNOSTIC. The horizontal band of visible light, which illuminates the individual PFC tiles on the central column inner wall, is produced mostly by Balmer α transitions as neutral deuterium recycles into the boundary plasma from the PFC surfaces, indicating strong local plasma flux incident at the surfaces. The AIMS measurement location used during intrashot measurements, as described below, is superimposed showing
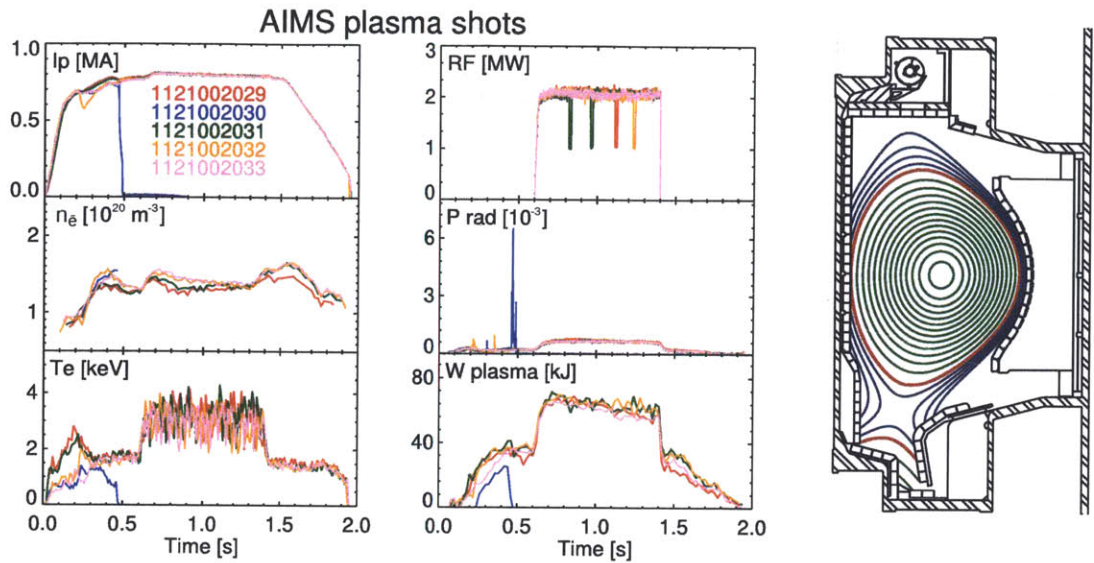
Figure 7-3: Time traces of key plasma parameters (left) and magnetic flux surface reconstruction (right) of the five plasma shots dedicated for AIMS experiments in the final part of the 1121002 run. Four successful inner wall limited plasmas were achieved with identical conditions; one shot terminated early due to a molybdenum injection.
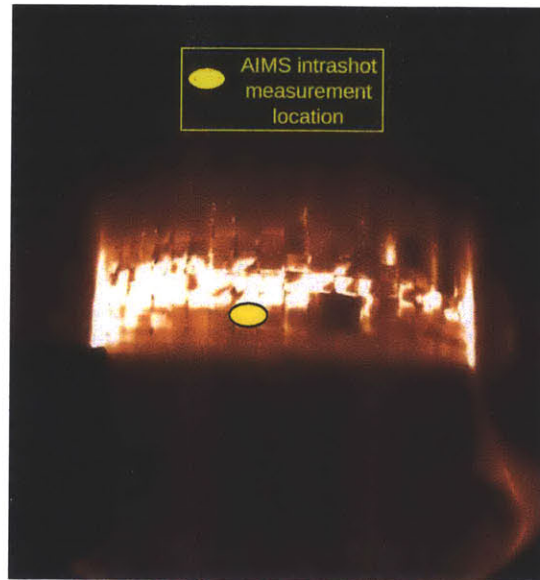
Figure 7-4: A still image from the WIDE1 visible camera during shot 1121002031 on Alcator C-Mod. The image is looking directly at the central column. Illuminating the individual PFC tiles, the visible light is produced mostly by deuterium neutrals entering the cool plasma boundary and indicates significant PMI on the inner wall PFCs. The location of the intrashot AIMS measurement is superimposed, showing the close proximity the region of maximum PMI.

(a) Poloidal boron thickness

(b) Deuterium codeposition
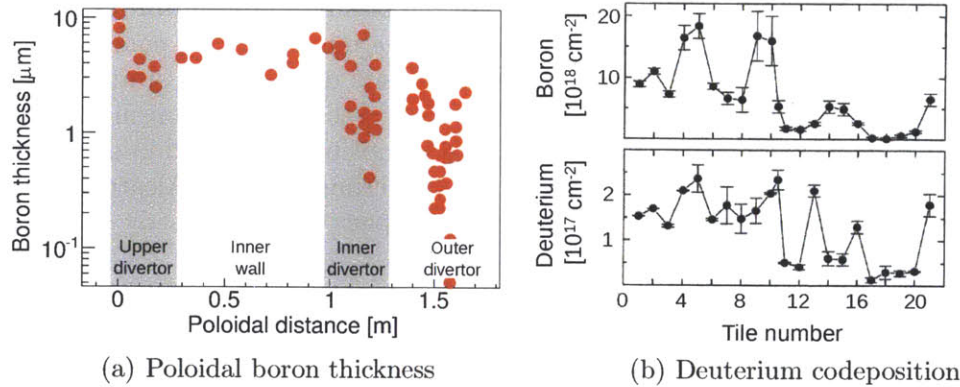
Figure 7-5: The inner wall PFCs of Alcator C-Mod are regions of net boron deposition (a), accumulating $\lesssim 5$ μm thick boron layers over several years of operation (Figure adapted from [111]). As shown by the nearly identical tile-to-tile variation in *ex-situ* ion beam analysis (b), the boron layer is saturated with deuterium (Figure adapted from [109]). Deuterium/boron atomic ratios are typically found to be $\sim$0.1 although ratios as high as $\sim$0.4 have been measured [110].

its proximity to regions of high PMI activity during IWL shots. plasma to induce detectable net erosion of the inner wall PFCs.

Again, as with the I-Mode shots, the relative similarity between successful IWL discharges indicates that the PMI effects should be similar for each shot, enabling a representative measure of average net erosion per shot to be obtained from measurements across several plasma shots. The single IWL disruption terminated early in the discharge with a sufficiently small core electron temperature ($\approx$0.75 keV) and stored energy in the plasma ($\approx$30 kJ) to be minimally disruptive to the PFC surface conditions when compared against previous studies of disruption-induced PMI [110].

The contrast between the expected PFC surface changes during LSN and IWL plasma shots provides an excellent canvas upon which AIMS can paint its colorful intrashot masterpiece. *Ex-situ* IBA on poloidal rows of tiles extracted after plasma campaign have shown that the inner wall and inner divertor in Alcator C-Mod are regions of *net* deposition during plasma operation due to material migration in the boundary region from the outer divertor [109, 111]; the finding is consistent with experiments in the JET and ASDEX-Upgrade tokamaks [20]. Figure 7-5a shows the buildup of the amorphous boron films as a function of poloidal tile location on Alcator C-Mod.

Boron is eroded by the plasma from the outer divertor near the separatrix strike-point and transported to the inner wall and divertor. Combined with the repeated boronizations throughout several years of operations on Alcator C-Mod, the material migration results in 5-10 μm layers of boron on the inner wall PFCs. The boron layers have been found experimentally to be rich in retained deuterium as shown in Figure 7-5b, where atomic ratios of deuterium to boron are $\sim$0.4 immediately after

boronization but decrease to ~0.1 by the end of the plasma campaign in Alcator C-Mod [9]. The strong poloidal correlation between deuterium and boron concentration suggests that the plasma erodes and locally codeposits deuterium-saturated boron layers. This is important for understanding deuterium retention mechanisms in Alcator C-Mod. If the boron locally codeposits almost completely saturated in deuterium then it cannot explain the large *net* retention of deuterium found in Alcator C-Mod since there is not enough extra deuterium storage capacity in the already saturated boron films [110].

By design, the IWL shots immediately following the LSN shots were intended to induce exactly the opposite behavior on the PFC surfaces. Limiting the plasma against the inner wall has the effect of directing the most energetic power exhaust flux to the inner all PFCs accessible for AIMS measurement as possible, as shown in Figure 7-4. In effect, the net erosion conditions that lead to the almost bare molybdenum PFCs in the outer divertor in Figure 7-5b have been moved to the AIMS measurement locations. In Alcator C-Mod, the beneficial plasma performance effects caused by the ~150 nm of boron deposited on the outer divertor during standard boronizations disappear in 15-50 shots, leading to estimated boron erosion rates at the strikepoint on the order of 1-10 nm shot^{-1}.

7.1.2   Wall conditioning

Following the conclusion of the FY12 plasma campaign, the Alcator C-Mod vacuum vessel was kept under vacuum for approximately five weeks in order perform a number of routine diagnostic and instrument calibrations. The isotopic composition of the PFC surfaces during this time remained frozen to that at the end of the plasma campaign as no procedure was carried out during this time that has the ability to modify the PFC surfaces. Once the calibrations were complete, a series of AIMS-specific wall conditioning operations were performed in order to measure changes to the inner wall PFCs.

As shown on the timeline in Figure 7-1, three different wall conditioning procedures were carried out: boronization (BZN), electron cyclotron discharge cleaning (ECDC), and glow discharge cleaning (GDC). Boronization is a procedure that is used in Alcator C-Mod to deposit ~150 nm boron films on PFC surfaces in order to achieve substantial increases in plasma performance [9]. First, the vacuum vessel is filled with a low pressure ($\lesssim$2 Pa) gas mixture of 10% deuterated diborane (D_2B_6) / 90% helium-4. 2.5 kW of radiofrequency (RF) waves at 2.45 GHz are injected into the vacuum vessel to ionize the gas molecules. The ionization occurs at the electron cyclotron resonance (ECR) location, which is fixed in major radius by the value of the toroidal field at B = 0.088T. In standard boronizations, the toroidal field is continuously varied in magnitude to sweep the ECR location radially in an attempt to deposit a uniform boron thickness poloidaly on PFCs [112].

(a) Radial boron deposition profiles   (b) Experimental geometry
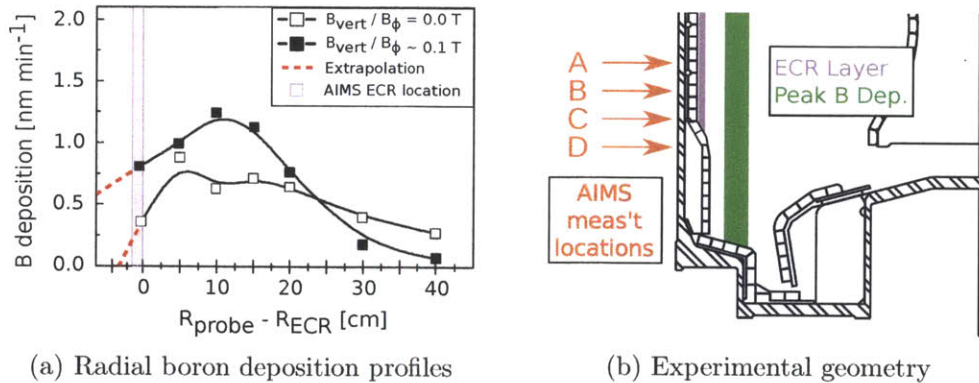
Figure 7-6: Experimental measurements with a quartz-microbalance (a) show that the peak boron deposition location is approximately 10 cm radial outboard of the electron cyclotron resonance (ECR) location (Figure adapted from [113]). Shown in both figures is the ECR location during boronization (BZN) and electron cyclotron discharge cleaning (ECDC), where it was held at a major radius of 43-44 cm to maximize induced changes to the inner wall PFC surfaces.

Recent experimental work with a quartz microbalance (QMB) in Alcator C-Mod has shown that boron deposition is ionic, peaking approximately 10 cm radially *outboard* of the ECR layer due to the influence of $\mathbf{E} \times \mathbf{B}$ drifts on the boron ions [113]. The radial boron deposition profiles, shown in Figure 7-6a for two different vertical magnetic field values, peak between 5 and 15 cm outboard of the ECR with peak deposition rates of approximately 1.25 nm min^{-1}. Because of the composition of the deuterated diborane, the deuterium/boron atomic ratio has been found to vary between 0.1 and 0.4 [9].

Two types of plasma techniques are used to condition the wall inside the vacuum vessel. ECDC is nearly identical to boronizations with the exception that the vacuum vessel fill gas is typically 100% helium-4. Singly ionized helium-4 nuclei bombard the PFC surface and desorb impurities, which can be removed with the vacuum system pumps [114]. GDC is a common technique in a variety of high vacuum applications where it that is used to remove impurities from the chamber walls [115]. In Alcator C-Mod, GDC is principally used after the conclusion of a plasma campaign to neutralize and remove residual boron compounds before manned access [112]; the use of boron is described below. GDC is performed by holding two invessel electrodes at approximately +1 kV while the PFC metals are held at ground. Ionized atoms from the helium fill gas are accelerated by the electric field, bombard the PFCs, and desorb impurities, which can then be removed with the tokamak vacuum pumps.

It is important to understand the expected effects of each conditioning process on regions that AIMS can presently interrogate. The AIMS measurement locations are presently confined to a small ($\sim 35 \times \sim 2$ cm vertical section) of the inner wall PFCs. Depositing boron and using ECDC on the inner wall, however, is problematic because the radially outward $\mathbf{E} \times \mathbf{B}$ drift prevents ions from reaching the inner wall. For

123
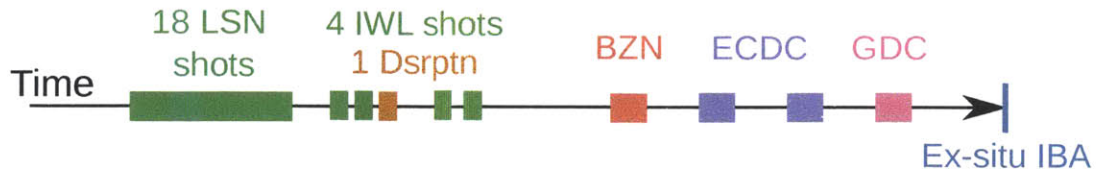
Figure 7-7: A timeline emphasizing the difficulty of using *ex-situ* IBA after a several month plasma campaign to elicit the dynamics of PMI. Although the PFC surface compositions are changing on a shot-to-shot timescale, only a single, post-plasma campaign "snapshot" of the PFCs can be obtained with *ex-situ* IBA.

boronization, the effect is that the boron deposition rate rapidly falls to zero within a few centimeters radially inboard of the ECR, as shown in Figure 7-6a. Coupled to the scanning of the ECR, where the resonance is swept and only comes with a few centimeters of the inner wall to prevent termination of the plasma, the boronization should minimally deposit on the inner wall PFCs. For ECDC, the result is that ions have a more difficult time reaching the inner wall PFC surfaces, making this region particularly difficult to affect with ECDC. In GDC, ions are accelerated to the walls electrostatically with no magnetic field present, and, therefore, we expect GDC to perturb the inner wall PFC surfaces.

Given the potential low impact of wall conditioning to the PFCs accessible to AIMS, the ECR resonance was held at a constant major radius of 43-44 cm during the entire process rather than swept radially across the vacuum chamber as is normally done; the position of the ECR radius during the boronization and two ECDCs is shown in Figure 7-6b. The boronization lasted 120 minutes with a 10% diborane / 90% helium-4 gas mixture at an average vessel pressure of 2.7×10^{-3} torr (vacuum thermocouples). The two ECDC sessions were conducted with helium gas with at an average invessel pressure of 2×10^{-4} torr (vacuum ion gauges). During the first ECDC, attempts to hold the ECR at a major radius of 43 cm led to continuous plasma termination, resulting in only about 50 minutes of operational time. For the second ECDC, the ECR location was moved to 44.1 cm, where a stable 120 minute discharge was achieved. The twenty-four hour GDC was also conducted in helium gas with an electrostatic potential of approximately 1000 V between the charged plates and the PFC surfaces; average invessel pressure was 2×10^{-2} torr (vacuum ion gauges).

7.2 Post-campaign ex-situ ion beam analysis

Following the conclusion of the FY12 campaign, a module of molybdenum PFC tiles was removed from the inner wall during the vacuum break and taken to an offsite facility for *ex-situ* IBA, as shown in the timeline that appears in Figure 7-7 The module of 8×8 tiles encompasses AIMS measurement location two of the locations that were routinely measured with AIMS during the plasma campaign and wall conditioning experiments - locations "A" and "B" shown in Figure 7-6b.

124
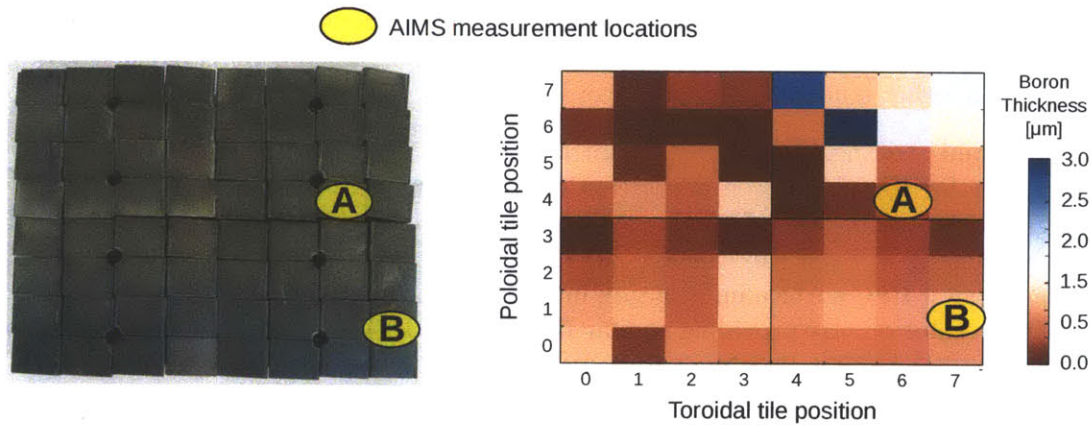
Figure 7-8: An inner wall 8×8 PFC tile module was removed from Alcator C-Mod (left) after the conclusion of the FY12 campaign for *ex-situ* ion beam analysis, which determined the average boron thickness on each tile (right). AIMS measurement locations "A" and "B", corresponding to toroidal field coil currents of 0.0 and 1.6 kA, respectively, are superimposed on top of the tile grids for reference. Time constraints prevented measuring the deuterium concentration.

Due to the demanding operation schedule of Alcator C-Mod, only twenty-fours were available for analysis before the module had to be returned for installation before vacuum pumpdown. Only a single module could be removed and analyzed due to time constraints. While this time was sufficient to measure the boron layer thickness on each of the sixty-four PFC tiles via gamma spectroscopy of the $^{10}B(p, \alpha\gamma)^7Be$ reaction, deuterium retention was not able to be measured. The tile module also had to be analyzed in air rather than vacuum, leading to relatively large measurement errors (10-20%) due to ion beam slowing down in the air gap between beam window and PFC surface. These resource-based restrictions on such *ex-situ* measurements provide one of strongest motivations behind AIMS.

7.2.1 Measurements of absolute boron layer thickness

The results of the *ex-situ* IBA are presented in Figure 7-8, which shows the absolute boron layer thickness covering each of the PFC tiles in the module. Several features are immediately striking about the result. First, there is a strong variation in the boron layer thickness in the poloidal and toroidal directions, approaching layer thickness differences of almost two orders of magnitude on some adjacent tiles. Such variation in the boron deposition cannot be explained by the physics of boronization. The diborane gas is distributed uniformly in the vacuum vessel by a series of toroidally symmetric gas valves and, and the ECR resonance is poloidally symmetric on the inner wall PFCs [112]. Although there is a very small misalignment in the PFC tiles that may account for some of the effect, the complex deposition pattern must result from the anisotropic erosion and redeposition PMI processes that occur dur-

125

ing plasma operation, which has been suggested by previous *ex-situ* IBA and plasma studies [9, 116]. The AIMS analysis of boron erosion and redeposition are the primary topic of another student's PhD and can be found in [55].

The second striking feature is the contrast between the dynamic PMI processes responsible for complex boron deposition over a six month plasma campaign and the single, static "snapshot" of the deposition pattern provided by *ex-situ* IBA at the end of the campaign. Such "archaeological" measurements have provided the majority of experimental PFC surface information in PMI science despite the enormous disparity in time resolution. By providing similar IBA-derived PFC surface data measurements but on a shot-to-shot time resolution - and without requiring resource-intensive extraction and offsite analysis - AIMS represents a quantum leap forward for the *in-situ* diagnosis of PFC surfaces.

7.2.2 Application of ex-situ results to AIMS measurements

One of the principle motivations for performing *ex-situ* IBA on the same region of PFC tiles that was accessible to AIMS was to be able to transform the *relative* AIMS measurements of isotope concentrations to *absolute* measurements. This process can be accomplished due to two reasons. First, AIMS measurements were acquired immediately before the Alcator C-Mod vacuum vessel was brought up to air for the post-campaign maintenance period. The composition of the PFC tiles measured by AIMS must match the composition measured during *ex-situ* since there was no surface perturbing process carried out in between. Therefore, the absolute boron layer thickness determined by *ex-situ* IBA can be assigned to the final measurement in time taken with AIMS.

Second, AIMS acquired over ten time-resolved measurements of the fractional change in surface composition during the plasma operations and wall conditioning processes at the end of the FY12 campaign. By pinning the final AIMS measurement to the absolute boron layer thickness and knowing the fractional change in boron at over ten points back in time, a post-mortem reconstruction of the absolute boron layer thickness can be made with the AIMS data for the two PFC locations that were measured by both techniques.

The absolute determination of changes in the boron layer thickness on a plasma shot-to-shot timescale provides tremendous insight into the PMI dynamics of material erosion and redeposition; the results of this branch of AIMS analysis is the subject of another student's Ph.D. dissertation [55] and will only be briefly described briefly here for validation purposes.

As will be discussed in detail in Section 7.4, AIMS measurements were acquired for each wall conditioning process, including at the two locations that overlapped the *ex-situ* IBA measurement. By pinning the final AIMS measurements at these locations to the absolute boron thicknesses, the absolute boron deposited during the
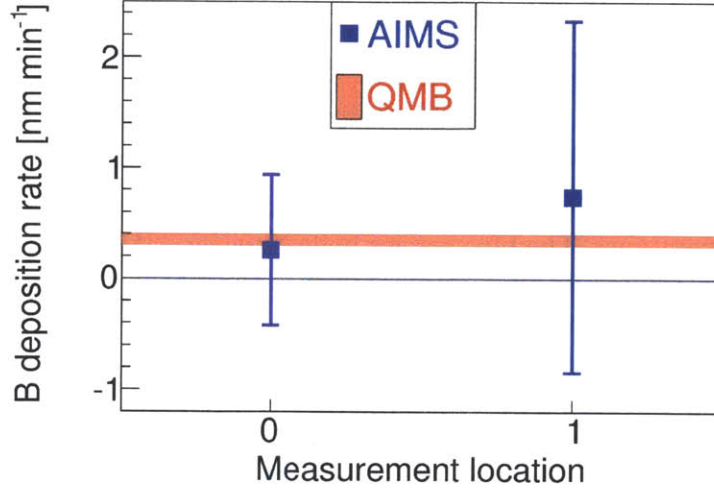
Figure 7-9: The comparison between AIMS and QMB measurements of the boron deposition rate on the inner wall PFCs shows reasonable agreement, validating the use of AIMS to measure absolute boron thicknesses when normalized against post-campaign *ex-situ* IBA measurements.

120 minutes BZN can be calculated by stepping backwards in time with the fractional boron changes measured by AIMS. Since the boron deposition rate has been measured experimentally with the QMB (Figure 7-6a) for surfaces parallel to the plasma, the AIMS-computed boron deposition rate can be experimentally validated.

The validation results appear in Figure 7-9, which compares the boron deposition rates measured by AIMS and a QMB for surfaces between 0 and 1 cm radially inboard of the ECR. The large uncertainty in the AIMS measurements is primarily a result of combining and propagating the large error from the *ex-situ* IBA measurements described above with the relatively modest error from the AIMS measurements. The sensitivity of AGNOSTIC measurements at present are $\sim$1 nm min^{-1} for the boron deposition rate or $\sim$200 nm for the total boron deposited during the 120 minutes BZN. Despite the large error, the AIMS measurements are certainly consistent with the results from the QMB measurements, providing confidence in the use of the above technique to correctly measure the absolute boron thickness.

For the issue of fuel retention, the ability to extract the absolute boron layer thicknesses actually provides AIMS with a crude measure of the absolute deuterium content. Analysis of these plasma-deposited boron layers from Alcator C-Mod [9], TEX-TOR [117], and laboratory experiments [118] have all found consistent atomic ratios of deuterium to boron, typically saturated up to ratios of 0.4 immediately following a deuterated diborane boronization but as low as 0.1 during post-campaign analysis [110]. Thus, the areal density of deuterium, ρ_a^D, in the boron layers can be estimated as

$$\rho_a^D = L_B \cdot \frac{N^D}{N^B} \cdot \frac{\rho_m^B N_A}{A^B} \tag{7.1}$$

127
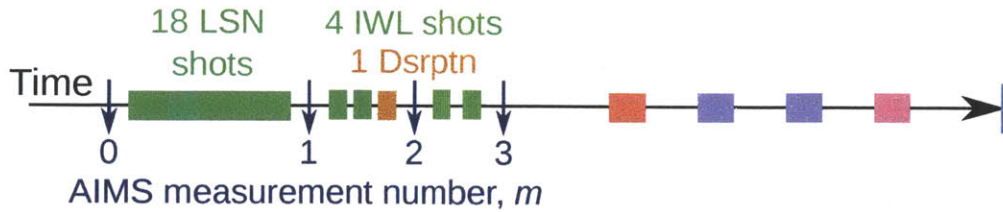
Figure 7-10: A timeline illustrating the intrashot measurement capabilities of AIMS during plasma operations. The blue arrows indicate when AIMS measurements were acquired, showing the ability to discern changes in the PFC surface composition on a shot-to-shot timescale.

where L_B is the boron thickness, $\frac{N^D}{N^B}$ is the deuterium-to-boron atomic ratio, ρ_a^B is the mass density of boron (usually considered 2.37 g cm^{-3} for pure elemental boron), N_A is Avogadro's number, and A^B is the atomic weight of elemental boron (10.811 g mol^{-1}). Combined with the absolute boron thickness changes measured with AIMS and the *ex-situ* results, Equation 7.1 provides an estimate of local net fuel retention.

7.3 AIMS measurements of deuterium retention during plasma operations

As shown on the timeline in Figure 7-10, four AIMS measurements of the inner wall PFCs were acquired throughout the plasma run day on October 2, 2012. Each measurement was assigned a sequential number, m, beginning with zero:

- $m = 0$: Acquired before the 18 I-mode LSN shots

- $m = 1$: Acquired before the AIMS-specific IWL shots

- $m = 2$: Acquired after 2 IWL shots and 1 disruption

- $m = 3$: Acquired after 2 IWL shots

In order to maximize the number of AIMS-specific plasma shots before the end of the run day, only a single PFC location on the inner wall was interrogated during the $m = 2$ measurements to avoid delaying plasma operations.[1]

---

[1]While the AIMS technique is, in principle, easily capable of scanning many PFC locations in the approximately ten or so minutes in between plasma shots on Alcator C-Mod, the present measurement time is limited by the number of detectors and the relatively low duty cycle of the RFQ accelerator. In addition, the Pearson transformer coil, which is used to measure the deuteron beam current entering the vacuum vessel, is susceptible to strong magnetic forces from the TF coils during plasma shots. For reasons of experimental convenience, the transformer was not secured on the beamline to withstand these forces; a time-consuming cell access was required to install and then
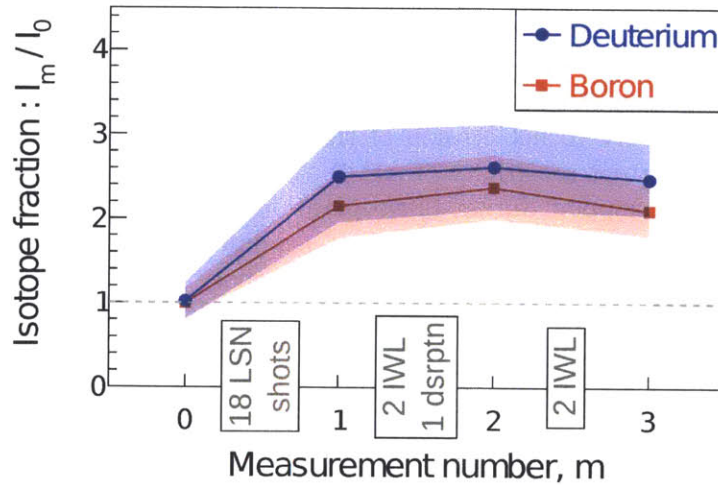
Figure 7-11: The fractional change in deuterium and boron during plasma operations. Local codeposition of deuterium with boron during the eighteen lower single null (LSN) diverted shots is evident. When the plasma configuration changes from diverted to inner wall limited (IWL) at $m = 1$, the boron-deuterium deposition rate becomes approximately essentially zero.

7.3.1   Results

7.3.2   Discussion

The most prominent feature of the measurements is the nearly identical trends in the fractional change of deuterium and boron during both LSN and IWL plasma shots. The result confirms the hypothesis that the plasma is eroding and redepositing deuterium-saturated layers of boron, which is of critical importance for understanding which potential physical retention mechanisms are responsible for fuel retention in low-Z film-coated refractory metal PFCs. As discussed above, it has been hypothesized that if the plasma were eroding and redepositing partially to fully saturated boron film then the amount of available deuterium storage is insufficient to explain the net deuterium retention experimentally found in Alcator C-Mod. The AIMS intrashot results corroborate this hypothesis, suggesting that alternative mechanisms for fuel retention must be investigated. The intrashot, *in-situ* fuel retention measurement capabilities of AIMS present one of the most compelling paths of future investigation in this area.

Another prominent feature in the deuterium and boron trends is the distinct bifurcation from net deposition during the LSN shots to zero (with a hint of net erosion)

---

remove the transformer. Hardware upgrades in the next iteration of the experiment will reduce the measurement times by a factor of 10 to 20 while the transformer coil will be structurally secured to the beamline.

deposition during the IWL shots. The first part of the trend is consistent with the expectations of material migration and redeposition in the boundary plasma from the outer divertor to the inner wall and divertor during LSN operation. Net deposition ceases immediately with the conclusion of the LSN shots, leading to either zero net deposition or more likely to net erosion of the boron layer that is too small to be measured with the current sensitivity of AIMS. As discussed above, boron erosion at the outer divertor strikepoint during LSN operation in high performance plasmas is on the order of 1-10 nm shot^{-1}, resulting in a maximum erosion during the 4 IWL shots of 40 nm that is well below the present sensitivity of AGNOSTIC to changes in boron layer thickness of a few hundred nanometers. Nevertheless, the null result is another important demonstration of AIMS capabilities since the measurement of no statistically significant erosion is consistent with the extremely low erosion rates that could be achieved in only 4 IWL plasma shots.

The primary mechanism of fuel retention in a future fusion reactor may not be codeposition in low-Z films; however, tremendous insight into the enormous challenge of fuel retention can be gain from a simple estimate. Consider a typical reactor-scale device (R = 6 m, a = 2 m, total PFC area $\sim$600 m^2) that boronizes in between deuterium-tritium plasma runs, leading to similar material migration and net deposition over most of the PFC surfaces as in Alcator C-Mod. For an assumed 5 μm boron layer with a saturated atomic deuteron-to-boron ratio of 0.4, Equation 7.1 gives areal density of $\sim 2 \times 10^{23}$ fuel atoms retained per square meter. This corresponds to approximately 0.25 kg of tritium retained only in the low-Z film and does not account for the other retention fuel mechanism in refractory metals. This simple exercise provides strong motivation to study fuel retention in micron-level films. 0.25 kg of in-vessel tritium is a serious nuclear hazard, potentially requiring suspension of device operation for cleaning, and probably makes sufficient tritium breeding infeasible.

7.4 AIMS measurements of deuterium retention during wall conditioning

As shown on the timeline in Figure 7-12, five AIMS measurements of the inner wall PFCs were acquired throughout the series of wall conditioning experiments that took place on November 13-16, 2012. As before, each measurement is assigned a sequential number, m, beginning with zero:

- $m = 0$: Acquired before the BZN

- $m = 1$: Acquired after the BZN

- $m = 2$: Acquired after ECDC #1

- $m = 3$: Acquired after ECDC #2
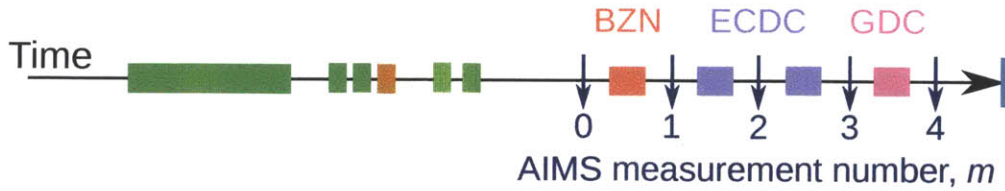
Figure 7-12: A timeline illustrating the AIMS measurements between wall conditioning experiments. The blue arrows indicate when AIMS measurements were acquired.

- $m = 4$: Acquired after GDC

7.4.1 Results

The results of the AIMS measurements are presented in Figure 7-13, which shows the fractional changes in deuterium and boron relative to the $m = 0$ measurement at locations A, B, C, and D on the inner wall PFCS. Locations A, B, and C are located at a major radius of R = 43 cm while measurement location D is located at R = 46 cm due to the "skirt" region of the inner wall that extends radially outwards approximately 3 cm from the rest of the PFCS. The deuteron beam trajectories in the Alcator C-Mod vacuum vessel and PFC measurement locations are shown to the right of the figure for reference. Vertical labels on the graphics indicate the wall conditioning processes that occurred in between each AIMS measurement.

7.4.2 Discussion

Figure 7-13 experimentally demonstrates all of the key features of the AIMS technique, fulfilling the PFC surface diagnosing capabilities required to advance PMI science as outlined in Chapter 3. The most important feature of the figure is the ability of AIMS to produce localized, time-resolved measurements of the fractional changes of isotopes over a nontrivial region of the inner wall PFCs; combining the measurements with the *ex-situ* IBA results as described above enables the extraction of the absolute boron thicknesses and estimated retained deuterium areal densities.

Of all the wall conditioning processes conducted during these experiments, boronization is the most well understood in terms of the induced physical changes to the PFC surfaces. For the upper three measurement locations (A, B, and C), the fractional increase in boron as a result of boronization is relatively small: 1.13 ± 0.09, 1.09 ± 0.09, and 1.16 ± 0.10. All three measurements agree closely and well within the statistical error bars, reflecting the expected poloidally uniform deposition of boron for PFCs at a constant major radius during BZN. The results also indicate that AIMS is measuring a physical change to the PFC surface, *i.e.* it is unlikely that the three identical measurements of boron increases - made at different locations and over the course of two days - are due to random effects in the AGNOSTIC equipment or data analysis.

131

Figure 7-13: The fractional changes in deuterium and boron at the locations A, B, C, and D on the inner wall during the wall conditioning experiments that were performed at the end of the FY12 campaign: boronization (BZN), electron cyclotron discharge cleanings (ECDC), and glow discharge cleaning (GDC).

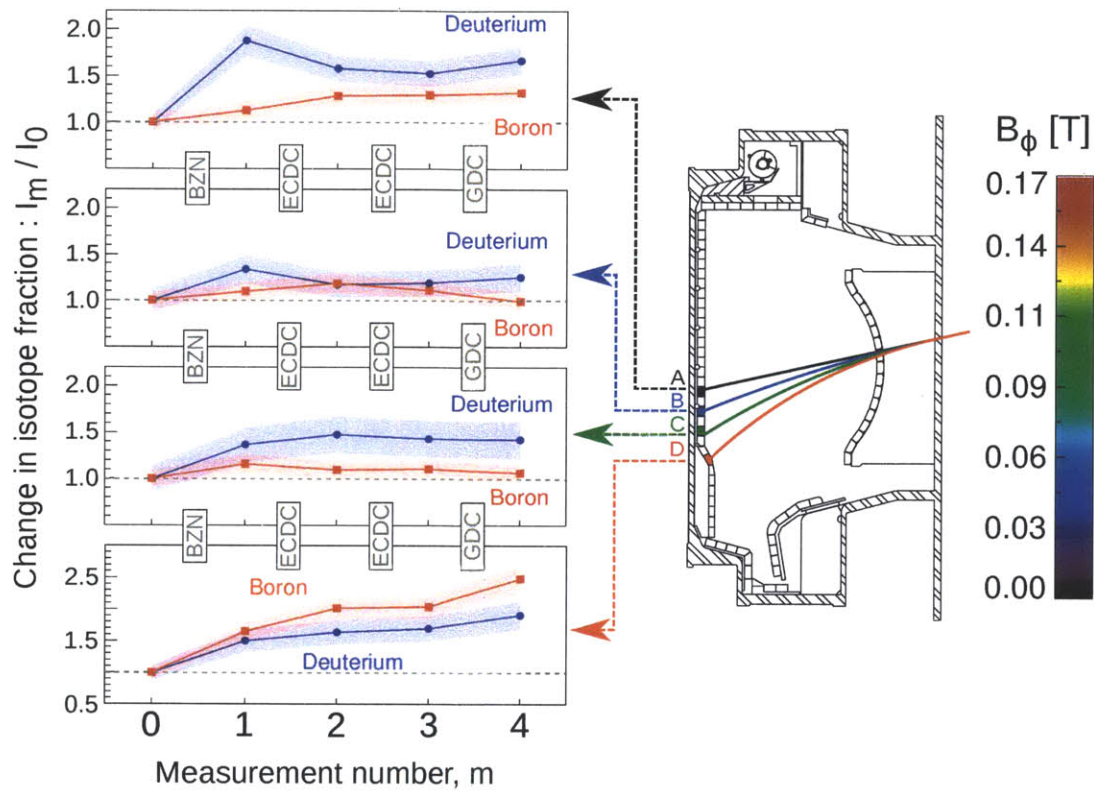From the *ex-situ* IBA results and the fractional boron change AIMS measurements in Figure 7-13, the maximum thickness of boron before the BZN was on the order of a few hundred nm. Given the ∼10% increase due to BZN measured at the upper AIMS locations, the result is that only a few tens of nanometers of boron were deposited on the upper three AIMS measurement locations, despite holding the ECR within ≲1 cm of the inner wall PFCS for 120 minutes. The finding is consistent with the hypothesis that boron deposits ionically during BZN and is largely prevented from reaching the inner wall due to radially outward $E \times B$ drifts imposed by the toroidal field during BZN.

Even more interesting is the significant difference between boron changes on locations A, B, and C (R = 43 cm) and on location D (R = 46 cm), which extends radially outward approximately 3 cm beyond the upper inner wall PFCs as shown in in the cross section of the vacuum vessel in Figure 7-13. Unlike the upper three measurement locations, which were ∼0.5 cm *inboard* of the ECR during the BZN, location D is approximately ∼2.5 cm *outboard* of the ECR and should experience a significantly higher boron deposition rate as shown in the radial boron deposition profiles of Figure 7-6a. The fractional increase in boron measured at the bottom most location was 1.65 ± 0.15, well above the previous measurement at the upper locations, which is a strong confirmation of the QMB-measured radial boron deposition profiles.

Turning from boron to deuterium retention, it is evident that the fractional changes of deuterium and boron are not tightly linked during wall conditioning as they were during plasma operations. As discussed above, the intrashot AIMS measurement corroborate the theory that the plasma erodes, transports, and redeposits deuterium-saturated layers boron layers with atomic deuterium-boron ratios approaching 0.4; however, as measured by AIMS, wall conditioning effects the boron and deuterium on the PFC surface differently. This may, in part, explain why saturated boron layers with atomic ratios of ∼0.4 are deposited during BZN, but post-campaign measurements measure only measure ∼0.1. Although the AIMS measured changes at locations A, B, and C (R = 43 cm) suggest that the atomic ratio increases (inconsistent with hypothesis), location D (R = 46 cm) shows that boron increases significantly more than deuterium in just a few wall conditioning experiments, consistent with a decreasing deuterium-to-boron ratio. Given that much of the PFC surfaces are radially outboard of the ECR during wall conditioning, the R = 46 cm result is probably the more representative result and suggests a promising path of future research to understand the deuterium-to-boron atomic ratios in amorphous films.

Finally, the results in Figure 7-13 demonstrate that the fractional increases of deuterium are larger than those of boron for the three R = 43 cm measurement locations; the reverse is true for the R = 46 cm location, which shows a higher fractional increase in boron compared to deuterium. The result suggests that the majority of deuterium, unlike the *ionic* deposition of boron, deposits as *neutral atoms* on the PFC surface after the diborane molecules are ionized during the BZN. Neutral deuterium atoms would not be subject to the $E \times B$ forces that effect the ionic boron, resulting in deuterium deposition being a far more isotropic process than boron deposition. The

fraction of deuterium that deposits radially *inboard* of the ECR would be higher than for boron, which is corroborated by the AIMS measurement of the PFCs at R = 43 cm (-0.5 cm inboard of the ECR). Conversely, roughly the same fraction of deuterium deposits radially *outboard* of the ECR but, in this case, the fractional increase of boron would be substantially higher due the peaked radial boron deposition profiles. While the AIMS results are consistent with this explanation, further work is required to understand the nature of deuterium deposition in Alcator C-Mod during BZNs.

Chapter 8

Concluding remarks

This thesis has presented the scientific motivation for and a conceptual description of AIMS, a new experimental technique for the *in-situ* interrogation of PFC surfaces in magnetic fusion devices. The descriptions and performance of the experimental components of the first AIMS diagnostics on Alcator C-Mod were examined as well as computational modeling activities that were essential during diagnostic development. Finally, the validation and first measurements of deuterium retention and boron erosion and redeposition during plasma operations and wall conditions were presented.

The purpose of this concluding chapter is to summarize the key results, perhaps most importantly, to illuminate the most important technical areas of the diagnostic technique and experimental hardware that could be dramatically improved in the near future for AGNOSTIC or in future implementations of an AIMS diagnostic at another facility.

8.1 Summary of the key results

- The design, implementation, and validation of the first AIMS diagnostic on Alcator C-Mod has been presented. The diagnostic has been shown to be capable of measuring localized isotopic PFC surface compositions at multiple locations and on a plasma shot-to-shot timescale. The successful demonstration of the diagnostic represents a significant advance in the experimental diagnosis of materials in magnetic fusion devices and could lead to new understanding in PMI.

- The feasibility of using the magnetic fields of a magnetic fusion device to steering an injected deuteron beam to the PFC surfaces of interest A 3D beam dynamics code was shown to be capable of predicting the deuteron trajectories in the magnetic fields. The use of nuclear kinematics and neutron spectroscopy validated the code by demonstrating a shift in spectral features that agreed very well with the predictions of the code.

- The feasibility of using AIMS to identify and quantify several of the key isotopes of interest for PMI, including deuterium and boron, was experimental demonstrated. Agreement was demonstrated between the neutron (EJ301-PMT) and gamma (LaBr$_3$-SiAPD) detectors for the measurement of boron changes on several inner wall PFCs validating the spectra analysis methods.

- The development and validation of a comprehensive Monte Carlo synthetic diagnostic for AIMS (ACRONYM) was presented. The simulation played a key role in determining the feasibility of neutron and gamma spectroscopy in Alcator C-Mod, optimizing the detector design and location, and providing insight into the spectral features of experimentally acquired detector responses.

- The development of a new method for the high-fidelity simulation of organic scintillation detectors has been presented. For the first time, the method enables the simulation of detector response functions and pulse shape discrimination capabilities for detectors of arbitrarily complex geometry and light readout configurations; the simulation can be performed within a larger experimental geometry to capture the realistic complexities of detection. Such capability is critical for fully modeling AIMS measurements with ACRONYM. Importantly, the method is now included in the world-leading Monte Carlo simulation toolkit of particle, nuclear, space, and detector physics, Geant4.

- The first time-resolved, localized AIMS measurement of deuterium retention in a magnetic fusion device during plasma operations have been presented. The measurements provide experimental evidence to support the theory that the plasma erodes and redeposits deuterium-saturated boron layers on top of the PFCs. The finding is important because it eliminates deuterium codeposition in boron layers as the responsible PMI mechanism for the *net* deuterium retention observed in Alcator C-Mod.

- The first time-resolved, localized AIMS measurements of the changes in boron and deuterium at four distinct locations on the inner wall PFCS of Alcator C-Mod during wall conditioning experiments have been presented. The result is important because it experimentally fulfills the promise of the AIMS technique to provide cartographic mapping of the changes of the isotope content on the accessible PFC surfaces as a function of time. Such data will be crucial to advance experimental PMI science and to use in the development of computational PMI codes that are critical for magnetic fusion energy reactor development.

8.2 Recommendations for AIMS development

This sections contains several key suggestions for the continuing development of the AIMS technique. While several recommendations are somewhat obvious - the need to

136

increase the number of detectors to reduce measurement times, to improve the performance of the RFQ, to maximize the signal-to-noise ratio of the detectors through geometry - the following recommendations are much more involved. In each case, work has already begun, and it is hoped that this section provides enough information to continue these developments at Alcator C-Mod or other magnetic fusion devices interesting in deploying an AIMS diagnostic.

8.2.1 Develop an EJ301-SiPM detector

As discussed in Chapters 3 and 4, a key requirement for particle detection in AIMS is the capability to operate in the relatively strong magnetic fields - $\lesssim 0.1$ T in Alcator C-Mod, that are used to steer the incident deuteron beam. This capability enables the detectors to operate as close to the PFC measurement surfaces as possible, maximizing the detector solid angle and signal-to-noise ratio. While the EJ301-PMT detector performed admirably, producing most the of results in this thesis, its sensitivity to magnetic fields required it to be located at the entrance of the reentrant tube, almost half a meter further away from the PFCs than the $LaBr_3$-SiAPD detector. Increasing its proximity to the PFCs would have results in a much more prominent deuterium signal in the EJ301-PMT spectrum by increasing the detected unscattering neutrons from the $^2H(d,n)^3He$ reaction compared to the large scattering background.

An upgrade to the neutron detection capability in AGNOSTIC has already begun and should continue as part of future AIMS development work. The new detector is composed of a 2.5×2.7 cm cell of EJ301 but is coupled to a large area SiPM array for optical readout. An important aspect of large area SiPMs are their high output capacitance, which is typically 1-2 nF. When coupled to standard commercially available current-sensitive preamplifiers, the high output capacitance couples with the input impedance to slow the time response to the SiPM-preamplifier combination. Although the time degradation is on the order of only a few hundred nanoseconds, it is sufficient to preclude the discrimination of neutron- and gamma-induced pulses for PSD for EJ301, which has principle scintillation time constants of 3.2 and 32 ns.

The proposed solution is to use an extremely fast ($\lesssim 1$ ns) current-sensitive preamplifier that has been recently been developed for photonic readout in medical imaging applications [119]. Figure 8-1 shows the circuit now under development in the laboratory. Successful tests have been carried out with the preamplifier and the next steps should be the evaluation of the circuit with different SiPMs.

8.2.2 Install an in-situ beam target

One of the principle limitations of AGNOSTIC was the lack of *in-situ* diagnosis of the RFQ deuteron beam. While extremely careful alignment and beam spot optimization was conducted before the RFQ was attached to the vacuum vessel, the unequivocal
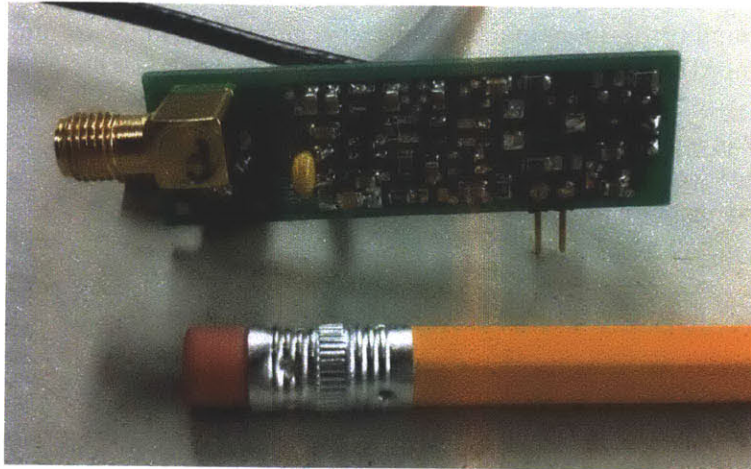
Figure 8-1: A photograph of the fast current preamplifier now under development for the AGNOSTIC EJ301-SiPM neutron detector.

imaging of the beam spot on the inner wall PFCs and direct visual confirmation of the magnetic beam steering would provide a far more substantial degree of confidence than the validation tests presented in Chapter 6. Optical imaging of the beamline would also enable visual optimization of the beam focusing optics and validation of the computational codes currently used to setup the permanent magnetic quadrupole focusing magnets.

A second limitation of AGNOSTIC was the inability to make control measurements of a fully known, unchanging PFC surface inside of Alcator C-Mod. Using a target with both neutron- and gamma-production cross sections would enable validation of the entire experiment in Alcator C-Mod as well as routine energy calibrations of the particle detectors. It would also enable the conversion of the AIMS measurements from *relative* to *absolute* isotopic concentrations. To provide a constant surface composition for measurement, the target should be protected from exposure to plasma conditions by pneumatic shutters that are used for other sensitive invessel equipment.

Both limitations could be simultaneously addressed by installing a dedicated *in-situ* beam target on the inner wall. By careful selection of the target material, bright scintillation light from the incident deuteron beam could be produced for visual beam diagnosis and magnetic steering while neutrons and gammas could be produced for the validating and calibrating the particle detectors. Of the materials considered, Boron Nitride (BN) is probably the most optimal: it scintillates in blue in response to energetic charged particle beams; it has neutron- and gamma-production cross sections (See Chapters 3 and 6); is relatively easily to machine; and is rated for high vacuum fusion applications.

The in-situ target must be designed to be completely nondisruptive to plasma operations, extremely robust, and within view of a visible imaging camera inside the vacuum vessel. An engineering design of *in-situ* target was completed and proposed

for installation as part up the AGNOSTIC upgrade during the FY13 plasma campaign but was not implemented due to the - currently in effect - shutdown of Alcator C-Mod. An image of the design proposed for AGNOSTIC appears in Figure 8-2. For any future AIMS diagnostic, Such a target would substantially enhance the diagnostic optimization, code validation, and measurement capabilities.

8.2.3 Continue developing computational IBA

ACRONYM, the synthetic diagnostic for AIMS on Alcator C-Mod, played a key role in exploring the diagnostic design, optimizing the position of the detectors within the myriad constraints, and providing insight into the experimental detector spectra. In the future, however, it is foreseen that developments underway in the IBA community may enable ACRONYM to extract *absolute* measurements of the PFC surface composition rather than just the relative measurements it is currently capable of obtaining.

The key development in this area is the IAEA-led initiative to utilize developments in computational power and nuclear data productions to replace standards-based IBA with standardless, computational IBA [42]. The nuclear reaction module written for ACRONYM is already capable of simulating the nuclear reactions of interest in AIMS although the dearth of differential angular cross section data is a - hopefully short-lived - hindrance. Cross sections for several of the deuteron-induced nuclear reaction of interest for AIMS are now underway at MIT, and new advances in the analysis of material composition using a combination of the EJ301-PMT detector responses and computational IBA are now being pursued.

8.3 Prospects for AIMS in PMI science

AGNOSTIC on Alcator C-Mod was the first AIMS diagnostic to be implemented on a magnetic fusion device. With the impending shutdown of the Alcator C-Mod tokamak and cessation of plasma operations that followed immediately after the AIMS plasma run on October 2, 2012, AGNOSTIC - the status of Alcator C-Mod remains unclear as of this writing - AGNOSTIC was a novel diagnostic that was given a single opportunity to prove its potential: no upgrades, no second chances, no "do overs." As demonstrated from the measurements and analysis presented in Chapters 6 and 7, as well as those found in [55], AIMS demonstrated its potential to revolutionize PMI science in just one third of a plasma run day on Alcator C-Mod.

For the first time in experimental PMI science, one can imagine routinely producing time-resolved maps of fuel retention, net erosion and deposition, and isotopic composition over a majority of PFC surfaces with a remote-sensing diagnostic that is adaptable to any magnetic fusion device. Such a capability would provide the

139

Inner wall backplate

BN Target

Stainless target holders

Mo PFCs
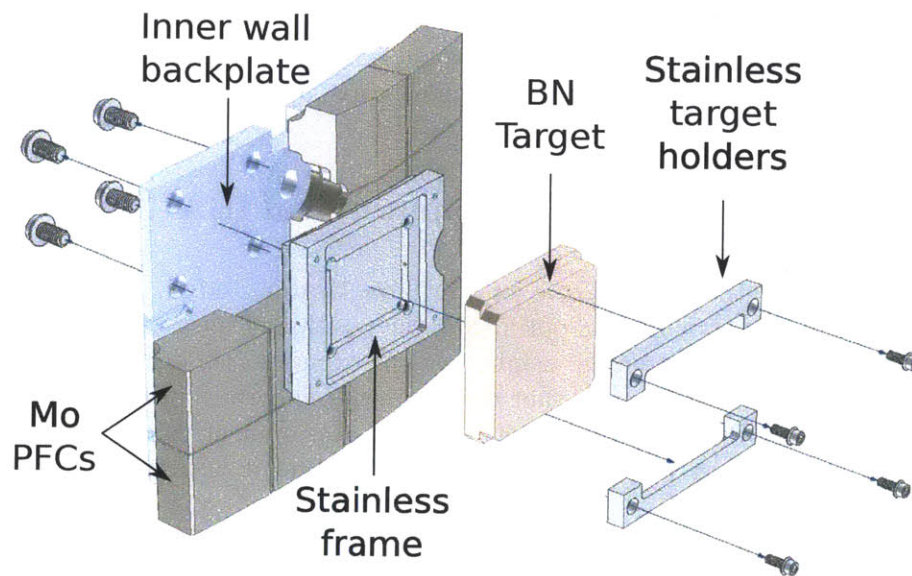
Stainless frame

(a) Exploded view
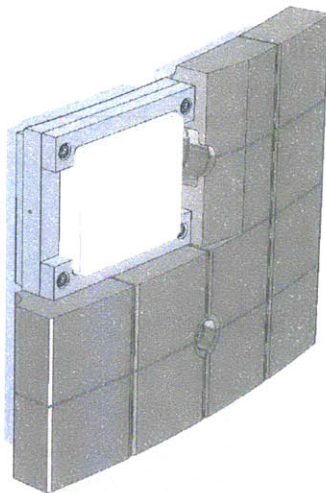
(b) Isometric view

(c) Top-down view

Figure 8-2: The engineering solid model for the AGNOSTIC *in-situ* beam target. The BN target plate is robustly secured in place in a stainless steel frame with two stainless target hold plates; the frame is then bolted to the inner wall backplate module. The BN target extends radially beyond the stainless frame but is set 5 mm behind the radius of the inner wall PFCs to prevent contaminating the plasma. Neighboring PFCs are beveled to prevent the plasma from encountering leading edges.

first true comprehensive look at the dynamic interactions of confined thermonuclear plasma and the plasma-facing boundary materials, integrating centimeter-scale resolution measurements into a true global picture of PMI. The result would be a tremendous advance in experimental PMI science as well as a wealth of experimental data to guide the development and validation of PMI modeling codes that are considered essential for magnetic fusion reactor development.

One of the most exciting prospects for AIMS is the operation of a significantly upgraded AGNOSTIC with the proposed Advanced Outer divertor (AOD) on Alcator C-Mod would have combined the most comprehensive *ex-situ* PFC surface diagnostic with the most forward-looking solution to reactor-relevant PMI issues. The AOD is an approved design for a toroidally continuous, tightly aligned tungsten divertor that operates at initial temperatures up to 875 K in order to understand the impact of high temperature surfaces on PMI, particularly fuel retention, and, in turn, on plasma confinement. AGNOSTIC would be the perfect complement to the AOD, providing time- and space-resolved measurements of the hot tungsten PFC surfaces that could be coupled to the suite of planned plasma and boundary diagnostics.

The successful demonstration of AIMS on Alcator C-Mod holds tremendous potential for the experimental advancement of PMI science in magnetic fusion tokamaks, and a clear path exists for the continued development of the measurements techniques and deployment of diagnostics on other magnetic fusion devices. It is the hope of this author that AIMS becomes one of the standard PMI diagnostics found on every magnetic fusion device and is considered to be one the principal keys in the unlocking of the science of PMI. Ultimately, the proof-of-principle AIMS diagnostic on Alcator C-Mod is analogous to the shore of the cosmic ocean in one of Carl Sagan's most famous quotes, an embodiment of the sentiment that with AIMS "on this shore, we've learned most of what we know. Recently, we've waded a little way out, maybe ankle-deep, and the water seems inviting [120]."

Appendix A

ROOT-based data acquisition and analysis framework

A major challenge of the thesis was to implement a data system that facilitated the collection and analysis of all experimental data, primarily digitized detector and accelerator signals for offline analysis. The bespoke, evolving nature of the experiment demanded an adaptable system that could be custom modified to meet any desired new functionality, which precluded the use of commercial data systems. We also required the ability to run the experiment independently of the tokamak, in order to achieve maximum operational flexibility for equipment debugging, experimental validation, system optimization, and tokamak-independent experiments, as well as to account for a scenario where we needed to move and operate the system in an offsite location. This requirement precluded the use of Alcator C-Mod's preexisting MDSplus[1] data storage framework. Therefore, we decided to develop a custom data acquisition and analysis framework from scratch using ROOT that would be tailored to meet the specific needs of our experiment. The result was a robust, customizable, well-understood framework for acquiring, storing, and analyzing the data that seemlessly integrated into the experiment's data acquisition hardware, which is described in detail in Section . The following section is intended to provide a detailed explanation of the software-side of the data acquisition system.

A.1 ROOT

ROOT[2] is a C++ object-oriented framework conceived at the European Center for Nuclear Research (CERN) developed by the high-energy particle physics community

---

[1]MDSplus is a set of software tools for data acquisition, storage, and management of complex scientific data commonly used in magnetic fusion experiments. Available at http://www.mdsplus.org/index.php/Introduction

[2]ROOT is available at http://root.cern.ch/drupal/

in order to meet the massive data storage and analysis challenges posed by the Large Hadron Collider and other next-generation experiments [60]. It should be noted, however, that despite its principle application in large collider experiments, ROOT provides a comprehensive, cost free, open source, and immensely powerful framework for almost any small- and mid-size physics experiment. ROOT contains an efficient object-orient database for parallel data writing/reading, advanced statistical analysis methods (multidimensional histogramming, data fitting packages, peak finding algorithms, etc), data visualization tools, a C++ interpreter environment for dynamic access to the ROOT framework, and a large toolkit of C++ classes that can be folded into the user's custom C++ code. Of particular interest to the development of our experiment, ROOT provides the ability to construct complex graphical user interfaces (GUI) by using either the native ROOT GUI environment or by integrating the ROOT framework into a Qt-based project.

A.2 Overview

The purpose of the data acquisition framework is threefold: first, it must allow the user to program and operate the the DAQ hardware; second, it must enable the user to acquire digitized data and store in persistently onto a hard drive; third, it must provide the user with the ability to access and analyze the data after the experiment has concluded.

An overview of the data acquisition framework is shown in figure X. In order to augment their data acquisition hardware, Caen provides firmware and a set of C libraries that provide for a basic interface to and control of the data hardware, which forms the foundation of the data acquisition framework. The next layer consists of the custom **ADAQ** library that uses the CAEN C libraries to provide a high-level interface to each piece of hardware for intuitive control and maximum data acquisition functionality, as well as "wrapper" functions using **Boost.Python**[3] to enable **Python** control of the hardware. Next, (**ADAQAcquisition**) is built on top of the **ADAQ** library. As described in the following section, it provides the user full control of the DAQ hardware, real time viewing and data analysis, and persistent storage of digitized waveforms via the ROOT file input/output framework. Finally, as described in Section A.3, **ADAQAnalysis** enables access to the stored ROOT files and provides comprehensive examination, analysis, and visualization, of the data stored in them.

Finally, it should be noted that combining the high-level **ADAQ** library with the tools provided by CAEN results in a flexible development platform that extends beyond **ADAQAcquisition** and **ADAQAnalysis**. For example, a number of ADAQ applications, using **C++** and **Python** to perform simple tasks from the command line and in batch mode, have been developed, as well as a prototype ADAQ interface to the **MDSplus** data system. Furthermore, the user can use these tools to develop new graphical

---

[3]**Boost.Python** is available at http://www.boost.org/doc/libs/1_53_0/libs/python/doc/index.html

interfaces using `Python`, `Qt`, or other application of their choosing.

A.3 Acquisition tools

`ADAQAcquisition` is a standalone, graphical user interface for ADAQ that is built primarily with custom C++ classes and the native ROOT GUI environment. Its main purposes is to enable the user to effortlessly acquire and store digitized data using ADAQ; it has the additional benefit of obscuring the low-level details of accessing the DAQ hardware and using ROOT file input/output, which enables any user, regardless of programming experience, to successfully use ADAQ. Its main features are to

- establish a connection to the ADAQ system

- read/write values to any register on the ADAQ hardware

- set, operate, and monitor of the ADAQ high voltage supply

- set, operate, and monitor of the ADAQ digitizers

- provide a real-time digital oscilloscope

- perform real-time analysis of digitized waveforms into spectra

- output publication-quality images of waveforms, detector spectra

- store digitized waveforms persistenly in ROOT files

The main window frame of `ADAQAcquisition` provides tabbed access to three main subframes: the "VME Connection" tab contains general DAQ functions; the "High Voltage" tab contains all voltage supply functions; and the "Oscilloscope" tab contains all of the real-time acquisition, analysis, and data storage functions. A screenshot of `ADAQAcquisition`, with the "Oscillocope" tab displaying an acquired detector waveform, is shown below:

A.4 Analysis tools

Similar to `ADAQAcquisition`, `ADAQAnalysis` is a standalone, graphical user interface for ADAQ that is built primarily with custom C++ classes and the native ROOT GUI environment. Its main purpose is to provide the user with an intuitive, powerful engine that streamlines the process of ADAQ data analysis while at the same time obscuring the underlying ROOT file storage architecture and input/output methods. Its main features are to provide

145
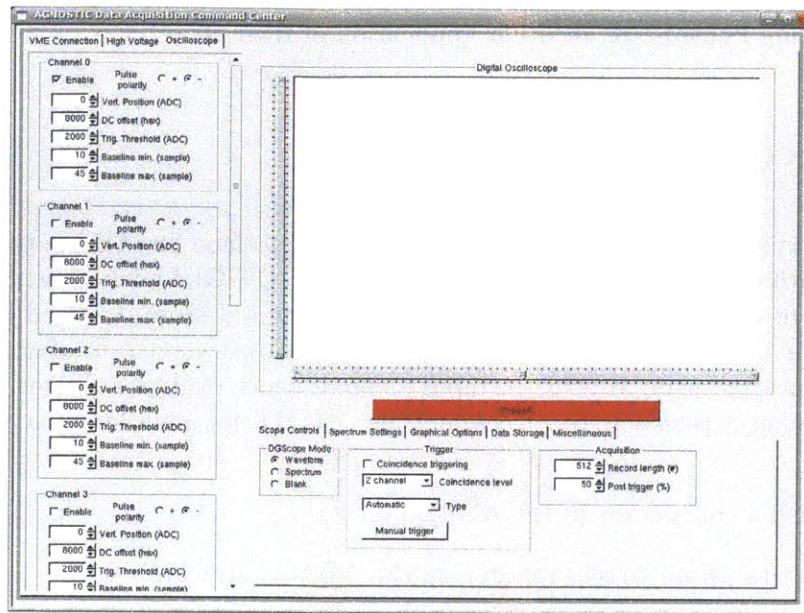
- seemless access to ADAQ data stored in ROOT files
- comprehensive inspection of digitized waveforms
- various algorithms for operations on waveforms
  - peak finding
  - pulse pileup rejection
  - spectra creation
  - pulse shape discrimination
  - pulse desplicing
- various algorithms for operations on spectra
  - spectra calibration
  - peak finding
  - peak fitting
  - background estimation and subtraction
  - spectra and peak integration
- calculation of detector count rates
- calculation of incident deuterons on target from RFQ current
- generation of publication-quality images of analyzed data

In addition, because many of the digital operations on waveforms are embarassingly parallel, **ADAQAnalysis** has been parallelized using Open MPI[4], which greatly reduces processing time for CPU-expensive tasks like peak finding and spectra creation on large data sets.

As for **ADAQAcquisition**, the main window of **ADAQAnalysis** provides tabbed access to five main subframes. The "Waveform" and "Spectrum" tab provide settings for

---

[4]Open MPI is an open source implemention of the MPI2 (Message Passing Interface) standards. Available at http://www.open-mpi.org/

creating and analyzing these objects, while the "Analysis" tab provides settings for various waveform analysis algorithms, such as pulse shape discrimination and count rate calculation. The "Graphics" tab handles the creation and output of graphical results, and the "Processing" tab controls sequential or parallel waveform handling and other features. A screenshot of `ADAQAnalysis`, showing a two-dimensional histogram containing the result of a pulse shape discrimination algorithm, is shown below:
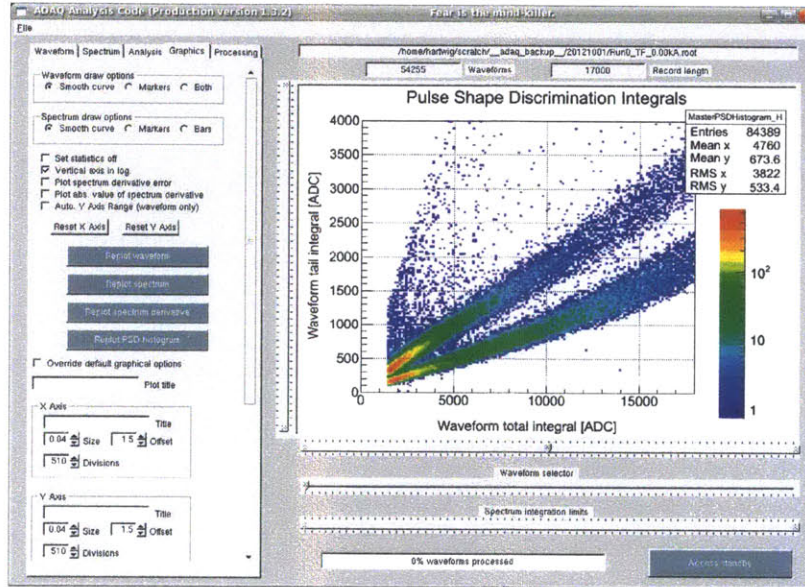
References

[1] R. Toschi. Nuclear fusion, an energy source. *Fusion Engineering and Design*, 36(1):1 – 8, 1997. ISSN 0920-3796. doi:10.1016/S0920-3796(97)00007-0.

[2] M. Greenwald, R. Callis, D., W. Dorland, D. Gates, J. Harris, R. Linford, M. Mauel, K. McCarthy, D. Meade, F. Najmabadi, W. Nevins, J. Sarff, M. Ulrickson, M. Zarnstorff, and S. Zinkle. Priorities, gaps and opportunities: Towards a long-range strategic plan for magnetic fusion energy. *FESAC Report DOE/SC-0102*, 2007. URL http://www.science.doe.gov/ofes/FESAC/Oct-2007/FESAC_Planning_Report.pdf.

[3] I. H. Hutchinson. *Principles of Plasma Diagnostics*. Cambridge University Press, Cambridge, 2005.

[4] G. Federici, C.H. Skinner, J.N. Brooks, J.P. Coad, C. Grisolia, A.A. Haasz, A. Hassanein, V. Philipps, C.S. Pitcher, J. Roth, W.R. Wampler, and D.G. Whyte. Plasma-material interactions in current tokamaks and their implications for next step fusion reactors. *Nuclear Fusion*, 41(12):1967, 2001. URL http://stacks.iop.org/0029-5515/41/i=12/a=218.

[5] Z. S. Hartwig, H. S. Barnard, B. N. Sorbom, R. C. Lanza, P. W. Stahle, and D. G. Whyte. An accelerator-based diagnostic for plasma-material interactions science on magnetic fusion devices. *Review of Scientific Instuments*, 2013. Accepted for publication; In press.

[6] Z. S. Hartwig and P. Gumplinger. Simulating response functions and pulse shape discrimination for organic scintillation detectors with Geant4. *Nuclear Instruments and Methods in Physics Research Section A: Accelerators, Spectrometers, Detectors and Associated Equipment*, 2013. ISSN 0168-9002. doi:10.1016/j.nima.2013.11.027. Accepted for publication; In press.

[7] Lyman Spitzer. Report NYO-993 (PM-S-1). *U.S. Atomic Energy Comission*, 1951.

[8] H.F. Dylla, M. Ulrickson, M.G. Bell, D.K. Owens, D. Buchenauer, R.V. Budny, K.W. Hill, S.J. Kilpatrick, D.M. Manos, P.H. LaMarche, A.T. Ramsey, G.L. Schmidt, and M. Zarnstorff. First-wall conditioning for enhanced confinement discharges and the DT experiments in TFTR. *Journal of Nuclear Materials*, 162164(0):128 – 137, 1989. ISSN 0022-3115. doi:10.1016/0022-3115(89)90263-8.

[9] B. Lipschultz, Y. Lin, M. L. Reinke, A. Hubbard, I. H. Hutchinson, J. Irby, B. LaBombard, E. S. Marmar, K. Marr, J. L. Terry, S. M. Wolfe, the Alcator C-Mod group, and D. Whyte. Operation of Alcator C-Mod with high-Z plasma facing components and implications. *Physics of Plasmas*, 13(5):056117, 2006. doi:10.1063/1.2180767.

[10] Peter C. Stangeby. *The Plasma Boundary of Magnetic Fusion Devices*. Taylor & Francis, 2000.

[11] G.M. Olynyk, Z.S. Hartwig, D.G. Whyte, H.S. Barnard, P.T. Bonoli, L. Bromberg, M.L. Garrett, C.B. Haakonsen, R.T. Mumgaard, and Y.A. Podpaly. Vulcan: A steady-state tokamak for reactor-relevant plasmamaterial interaction science. *Fusion Engineering and Design*, 87(3):224 – 233, 2012. ISSN 0920-3796. doi:10.1016/j.fusengdes.2011.12.009. Special Section on Vulcan Conceptual Design.

[12] B. D. Wirth, K. Nordlund, D.G. Whyte, and D. Xu. Fusion materials modeling: challenges and opportunities. *Materials Research Society Bulletin*, 36:216–222, 2011. doi:10.1557/mrs.2011.37.

[13] G.V. Kidson. 9.2 Methods of measurements of diffusion coefficients of hydrogen in metals. 26:504–509, 1990. doi:10.1007/10390457_93.

[14] D. Nishijima, T. Sugimoto, H. Iwakiri, M.Y. Ye, N. Ohno, N. Yoshida, and S. Takamura. Characteristic changes of deuterium retention on tungsten surfaces due to low-energy helium plasma pre-exposure. *Journal of Nuclear Materials*, 337339(0):927 – 931, 2005. ISSN 0022-3115. doi:10.1016/j.jnucmat.2004.10.011. PSI-16.

[15] M. A. Abdou, E. L. Vold, C. Y. Gung, M. Z. Youssef, and K. Shin. Deuterium-tritium fuel self-sufficiency in fusion reactors. *Fusion Technology*, 9:250 – 285, 1985.

[16] A.W. Leonard, A. Herrmann, K. Itami, J. Lingertat, A. Loarte, T.H. Osborne, W. Suttrop, the ITER Divertor Modeling, Database Expert Group, and the ITER Divertor Physics Expert Group. The impact of ELMs on the ITER divertor. *Journal of Nuclear Materials*, 266269(0):109 – 117, 1999. ISSN 0022-3115. doi:10.1016/S0022-3115(98)00522-4.

[17] A. Hassanein. *Fusion Technology*, 15, 1989.

[18] G. Federici, A. Loarte, and G. Strohmayer. Assessment of erosion of the ITER divertor targets during type I ELMs. *Plasma Physics and Controlled Fusion*, 45(9):1523, 2003. URL http://stacks.iop.org/0741-3335/45/i=9/a=301.

[19] D.G. Whyte, J.P. Coad, P. Franzen, and H. Maier. Similarities in divertor erosion/redeposition and deuterium retention patterns between the tokamaks ASDEX Upgrade, DIII-D and JET. *Nuclear Fusion*, 39(8):1025, 1999. URL http://stacks.iop.org/0029-5515/39/i=8/a=306.

[20] R. A. Pitts, J. P. Coad, D. P. Coster, G. Federici, W. Fundamenski, J. Horacek, K. Krieger, A. Kukushkin, J. Likonen, G. F. Matthews, M. Rubel, J. D. Strachan, and JET-EFDA contributors. Material erosion and migration in tokamaks. *Plasma Physics and Controlled Fusion*, 47(12B):B303, 2005. URL http://stacks.iop.org/0741-3335/47/i=12B/a=S22.

[21] H. W. Kugel, M. G. Bell, J.-W. Ahn, J. P. Allain, R. Bell, J. Boedo, C. Bush, D. Gates, T. Gray, S. Kaye, R. Kaita, B. LeBlanc, R. Maingi, R. Majeski, D. Mansfield, J. Menard, D. Mueller, M. Ono, S. Paul, R. Raman, A. L. Roquemore, P. W. Ross, S. Sabbagh, H. Schneider, C. H. Skinner, V. Soukhanovskii, T. Stevenson, J. Timberlake, W. R. Wampler, and L. Zakharov. The effect of lithium surface coatings on plasma performance in the national spherical torus experiment. *Physics of Plasmas*, 15(5):056118, 2008. doi:10.1063/1.2906260.

[22] R. Behrisch, M. Mayer, and C. Garca-Rosales. Composition of the plasma facing material tokamakium. *Journal of Nuclear Materials*, 233237, Part 1(0): 673 – 680, 1996. ISSN 0022-3115. doi:10.1016/S0022-3115(96)00144-4.

[23] G. Federici. Plasma wall interactions in ITER. *Physica Scripta*, 2006(T124):1, 2006. URL http://stacks.iop.org/1402-4896/2006/i=T124/a=001.

[24] M. Psoda, M. Rubel, G. Sergienko, P. Sundelin, and A. Pospieszczyk. Material mixing on plasma-facing components: Compound formation. *Journal of Nuclear Materials*, 386388(0):740 – 743, 2009. ISSN 0022-3115. doi:10.1016/j.jnucmat.2008.12.206. Proceedings of the Thirteenth International Conference on Fusion Reactor Materials.

[25] G.F. Counsell, J.P. Coad, G. Federici, K. Krieger, V. Philipps, C.H. Skinner, and D.G. Whyte. Towards an improved understanding of the relationship between plasma edge and materials issues in a next-step fusion device. *Journal of Nuclear Materials*, 290293(0):255 – 259, 2001. ISSN 0022-3115. doi:10.1016/S0022-3115(00)00626-7. 14th Int. Conf. on Plasma-Surface Interactions in Controlled Fusion Devices.

[26] M. Rubel, J.P. Coad, and D. Hole. Accelerator-based ion beam analysis of fusion reactor materials. *Vacuum*, 78(24):255 – 261, 2005. ISSN 0042-207X. doi:10.1016/j.vacuum.2005.01.109. Proceedings of the fifth International Conference on Ion Implantation and other Applications of Ions and Electrons (ION 2004).

[27] G.M. Wright, H. S. Barnard, Z. S. Hartwig, P.W. Stahle, R.M. Sullivan, K.B. Woller, and D.G. Whyte. Plasma-surface Interaction research at The Cambridge Laboratory of Accelerator Studies of Surfaces. 1336:626, 2011.

[28] F. Anabitarte, A. Cobo, and J. M. Lopez-Higuera. Laser-induced breakdown spectroscopy: Fundamentals, applications, and challenges. *ISRN Spectroscopy*, 2012(Article ID 285240):1–12, 2012. doi:doi:10.5402/2012/285240.

151

[29] M. Zlobinski, V. Philipps, B. Schweer, A. Huber, H. Stoschus, S. Brezinsek, U. Samm, and the TEXTOR team. In situ measurements of fuel retention by laser induced desorption spectroscopy in TEXTOR. *Physica Scripta*, 2011(T145):014027, 2011. URL http://stacks.iop.org/1402-4896/2011/i=T145/a=014027.

[30] Q. Xiao, A. Huber, G. Sergienko, B. Schweer, Ph. Mertens, A. Kubina, V. Philipps, and H. Ding. Application of laser-induced breakdown spectroscopy for characterization of material deposits and tritium retention in fusion devices. *Fusion Engineering and Design*, (0):–, 2013. ISSN 0920-3796. doi:10.1016/j.fusengdes.2013.05.083.

[31] B. Schweer, F. Irrek, G. Sergienko, V. Philipps, and U. Samm. In situ diagnostic for monitoring of deuterium and tritium in re-deposited carbon layers by laser induced desorption. *Journal of Nuclear Materials*, 363365(0):1375 – 1379, 2007. ISSN 0022-3115. doi:10.1016/j.jnucmat.2007.01.247. Plasma-Surface Interactions-17.

[32] P. Franzen, R. Behrisch, C. Garcia-Rosales, D. Schleussner, D. Rosler, J. Becker, W. Knapp, and C. Edelmann. Hydrogen isotope inventory in the graphite divertor tiles of ASDEX Upgrade as measured by thermal desorption spectroscopy. *Nuclear Fusion*, 37(10):1375, 1997. URL http://stacks.iop.org/0029-5515/37/i=10/a=I05.

[33] H.G. Esser, V. Philipps, M. Freisinger, G.F. Matthews, J.P. Coad, and G.F. Neill. Effect of plasma configuration on carbon migration measured in the inner divertor of jet using quartz microbalance. *Journal of Nuclear Materials*, 337339(0):84 – 88, 2005. ISSN 0022-3115. doi:10.1016/j.jnucmat.2004.10.112. PSI-16.

[34] C.H. Skinner, H. Kugel, A.L. Roquemore, J. Hogan, and W.R. Wampler. Time resolved deposition measurements in NSTX. *Journal of Nuclear Materials*, 337339(0):129 – 133, 2005. ISSN 0022-3115. doi:10.1016/j.jnucmat.2004.10.076. PSI-16.

[35] F. Weschenfelder, G. L. Jackson, P. Wienhold, J. Winter, N. H. Brooks, W. P. West, and R. Lee. In situ measurement of erosion/deposition in the diii-d divertor by colorimetry. *Plasma Physics and Controlled Fusion*, 38(7):1043, 1996. URL http://stacks.iop.org/0741-3335/38/i=7/a=009.

[36] D. G. Whyte. Plasma-surface interaction studies on DIII-D and their implications for next-step fusion experiments. *Fusion Science and Technology*, 48(2): 1096, 2005.

[37] C.P.C. Wong, D.L. Rudakov, J.P. Allain, R.J. Bastasz, N.H. Brooks, J.N. Brooks, R.P. Doerner, T.E. Evans, A. Hassanein, W. Jacob, K. Krieger, A. Litnovsky, A.G. McLean, V. Philipps, A.Yu. Pigarov, W.R. Wampler, J.G. Watkins, W.P. West, J. Whaley, and P. Wienhold. Divertor and midplane materials evaluation system in diii-d. *Journal of Nuclear Materials*, 363365(0):276 –

281, 2007. ISSN 0022-3115. doi:10.1016/j.jnucmat.2007.01.121. Plasma-Surface Interactions-17.

[38] D.D.R. Summers, M.N.A. Beurskens, J.P. Coad, G. Counsell, W. Fundamenski, G.F. Matthews, and M.F. Stamp. In situ measurement of hydrogen retention in jet carbon tiles. *Journal of Nuclear Materials*, 290293(0):496 – 500, 2001. ISSN 0022-3115. doi:10.1016/S0022-3115(00)00481-5. 14th Int. Conf. on Plasma-Surface Interactions in Controlled Fusion Devices.

[39] B. Schweer, F. Irrek, M. Zlobinski, A. Huber, G. Sergienko, S. Brezinsek, V. Philipps, and U. Samm. In situ detection of hydrogen retention in TEXTOR by laser induced desorption. *Journal of Nuclear Materials*, 390391(0):576 – 580, 2009. ISSN 0022-3115. doi:10.1016/j.jnucmat.2009.01.108. Proceedings of the 18th International Conference on Plasma-Surface Interactions in Controlled Fusion Devices.

[40] A. Huber, B. Schweer, V. Philipps, R. Leyte-Gonzales, N. Gierse, M. Zlobinski, S. Brezinsek, V. Kotov, P. Mertens, U. Samm, and G. Sergienko. Study of the feasibility of applying laser-induced breakdown spectroscopy for in-situ characterization of deposited layers in fusion devices. *Physics Scripta*, T145:1 – 5, 2011. doi:10.1088/0031-8949/2011/T145/014028.

[41] Y. Wang and M. Nastasi, editors. *Handbook of Modern Ion Beam Materials Analysis*. Materials Research Society, Warrendale, PA, 2 edition, 2010.

[42] D. Abriola and A. P. de Jesus. Development of a reference database for particle induced gamma ray emission (PIGE) spectroscopy. *IAEA International Nuclear Data Committee Report INDC(NDS)-0589*, 2011.

[43] R. H. Stokes and T. P. Wangler. Radiofrequency quadrupole accelerators and their applications. *Annual Review of Nuclear and Particle Science*, 38(1):97–118, 1988. doi:10.1146/annurev.ns.38.120188.000525.

[44] D.J. Herbert, N. DAscenzo, N. Belcari, A. Del Guerra, F. Morsani, and V. Saveliev. Study of SiPM as a potential photodetector for scintillator readout. *Nuclear Instruments and Methods in Physics Research Section A: Accelerators, Spectrometers, Detectors and Associated Equipment*, 567(1):356 – 359, 2006. ISSN 0168-9002. doi:10.1016/j.nima.2006.05.143. Proceedings of the 4th International Conference on New Developments in Photodetection.

[45] M. Deutsch. Angular correlations in nuclear reactions. *Reports on Progress in Physics*, 14(1):196, 1951. URL http://stacks.iop.org/0034-4885/14/i=1/a=307.

[46] Z. Elekes, .Z. Kiss, I. Biron, T. Calligaro, and J. Salomon. Thick target gamma-ray yields for light elements measured in the deuteron energy interval of 0.73.4 MeV. *Nuclear Instruments and Methods in Physics Research Section B: Beam*

Interactions with Materials and Atoms, 168(3):305 – 320, 2000. ISSN 0168-583X. doi:10.1016/S0168-583X(99)01003-4.

[47] G.. Sziki, A. Simon, Z. Szikszai, Zs. Kertsz, and E. Dobos. Gamma ray production cross-sections of deuteron induced nuclear reactions for light element analysis. *Nuclear Instruments and Methods in Physics Research Section B: Beam Interactions with Materials and Atoms*, 251(2):343 – 351, 2006. ISSN 0168-583X. doi:10.1016/j.nimb.2006.07.008.

[48] Oakes Ames, George E. Owen, and C. D. Swartz. Angular Distributions of the $B^{11}(d, n)C^{12}$ Ground-State Neutrons. *Phys. Rev.*, 106:775–778, May 1957. doi:10.1103/PhysRev.106.775.

[49] M.B. Chadwick, M. Herman, P. Obloinsk, M.E. Dunn, Y. Danon, A.C. Kahler, D.L. Smith, B. Pritychenko, G. Arbanas, R. Arcilla, R. Brewer, D.A. Brown, R. Capote, A.D. Carlson, Y.S. Cho, H. Derrien, K. Guber, G.M. Hale, S. Hoblit, S. Holloway, T.D. Johnson, T. Kawano, B.C. Kiedrowski, H. Kim, S. Kunieda, N.M. Larson, L. Leal, J.P. Lestone, R.C. Little, E.A. McCutchan, R.E. MacFarlane, M. MacInnes, C.M. Mattoon, R.D. McKnight, S.F. Mughabghab, G.P.A. Nobre, G. Palmiotti, A. Palumbo, M.T. Pigni, V.G. Pronyaev, R.O. Sayer, A.A. Sonzogni, N.C. Summers, P. Talou, I.J. Thompson, A. Trkov, R.L. Vogt, S.C. van der Marck, A. Wallner, M.C. White, D. Wiarda, and P.G. Young. Endf/b-vii.1 nuclear data for science and technology: Cross sections, covariances, fission product yields and decay data. *Nuclear Data Sheets*, 112(12): 2887 – 2996, 2011. ISSN 0090-3752. doi:10.1016/j.nds.2011.11.002. Special Issue on ENDF/B-VII.1 Library.

[50] R.W. Michelmann, J. Krauskopf, J.D. Meyer, and K. Bethge. Excitation functions for the reactions 10B(d, n)11C and 12C(d, n)13N for charged particle activation analysis. *Nuclear Instruments and Methods in Physics Research Section B: Beam Interactions with Materials and Atoms*, 51(1):1 – 4, 1990. ISSN 0168-583X. doi:10.1016/0168-583X(90)90530-8.

[51] A. E. Kempton, B. C. Browne, and R. Maasdorp. Angular distributions of the protons and neutrons emitted in some transmutations of deuterium. *Proceedings of the Royal Society of London. Series A - Mathematical and Physical Sciences*, 157(891):386–399, 1936. doi:10.1098/rspa.1936.0202.

[52] A.A. Haasz and J.W. Davis. Deuterium retention in beryllium, molybdenum and tungsten at high fluences. *Journal of Nuclear Materials*, 241243(0):1076 – 1081, 1997. ISSN 0022-3115. doi:10.1016/S0022-3115(97)80197-3.

[53] G. F. Knoll. *Radiation Detection and Measurement*. Wiley, 2000.

[54] James F. Ziegler, M.D. Ziegler, and J.P. Biersack. SRIM - The stopping and range of ions in matter (2010). *Nuclear Instruments and Methods in Physics Research Section B: Beam Interactions with Materials and Atoms*, 268(11-12):

1818 – 1823, 2010. ISSN 0168-583X. doi:10.1016/j.nimb.2010.02.091. 19th International Conference on Ion Beam Analysis.

[55] Harold S Barnard. *Unknown title as of this writing*. PhD thesis, Massachusetts Institute of Technology, 2013.

[56] I. H. Hutchinson, R. Boivin, F. Bombarda, P. Bonoli, S. Fairfax, C. Fiore, J. Goetz, S. Golovato, R. Granetz, M. Greenwald, S. Horne, A. Hubbard, J. Irby, B. LaBombard, B. Lipschultz, E. Marmar, G. McCracken, M. Porkolab, J. Rice, J. Snipes, Y. Takase, J. Terry, S. Wolfe, C. Christensen, D. Garnier, M. Graf, T. Hsu, T. Luke, M. May, A. Niemczewski, G. Tinios, J. Schachter, and J. Urbahn. First results from Alcator-C-Mod. *Physics of Plasmas*, 1(5):1511–1518, 1994. doi:10.1063/1.870701.

[57] F. Romanelli and JET EFDA Contributors. Overview of the JET results with the ITER-like wall. *Nuclear Fusion*, 53(10):104002, 2013. URL http://stacks.iop.org/0029-5515/53/i=10/a=104002.

[58] B. Lipschultz, B. LaBombard, J.L. Terry, and I.H. Hutchinson. Divertor physics research in Alcator C-Mod. *MIT Plasma Science and Fusion Center Reports*, PSFC/JA-05-38, 2005.

[59] N. P. Basse A. Dominguez E. M. Edlund C. L. Fiore R. S. Granetz A. E. Hubbard J. W. Hughes I. H. Hutchinson J. H. Irby B. LaBombard L. Lin Y. Lin B. Lipschultz J. E. Liptac E. S. Marmar D. A. Mossessian R. R. Parker M. Porkolab J. E. Rice J. A. Snipes V. Tang J. L. Terry S. M. Wolfe S. J. Wukitch K. Zhurovich R. V. Bravenec P. E. Phillips W. L. Rowan G. J. Kramer G. Schilling S. D. Scott S. J. Zweben. Diagnostic systems on Alcator C-Mod. *Fusion Science and Technology*, 51(3):476–507, 2007.

[60] R. Brun and F. Rademakers. ROOT - An object-oriented data analysis framework. *Nuclear Instruments and Methods in Physics Research Section A: Accelerators, Spectrometers, Detectors and Associated Equipment*, 389:81–86, 1997.

[61] Eljen Technology Inc. EJ-301 Liquid Scintillator Data Sheet. 2013. URL http://www.eljentechnology.com.

[62] F. T. Kuchnir and F. J. Lynch. Time dependence of scintillations and the effect on pulse-shape discrimination. *Nuclear Science, IEEE Transactions on*, 15(3):107–113, 1968. ISSN 0018-9499. doi:10.1109/TNS.1968.4324923.

[63] V.V. Filchenkov, A.D. Konin, and V.G. Zinov. Study of the parameters of a long NE213 scintillator counter. *Nuclear Instruments and Methods in Physics Research Section A: Accelerators, Spectrometers, Detectors and Associated Equipment*, 245(23):490 – 494, 1986. ISSN 0168-9002. doi:10.1016/0168-9002(86)91286-6.

155

[64] G. Ranucci, A. Goretti, and P. Lombardi. Pulse-shape discrimination of liquid scintillators. *Nuclear Instruments and Methods in Physics Research Section A: Accelerators, Spectrometers, Detectors and Associated Equipment*, 412(23):374 – 386, 1998. ISSN 0168-9002. doi:10.1016/S0168-9002(98)00456-2.

[65] H. Klein and S. Neumann. Neutron and photon spectrometry with liquid scintillation detectors in mixed fields. *Nuclear Instruments and Methods in Physics Research Section A: Accelerators, Spectrometers, Detectors and Associated Equipment*, 476(12):132 – 142, 2002. ISSN 0168-9002. doi:10.1016/S0168-9002(01)01410-3. Int. Workshop on Neutron Field Spectrometry in Science, Technology and Radiation Protection.

[66] A. Zimbal, H. Klein, M. Reginatto, H. Schuhmacher, L. Bertalot, and A. Murari. High resolution neutron spectrometry with liquid scintillation detectors for fusion applications. *Proceedings of International Workshop on Fast Neutron Detectors and Applications*, PoS, 2006.

[67] V.V. Verbinski, W.R. Burrus, T.A. Love, W. Zobel, N.W. Hill, and R. Textor. Calibration of an organic scintillator for neutron spectrometry. *Nuclear Instruments and Methods*, 65(1):8 – 25, 1968. ISSN 0029-554X. doi:10.1016/0029-554X(68)90003-7.

[68] R.A. Cecil, B.D. Anderson, and R. Madey. Improved predictions of neutron detection efficiency for hydrocarbon scintillators from 1 MeV to about 300 MeV. *Nuclear Instruments and Methods*, 161(3):439 – 447, 1979. ISSN 0029-554X. doi:10.1016/0029-554X(79)90417-8.

[69] A. Aksoy, A. Coban, A.A. Naqvi, F.Z. Khiari, J.M. Hanly, C.R. Howell, W. Tornow, P.D. Felsher, M.A. Al-Ohali, and R.L. Walter. Response-function measurement of an NE213 scintillator using the 2H(d, n)3He reaction. *Nuclear Instruments and Methods in Physics Research Section A: Accelerators, Spectrometers, Detectors and Associated Equipment*, 337(23):486 – 491, 1994. ISSN 0168-9002. doi:10.1016/0168-9002(94)91118-5.

[70] N.P. Hawkes, J.M. Adams, D.S. Bond, S. Croft, O.N. Jarvis, and N. Watkins. Measurements of the proton light output function of the organic liquid scintillator NE213 in several detectors. *Nuclear Instruments and Methods in Physics Research Section A: Accelerators, Spectrometers, Detectors and Associated Equipment*, 476(12):190 – 194, 2002. ISSN 0168-9002. doi:10.1016/S0168-9002(01)01429-2. Int. Workshop on Neutron Field Spectrometry in Science, Technology and Radiation Protection.

[71] M. Gohil, K. Banerjee, S. Bhattacharya, C. Bhattacharya, S. Kundu, T.K. Rana, G. Mukherjee, J.K. Meena, R. Pandey, H. Pai, T.K. Ghosh, A. Dey, S. Mukhopadhyay, D. Pandit, S. Pal, S.R. Banerjee, and T. Bandhop. Measurement and simulation of neutron response function of organic liquid scintillator detector. *Nuclear Instruments and Methods in Physics Research Section*

A: Accelerators, Spectrometers, Detectors and Associated Equipment, 664(1): 304 – 309, 2012. ISSN 0168-9002. doi:10.1016/j.nima.2011.10.054.

[72] K.F. Flynn, L.E. Glendenin, E.P. Steinberg, and P.M. Wright. Pulse height-energy relations for electrons and alpha particles in a liquid scintillator. *Nuclear Instruments and Methods*, 27(1):13 – 17, 1964. ISSN 0029-554X. doi:10.1016/0029-554X(64)90129-6.

[73] G. Dietze and H. Klein. Gamma-calibration of NE213 scintillation counters. *Nuclear Instruments and Methods in Physics Research*, 193(3):549 – 556, 1982. ISSN 0167-5087. doi:10.1016/0029-554X(82)90249-X.

[74] Y. Kaschuck and B. Esposito. Neutron-gamma ray digital pulse shape discrimination with organic scintillators. *Nuclear Instruments and Methods in Physics Research Section A: Accelerators, Spectrometers, Detectors and Associated Equipment*, 551(23):420 – 428, 2005. ISSN 0168-9002. doi:10.1016/j.nima.2005.05.071.

[75] International Standard Organization. Reference Neutron Radiations Part I: Characteristics and Methods of Production. *ISO/DIS 8529-1*, 2000.

[76] C.E. Brient, C.E. Nelson, and R.L. Young. Pulse shape analyzer for fast neutron-gamma ray discrimination. *Nuclear Instruments and Methods*, 98(2): 329 – 333, 1972. ISSN 0029-554X. doi:10.1016/0029-554X(72)90114-0.

[77] J. Flamanc and C. Rozsa. Compact LaBr3:Ce gamma ray detector with Si-APD readout. *AIP Conference Proceedings*, 1099(1):79–83, 2009. doi:10.1063/1.3120159.

[78] R. Hofstadter. Alkali halide scintillation counters. *Phys. Rev.*, 74:100–101, Jul 1948. doi:10.1103/PhysRev.74.100.

[79] O. Guillot-Nol, J.T.M. de Haas, P. Dorenbos, C.W.E. van Eijk, K. Krmer, and H.U. Gdel. Optical and scintillation properties of cerium-doped LaCl3, LuBr3 and LuCl3. *Journal of Luminescence*, 85(13):21 – 35, 1999. ISSN 0022-2313. doi:10.1016/S0022-2313(99)00063-0.

[80] E. V. D. van Loef, P. Dorenbos, C. W. E. van Eijk, K. Kramer, and H. U. Gudel. High-energy-resolution scintillator: Ce^{3+} activated $LaCl_3$. *Applied Physics Letters*, 77(10):1467–1468, 2000. doi:10.1063/1.1308053.

[81] Saint-Gobain Crystals. BrilLanCe 380 $LaBr_3$(Ce) Scintillation Material Datasheet. 2013. URL http://www.detectors.saint-gobain.com.

[82] A. Iltis, M.R. Mayhugh, P. Menge, C.M. Rozsa, O. Selles, and V. Solovyev. Lanthanum halide scintillators: Properties and applications. *Nuclear Instruments and Methods in Physics Research Section A: Accelerators, Spectrometers, Detectors and Associated Equipment*, 563(2):359 – 363, 2006. ISSN 0168-9002. doi:10.1016/j.nima.2006.02.192.

[83] C. Cazzaniga, G. Croci, L. Giacomelli, G. Grosso, M. Nocente, M. Tardocchi, G. Gorini, and A. Weller. LaBr$_3$ scintillator response to admixed neutron and fluxes. *Nuclear Instruments and Methods in Physics Research Section A: Accelerators, Spectrometers, Detectors and Associated Equipment*, (0):–, 2013. ISSN 0168-9002. doi:10.1016/j.nima.2013.05.055.

[84] M. S. Alekhin, J. T. M. de Haas, I. V. Khodyuk, K. W. Kramer, P. R. Menge, V. Ouspenski, and P. Dorenbos. Improvement of gamma-ray energy resolution of LaBr$_3$:Ce^{3+} scintillation detectors by Sr^{2+} and Ca^{2+} co-doping. *Applied Physics Letters*, 102(16):161915, 2013. doi:10.1063/1.4803440.

[85] Helmut Wiedemann. *Particle Accelerator Physics*. Springer London, Limited, 2007.

[86] S. Humphries and S. Humphries Jr. *Charged Particle Beams*. Dover Publications, 2013.

[87] S. Agostinelli, J. Allison, K. Amako, J. Apostolakis, H. Araujo, P. Arce, M. Asai, D. Axen, S. Banerjee, G. Barrand, F. Behner, L. Bellagamba, J. Boudreau, L. Broglia, A. Brunengo, H. Burkhardt, S. Chauvie, J. Chuma, R. Chytracek, G. Cooperman, G. Cosmo, P. Degtyarenko, A. Dell'Acqua, G. Depaola, D. Dietrich, R. Enami, A. Feliciello, C. Ferguson, H. Fesefeldt, G. Folger, F. Foppiano, A. Forti, S. Garelli, S. Giani, R. Giannitrapani, D. Gibin, J.J. Gmez Cadenas, I. Gonzlez, G. Gracia Abril, G. Greeniaus, W. Greiner, V. Grichine, A. Grossheim, S. Guatelli, P. Gumplinger, R. Hamatsu, K. Hashimoto, H. Hasui, A. Heikkinen, A. Howard, V. Ivanchenko, A. Johnson, F.W. Jones, J. Kallenbach, N. Kanaya, M. Kawabata, Y. Kawabata, M. Kawaguti, S. Kelner, P. Kent, A. Kimura, T. Kodama, R. Kokoulin, M. Kossov, H. Kurashige, E. Lamanna, T. Lampn, V. Lara, V. Lefebure, F. Lei, M. Liendl, W. Lockman, F. Longo, S. Magni, M. Maire, E. Medernach, K. Minamimoto, P. Mora de Freitas, Y. Morita, K. Murakami, M. Nagamatu, R. Nartallo, P. Nieminen, T. Nishimura, K. Ohtsubo, M. Okamura, S. O'Neale, Y. Oohata, K. Paech, J. Perl, A. Pfeiffer, M.G. Pia, F. Ranjard, A. Rybin, S. Sadilov, E. Di Salvo, G. Santin, T. Sasaki, N. Savvas, Y. Sawada, S. Scherer, S. Sei, V. Sirotenko, D. Smith, N. Starkov, H. Stoecker, J. Sulkimo, M. Takahata, S. Tanaka, E. Tcherniaev, E. Safai Tehrani, M. Tropeano, P. Truscott, H. Uno, L. Urban, P. Urban, M. Verderi, A. Walkden, W. Wander, H. Weber, J.P. Wellisch, T. Wenaus, D.C. Williams, D. Wright, T. Yamada, H. Yoshida, and D. Zschiesche. Geant4: A simulation toolkit. *Nuclear Instruments and Methods in Physics Research Section A: Accelerators, Spectrometers, Detectors and Associated Equipment*, 506(3):250 – 303, 2003. ISSN 0168-9002. doi:10.1016/S0168-9002(03)01368-8.

[88] N. Zaitseva, B. L. Rupert, I. Paweczak, A. Glenn, H. P. Martinez, L. Carman, M. Faust, N. Cherepy, and S. Payne. Plastic scintillators with efficient neutron/gamma pulse shape discrimination. *Nuclear Instruments and*

Methods in Physics Research Section A: Accelerators, Spectrometers, Detectors and Associated Equipment, 668(0):88 – 93, 2012. ISSN 0168-9002. doi:10.1016/j.nima.2011.11.071.

[89] J.K. Dickens. A Monte Carlo based computer program to determine a scintillator full energy response to neutron detection for E_n between 0.1 and 80 MeV. *ORNL-6463*, 1988.

[90] G. Dietze and H. Klein. NRESP4 and NEFF4 : Monte Carlo codes for the calculation of neutron response functions and detection efficiencies for NE213 scintillation detectors. *PTB Report PTB-ND-22*, 1982. ISSN ISSN 0572-7170.

[91] S. A. Pozzi, M. Flaska, A. Enqvist, and I. Pázsit. Monte carlo and analytical models of neutron detection with organic scintillation detectors. *Nuclear Instruments and Methods in Physics Research Section A: Accelerators, Spectrometers, Detectors and Associated Equipment*, 582(2):629 – 637, 2007. ISSN 0168-9002. doi:10.1016/j.nima.2007.08.246.

[92] M. Tajik, N. Ghal-Eh, G.R. Etaati, and H. Afarideh. Modeling NE213 scintillator response to neutrons using an MCNPX-PHOTRACK hybrid code. *Nuclear Instruments and Methods in Physics Research Section A: Accelerators, Spectrometers, Detectors and Associated Equipment*, 704(0):104 – 110, 2013. ISSN 0168-9002. doi:10.1016/j.nima.2012.12.001.

[93] N. Patronis, M. Kokkoris, D. Giantsoudi, G. Perdikakis, C.T. Papadopoulos, and R. Vlastou. Aspects of GEANT4 Monte-Carlo calculations of the BC501A neutron detector. *Nuclear Instruments and Methods in Physics Research Section A: Accelerators, Spectrometers, Detectors and Associated Equipment*, 578(1): 351 – 355, 2007. ISSN 0168-9002. doi:10.1016/j.nima.2007.05.151.

[94] K. Banerjee, T.K. Ghosh, S. Kundu, T.K. Rana, C. Bhattacharya, J.K. Meena, G. Mukherjee, P. Mali, D. Gupta, S. Mukhopadhyay, D. Pandit, S.R. Banerjee, S. Bhattacharya, T. Bandyopadhyay, and S. Chatterjee. Variation of neutron detection characteristics with dimension of BC501A neutron detector. *Nuclear Instruments and Methods in Physics Research Section A: Accelerators, Spectrometers, Detectors and Associated Equipment*, 608(3):440 – 446, 2009. ISSN 0168-9002. doi:10.1016/j.nima.2009.07.034.

[95] X. Xufei, Z. Xing, Y. Xi, F. Tieshuan, C. Jinxiang, and L. Xiangqing. Investigation of the influence of an inner gas bubble on the response of a liquid scintillation detector to γ-rays and neutrons. *Nuclear Instruments and Methods in Physics Research Section A: Accelerators, Spectrometers, Detectors and Associated Equipment*, 721(0):10 – 16, 2013. ISSN 0168-9002. doi:10.1016/j.nima.2013.03.041.

[96] S.F. Naeem, S.D. Clarke, and S.A. Pozzi. Validation of Geant4 and MCNPX-PoliMi simulations of fast neutron detection with the EJ-309 liquid scintilla-

tor. *Nuclear Instruments and Methods in Physics Research Section A: Accelerators, Spectrometers, Detectors and Associated Equipment*, 714(0):98 – 104, 2013. ISSN 0168-9002. doi:10.1016/j.nima.2013.02.017.

[97] Geant4 Collaboration. Geant4 User's Guide for Application Developers. 2012.

[98] J. T. Goorley. Initial MCNP6 Release Overview - MCNP6 Beta 3. *Los Alamos Report LA-UR-12-26631*, 2012.

[99] A. Fasso, A. Ferrari, J. Ranft, and P.R. Sala. Fluka: a multi-particle transport code. *CERN-2005-10 (2005), INFN/TC_05/11, SLAC-R-773*, 2005.

[100] T. J. Tautges, P. P. H. Wilson, J. A. Kraftcheck, B. M. Smith, and D. L. Henderson. Acceleration techniques for direct use of CAD-based geometries in Monte Carlo radiation transport. *Proc. Int. Conf. on Mathematics, Computational Methods, and Reactor Physics*, 2009.

[101] Min Cheol Han, Chan Hyeong Kim, Jong Hwi Jeong, Yeon Soo Yeom, SungHoon Kim, Paul P H Wilson, and John Apostolakis. DagSolid: a new Geant4 solid class for fast simulation in polygon-mesh geometry. *Physics in Medicine and Biology*, 58(13):4595, 2013. URL http://stacks.iop.org/0031-9155/58/i=13/a=4595.

[102] C. L. Fiore, R. Boivin, R. S. Granetz, T. Fuller, and C. Kurz. Status of the neutron diagnostic experiment for Alcator C-Mod. *Review of Scientific Instruments*, 63(10):4530–4532, 1992. doi:10.1063/1.1143711.

[103] R. Mateus, A.P. Jesus, and J.P. Ribeiro. Quantitative analysis of light elements in thick samples by PIGE. *Nuclear Instruments and Methods in Physics Research Section B: Beam Interactions with Materials and Atoms*, 219220(0):519 – 523, 2004. ISSN 0168-583X. doi:10.1016/j.nimb.2004.01.114. Proceedings of the Sixteenth International Conference on Ion Beam Analysis.

[104] R. Mateus, A.P. Jesus, and J.P. Ribeiro. A code for quantitative analysis of light elements in thick samples by PIGE. *Nuclear Instruments and Methods in Physics Research Section B: Beam Interactions with Materials and Atoms*, 229(2):302 – 308, 2005. ISSN 0168-583X. doi:10.1016/j.nimb.2004.11.019.

[105] M. Fonseca, A.P. Jesus, H. Lus, R. Mateus, J. Cruz, L. Gasques, D. Galaviz, and J.P. Ribeiro. PIGE analysis of magnesium and beryllium. *Nuclear Instruments and Methods in Physics Research Section B: Beam Interactions with Materials and Atoms*, 268(1112):1806 – 1808, 2010. ISSN 0168-583X. doi:10.1016/j.nimb.2010.02.079. 19th International Conference on Ion Beam Analysis.

[106] C. L. Fiore and R. L. Boivin. Performance of the neutron diagnostic system for Alcator C-Mod. *Review of Scientific Instruments*, 66(1):945–947, 1995. doi:10.1063/1.1146215.

160

[107] C.G. Ryan, E. Clayton, W.L. Griffin, S.H. Sie, and D.R. Cousens. SNIP, a statistics-sensitive background treatment for the quantitative analysis of PIXE spectra in geoscience applications. *Nuclear Instruments and Methods in Physics Research Section B: Beam Interactions with Materials and Atoms*, 34(3):396 – 402, 1988. ISSN 0168-583X. doi:10.1016/0168-583X(88)90063-8.

[108] M. Morháč, J. Kliman, V. Matoušek, M. Veselský, and I. Turzo. Efficient one- and two-dimensional gold deconvolution and its application to γ-ray spectra decomposition. *Nuclear Instruments and Methods in Physics Research Section A: Accelerators, Spectrometers, Detectors and Associated Equipment*, 401(23): 385 – 408, 1997. ISSN 0168-9002. doi:10.1016/S0168-9002(97)01058-9.

[109] W.R. Wampler, B. LaBombard, B. Lipschultz, G.M. McCracken, D.A. Pappas, and C.S. Pitcher. Molybdenum erosion measurements in Alcator C-Mod. *Journal of Nuclear Materials*, 266269(0):217 – 221, 1999. ISSN 0022-3115. doi:10.1016/S0022-3115(98)00663-1.

[110] B. Lipschultz, D.G. Whyte, J. Irby, B. LaBombard, and G.M. Wright. Hydrogenic retention with high-z plasma facing surfaces in alcator c-mod. *Nuclear Fusion*, 49(4):045009, 2009. URL http://stacks.iop.org/0029-5515/49/i=4/a=045009.

[111] Y. Lin, J. Irby, B. Lipschultz, E. Marmar, D. Whyte, S. Wolfe, and S. Wukitch. Hydrogen control in alcator c-mod walls and plasmas. *Journal of Nuclear Materials*, 363365(0):920 – 924, 2007. ISSN 0022-3115. doi:10.1016/j.jnucmat.2007.01.115. Plasma-Surface Interactions-17.

[112] J. Irby, D. Gwinn, W. Beck, B. LaBombard, R. Granetz, and R. Vieira. Alcator C-Mod design, engineering, and disruption research. *Fusion Science and Technology*, 51:260–275, 2007.

[113] R. Ochoukov, D. G. Whyte, B. Lipschultz, B. LaBombard, N. Gierse, and S. Harrison. Study and optimization of boronization in Alcator C-Mod using the Surface Science Station (S3). *Fusion Engineering and Design*, 87(9):1700 – 1707, 2012. ISSN 0920-3796. doi:10.1016/j.fusengdes.2012.07.013.

[114] Y. Sakamoto, Y. Ishibe, K. Yano, H. Oyama, Y. Tanaka, N. Fujisawa, Y. Matsuzaki, N. Suzuki, K. Maeno, T. Yamamoto, and K. Yokokura. Electron cyclotron resonance discharge cleaning of JFT-2 Tokamak (JAERI). *Journal of Nuclear Materials*, 9394, Part 1(0):333 – 337, 1980. ISSN 0022-3115. doi:10.1016/0022-3115(80)90344-X.

[115] H. F. Dylla. Glow discharge techniques for conditioning high vacuum systems. *Journal of Vacuum Science Technology A: Vacuum, Surfaces, and Films*, 6(3): 1276–1287, 1988. ISSN 0734-2101. doi:10.1116/1.575689.

[116] B. Lipschultz, Y. Lin, E.S. Marmar, D.G. Whyte, S. Wukitch, I.H. Hutchinson, J. Irby, B. LaBombard, M.L. Reinke, J.L. Terry, and G. Wright. Influence of

boronization on operation with high-Z plasma facing components in Alcator C-Mod. *Journal of Nuclear Materials*, 363365(0):1110 – 1118, 2007. ISSN 0022-3115. doi:10.1016/j.jnucmat.2007.01.227. Plasma-Surface Interactions-17.

[117] J. Winter, H.G. Esser, L. Knen, V. Philipps, H. Reimer, J.v. Seggern, J. Schlter, E. Vietzke, F. Waelbroeck, P. Wienhold, T. Banno, D. Ringer, and S. Vepek. Boronization in TEXTOR. *Journal of Nuclear Materials*, 162164(0):713 – 723, 1989. ISSN 0022-3115. doi:10.1016/0022-3115(89)90352-8.

[118] K. Tsuzuki, M. Natsir, N. Inoue, A. Sagara, N. Noda, O. Motojima, T. Mochizuki, T. Hino, and T. Yamashina. Hydrogen absorption behavior into boron films by glow discharges in hydrogen and helium. *Journal of Nuclear Materials*, 241243(0):1055 – 1059, 1997. ISSN 0022-3115. doi:10.1016/S0022-3115(97)80193-6.

[119] J. Huizenga, S. Seifert, F. Schreuder, H.T. van Dam, P. Dendooven, H. Lhner, R. Vinke, and D.R. Schaart. A fast preamplifier concept for SiPM-based time-of-flight PET detectors. *Nuclear Instruments and Methods in Physics Research Section A: Accelerators, Spectrometers, Detectors and Associated Equipment*, 695(0):379 – 384, 2012. ISSN 0168-9002. doi:10.1016/j.nima.2011.11.012. New Developments in Photodetection NDIP11.

[120] C. E. Sagan. *Cosmos*. Random House, Inc., 1980.